GENERATION OF SUB-WAVELENGTH FAR AND NEAR-FIELD FOCUSING PATTERNS USING OPTICAL VECTOR BEAMS

by

Ran Chen

Submitted in partial fulfilment of the requirements
for the degree of Doctor of Philosophy

at

Dalhousie University
Halifax, Nova Scotia
July 2020

Dedicated to my parents for their endless love, care and support.

TABLE OF CONTENTS

LIST OF TABLES

LIST OF FIGURES

ABSTRACT

Optical fields with complex spatial distribution are of great importance in various applications such as super-resolution imaging, laser nanofabrication, molecule or nanoparticle trapping and manipulation. This dissertation focuses mainly on both far-field and near-field focusing and shaping using optical vector fields.

The focusing characteristics of cylindrical vector beams such as doughnut Gaussian beam and Bessel-Gaussian beam in a high numerical aperture focusing system were theoretically investigated based on the Richards-Wolf diffraction integral theory. Cosine function based complex amplitude filters were introduced to the high numerical aperture system to achieve a focusing field with a long depth of focus. Results show that a focusing spot with sub-wavelength lateral size and short depth of focus can be obtained when the radially polarized doughnut Gaussian incident beam is properly designed. A cosine function based complex amplitude filter was designed to increase the depth of focus of the focusing field. Using this complex amplitude filter, hollow beams with a long focal depth were successfully generated in a high numerical aperture focusing system. A radially polarized Bessel-Gaussian beam was used as the incident beam and a second-order vortex phase filter was used to create the null intensity on the optical axis. In addition, the radially polarized Bessel-Gaussian beam and the complex amplitude filter were used in a high numerical aperture 4π focusing system. A long longitudinally polarized optical chain was generated successfully.

For the near-field case, the impact of the illumination polarization on the obtained photonic nanojets was numerically investigated for the model of a microsphere illuminated by plane waves and Gaussian beams with different polarizations. Both linearly and circularly polarized plane waves and linearly, circularly, radially, and azimuthally polarized Gaussian beams were used to generate photonic nanojets. Results show that one can precisely engineer the overall shape, intensity, location, and transverse and longitudinal size of the generated photonic nanojet at will for different applications by controlling the polarization and the amplitude profile of the illumination beam.

LIST OF ABBREVIATIONS USED

AFM	Atomic Force Microscopy
BG	Bessel-Gaussian Beam
CVB	Cylindrical Vector Beam
DG	Doughnut Gaussian Beam
DOF	Depth of Focus
DOCP	Degree of Circular Polarization
DOLP	Degree of Linear Polarization
DOP	Degree of Polarization
EFL	Effective Focal Length
FDTD	Finite-Difference Time-Domain
FOV	Field of View
FWHM	Full-Width at Half-Maximum
LC	Liquid Crystal
LCOS	Liquid Crystal on Silicon
LG	Laguerre-Gaussian Beam
LHC	Left-Handed Circularly Polarized
NA	Numerical Aperture
PALM	Photo-Activated Localization Microscopy
PML	Perfectly Matched Layer
PNJ	Photonic Nanojet
PS	Polystyrene
PSF	Point Spread Function
RHC	Right-Handed Circularly Polarized
SIM	Structured Illumination Microscopy
SLM	Spatial Light Modulator
SNR	Signal-to-Noise Ratio
SOP	State of Polarization
SSIM	Saturated Structured Illumination Microscopy
STED	Stimulated Emission Depletion Microscopy
STORM	Stochastic Optical Reconstruction Microscopy

ACKNOWLEDGEMENTS

Nobody has been more important to me in the pursuit of this journey than the members of my family. Special thanks are due to my parents. They are the ultimate role models in my life. I couldn't have come this far without their love, care and support.

CHAPTER 1   INTRODUCTION

Engineering of optical focusing field has attracted a tremendous amount of research interests in the areas of super-resolution imaging, optical trapping, and nano-/micro-particle manipulation. Laser beam shaping and focus shaping have seen great development over the past few decades. Equipment based on shaped optical fields has been developed to trap, guide, and pattern molecules, and nano/micro particles in order to better understand subjects such as biophysics. In the microscope field, spatial engineering of optical fields has been extensively studied to overcome the diffraction limit. Another hot research topic is that of vortex beams because of their unique orbital angular momentum property due to spiral phase wave front. Researchers have done a tremendous amount of work to develop technology using the vortex beam's orbital angular momentum as a free space communication information carrier because of its orthogonality and multiplexing capability. In addition to the study of intensity and phase of light for various potential applications, the polarization of light is also a key element in optical field shaping. Many applications require precise control of various parameters in the optical system to achieve the desired focusing field. This project aims to explore new techniques for engineering the focusing field in both far-field and near-field and gain a better understanding of sub-wavelength focusing through modelling.

1.1 DIFFRACTION LIMIT AND OPTICAL RESOLUTION CRITERIA

When light is emitted from a point source located far from a focusing system, a fraction of the emitted light will be captured by the optical focusing system and focused at a corresponding point in the focal region. However, the focusing lens does not focus the captured light to an infinitely small point at the focal point. Instead, a diffraction pattern is produced at the focal point. Diffraction happens because of the wave nature of light and the lens pupil is a diffracting aperture [1] - [2]. The diffraction effect was first theoretically

proposed by Huygens and was further investigated by Fresnel [1] - [2]. Using Young's single and double slits, direct experimental observation of the diffraction effect can be obtained.

In the focal region, the electromagnetic field distribution is the interference result of all diffracted light waves that emerged from the lens aperture. This diffraction pattern at the focal point is called the point spread function (PSF) of the focusing system [2] - [3]. In fact, PSF is the fundamental building block in image formation models. The PSF of an optical system is a three-dimensional diffraction pattern of light emitted from an infinitely small point source and transmitted to the focal plane through the optics. When viewed in the transverse plane, the PSF is a pattern of concentric rings of light surrounding a central bright disk. For a circular aperture, the PSF in the transverse plane is an Airy disk [3]. In the longitudinal plane, the diffraction pattern can have various shapes depending on the type of focusing system used (e.g. widefield, or confocal) but is often hourglass or American football shaped.

Generally, the dimensions of a focusing spot produced by an optical focusing system can be characterized by two parameters: longitudinal size (D_L) and transverse size (D_T). The size and shape of the focusing spot has a direct impact on the resolving power of an optical focusing system. If there are two point objects in the specimen that are close enough to each other, the corresponding PSFs will merge into each other and we can no longer distinguish the images of these two points in the image plane. For diffraction-limited optical systems, various criteria such as Abbe [4], Rayleigh [5], Sparrow [6], and Houston [7] have developed mathematical models to determine how close two point objects can be separated from each other and discerned as two individual point sources in the image plane. The ability of an imaging system to resolve detailed features in a sample that is being imaged is called optical resolution. The resolution of a lens-based optical focusing system depends on many factors. The illumination characteristics including wavelength, polarization, and coherence [8] - [9] as well as certain parameters of the focusing system such as the numerical aperture (NA) of the objective lens [10] have direct impact on the overall focusing performance.

According to Abbe's theory [4], incident light is diffracted by object features in the specimen. Features in the specimen separated by a distance d can be considered as a diffraction grating with a period of d whose Fourier transform forms images at the focal plane of the lens system. The lens system operates as a low pass filter and not all spatial frequencies can be collected by the lens system [11] - [12]. Therefore, the resolution is limited.

To satisfy the following grating equation, the mth diffraction order occurs at an angle θ_m.

$$dsin\theta_m = m\lambda \tag{1.1}$$

where θ_m is the angle between the mth diffraction order and the normal direction to the grating surface. From the grating equation, the smaller d, meaning the smaller the details of a feature in the sample, the larger θ_m for a given diffraction order. In theory, the zero-order and one of the higher order rays needs to be collected by the lens system in order to resolve that feature properly [11]. The condition for passing one of the first order diffracted rays through the lens system gives the Abbe diffraction limit:

$$d = \frac{0.5\lambda_0}{NA} \tag{1.2}$$

where λ_0 is the free space wavelength of the illumination light. NA is the numerical aperture of the lens system. This means that features smaller than $\frac{0.5\lambda_0}{NA}$ in a sample cannot be resolved by this specific imaging system.

As is shown in Figure 1, the NA of a lens is defined as:

$$NA = n \cdot sin\theta \tag{1.3}$$

where n is the refractive index of the surrounding medium, and θ is the half angle of the maximum cone of light that can enter the lens.
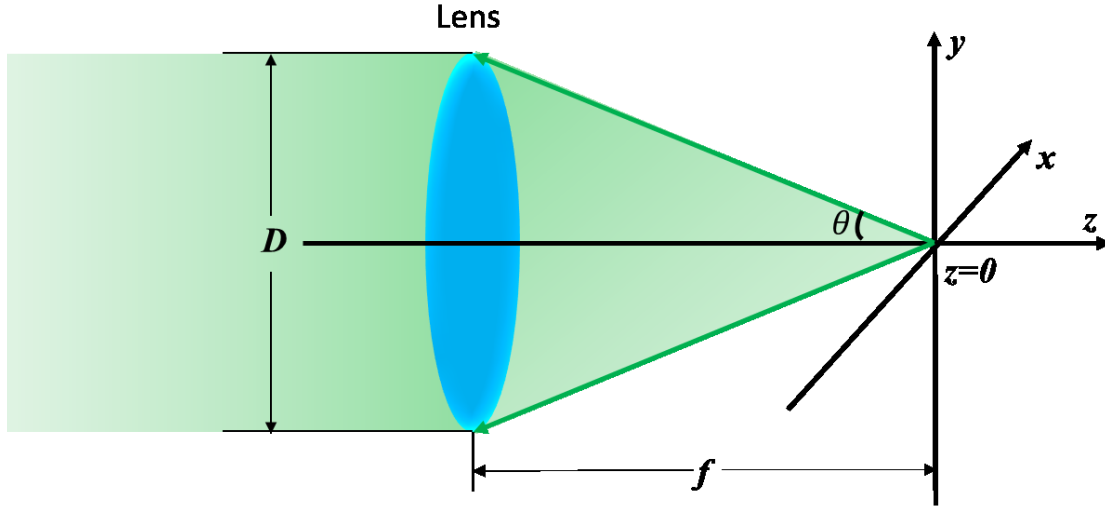
Figure 1 Numerical aperture of a lens.

From the Abbe diffraction limit equation and the definition of NA, we can see that the resolution of the imaging system can be improved by increasing the refractive index of the surrounding medium between the sample and the lens, increasing the light acceptance angle of the lens system, and reducing the illumination wavelength. Typically, the Abbe diffraction limit for a regular white light imaging system is about 200 - 250 nm. Techniques that can improve the resolution beyond the Abbe diffraction limit have been called super-resolution imaging in literatures [11].

As mentioned at the beginning of this section, there are a few other classical resolution criteria. In principle, they are related to the size of the main lobe of the PSF of the imaging system. For a circular aperture with a diameter of D, the PSF is an Airy disk [3]:

$$I(r) = I_0 \left(\frac{2J_1(k_0 r NA)}{k_0 r NA} \right)^2 \tag{1.4}$$

where $k_0 = \frac{2\pi}{\lambda_0}$ is the free space wave number of the illumination light. If there are two point sources to be imaged by a lens system, their PSFs merge into each other and can no longer be distinguished at the image plane when they are close enough. The Rayleigh resolution limit states that the images of two point sources with equal intensities are just resolvable if the center of the diffraction pattern produced by one point source coincides with the first zero of the diffraction patterns produced by the second source [3] - [5]. In this scenario, the field intensity distribution at the image plane shows a saddle shape [13].

To satisfy the Rayleigh criteria, the distance between the two point sources d should be greater or equal to the radius of the Airy disk. Because the first zero of the Bessel function of the first kind $J_1(x)$ appears at $x = 1.22\pi$, the Rayleigh diffraction limit can be written as:

$$d = \frac{0.61\lambda_0}{NA} \tag{1.5}$$

However, it is worth mentioning that Abbe's resolution limit is developed based on a physical model, while the Rayleigh resolution criteria is a heuristic estimation of the resolution limit of an optical system [4], [5], [14].

1.2 INTRODUCTION TO VARIOUS SUPER-RESOLUTION IMAGING TECHNIQUES

In this section, the background and mechanism of various super-resolution imaging techniques are introduced. The principles of super-resolution microscopy, near-field scanning optical microscopy, and microsphere based near-field super-resolution imaging method are reviewed and discussed. These techniques have all achieved improved lateral resolution down to tens of nanometers, but each method has a unique set of limitations.

1.2.1   Far-field super-resolution optical imaging

Conventional optical microscopy has many advantages for the imaging of biological and cellular samples. A typical optical microscope has a theoretical lateral resolution limit of 200 nm according to Abbe's diffraction limit theory. Several optical super-resolution microscopy systems have been developed to overcome the diffraction limit including confocal microscopy, point spread function engineering based stimulated emission depletion microscopy (STED) [15] - [21]; single molecule localization based photo-activated localization microscopy (PALM) and stochastic optical reconstruction microscopy (STORM) [22] - [30], and Moiré effect based structured illumination microscopy (SIM) [31] - [38]. This section will briefly summarize the working principles of some of these techniques.

The STED microscopy uses two focused laser beams of different wavelengths to achieve super-resolution imaging. The two beams are called the exciting laser beam and the depletion beam [15] - [16]. In this approach, the excitation beam activates the fluorophores in the sample, while the depletion beam switches off the fluorophores at predefined positions of the diffraction limited regions. Only the excited fluorophores in the complementary regions emit light, allowing features in the sample smaller than the diffraction limit to be resolved.

In a common STED microscopy setup, super-resolution imaging can be achieved by co-aligning a Gaussian excitation beam with a doughnut shaped depletion beam [17] - [18]. The excitation beam activates the fluorophores in the sample. The depletion beam is engineered in phase and/or polarization to create a doughnut shaped focal intensity distribution with a zero-intensity center. The depletion beam in the STED microscopy is diffraction limited. But the high intensity saturates the stimulated emission transition and keeps most of the fluorophores in the ground state. Only those fluorophores located in the zero-intensity center are excited. The size of the zero-intensity center can reach a sub-diffraction limited value and further decrease with the increase of the depletion beam intensity.

The spatial resolution of a STED microscopy is given by the size of the effective fluorescent region which is defined by the size of the zero-intensity center. Theoretically, the resolution of STED microscopy can reach the ultimate limit of a fluorescent microscope - molecule size. In practice, it is limited by the signal-to-noise ratio (SNR) [39] because the STED microscopy needs to scan the coaligned beams together across the whole sample to form a super-resolution image of the sample. It is important to both generate sub-diffraction fluorescent regions across the whole sample and to collect enough fluorescent photons from all regions to obtain good SNR.

The PALM/STORM methods rely on fluorophore blinking in the presence of excitation light and collecting many images, each containing just a few active isolated fluorophores [22] - [23]. This method can stochastically switch on and off a subset of photoswitchable fluorophores at the single molecule level at a time. During each on and off cycle, the density of activated molecules is kept low enough that the molecular images of individual fluorophores do not typically overlap. Each fluorophore can then be separately identified using computer algorithms. Both PALM and STORM have similar imaging procedures. The difference between these two methods is the use of different fluorophores [41]. PALM uses genetically encoded photoswitchable protein fluorophores, while STORM uses photoswitchable dye fluorophores. The fluorophores switch between fluorescent state and dark state by applying excitation light of different wavelengths. The activated fluorophores will emit low intensity light and are imaged by a digital camera. The point spread functions of each individual molecule are localized with high precision based on the photon output before the fluorophores switch to the dark state. Repeat this process many times and a series of images can be obtained. A sub-diffraction limited image can be constructed by combining all the identified positions of the fluorescent probes. A common drawback of the STORM technique is that a large amount of data needs to be collected and processed, therefore it is slow in generating a single picture [41].

Moiré patterns or Moiré fringes are interference patterns that appear when two similar patterns with fine details are superimposed. If one of the fine patterns and the Moiré interference pattern is known, the other fine pattern can be calculated. SIM takes advantage

of this idea and achieves super-resolution successfully [37]. In a typical SIM setup, a diffraction grating is utilized in the illumination beam to generate a high contrast grating pattern with feature size down to the resolution limit of the microscope objective used in the system. This structured illumination provides one of the fine patterns. The other fine pattern is the small features in the sample that need to be imaged. The interference pattern given by these two fine patterns can then be recorded by a microscope.

A typical SIM setup is usually not very complicated. The main difference between a SIM setup and a confocal microscope is that SIM needs a diffraction grating to generate a high-contrast pattern with a feature size down to the resolution limit of the microscope objective lens. In addition, the grating must be rotatable for full image capability. For a traditional microscope whose resolution is limited at around 290 nm, the SIM technique can improve the resolution power down to 115 nm [41]. Other types of SIM based techniques have been developed as well. A wide-field imaging technique called saturated structured illumination microscopy (SSIM) was reported in 2005 [40] and 50 nm lateral resolution was achieved.

During the last two decades, far-field optical super-resolution techniques have seen great development. Many ideas evolved into commercial products successfully. Most of these techniques offer both high lateral and axial resolution. However, there are other important factors, such as field of view (FOV), cost of the imaging system and so on, that need to be addressed as well.

1.2.2   Near-field super-resolution optical imaging

Most of the far-field techniques use fluorescent labelling to achieve super-resolution. There are also many techniques that can overcome the diffraction limit by taking advantage of the near-field evanescent waves. Evanescent waves are non-propagating electromagnetic waves, whose energy is spatially confined in the vicinity of the source and decays exponentially with distance from the source [3]. Common near-field techniques need to place a probe close to the sample to collect the evanescent waves. The problem

with this type of setup is the FOV is usually limited. In this section, a few near-field techniques will be reviewed and discussed.

Near-field scanning optical microscopy (NSOM) is a technique that takes advantages of both the scanning probe imaging technology and optical microscopy technology. The first report of a NSOM experimental setup concept dates back to 1928 [42]. However, the idea wasn't really implemented until 50 years later [43] - [47]. The development of micro fabrication technology enabled the fabrication of sub-wavelength optical aperture at the apex of a sharp transparent tip coated with metal.

Generally, the NSOM technique can be implemented in different ways. In the aperture based method, the sample is placed on a glass hemisphere substrate. Only a small section of the sample is illuminated [48] - [49]. The glass substrate acts as a transducer and convert the collected near-field information to far-field. Lateral resolution between 10 nm and 100 nm were reported using this technique. With the apertureless method, an external far-field illumination is strongly confined at the tip to achieve 1 nm to 20 nm lateral resolution. The problem with this method is that a useful signal must be extracted from the strong external illumination light [50] - [57]. The third common method is called scanning optical microscopy. A tip is used to collect the near-field information in close vicinity to the sample [58] - [59].

The key element that has a significant impact on the performance of these NSOM methods is the aperture of the probe tip. The transmission coefficient of the probe tip can be modeled using the Bethe-Bouwkamp [60] - [61]. The coefficient decreases dramatically for small apertures. One could increase the input power to improve the SNR. But high power may damage the metal coating on the tip. A good balance between minimizing the aperture size and the input power is critical in NSOM setup [62] - [66]. NSOM technique has good super-resolution capability but its biggest drawback is that only the surface of samples can be observed.

Metamaterials based near-field super-resolution technique has drawn tremendous research interests in the past decade. Pendry et al. [67] proposed the "perfect lens" concept based on the negative refractive index medium theory. In theory, the negative refractive index medium can compensate for the decay of the evanescent waves. Therefore, the "perfect lens" made from negative refractive index medium can obtain a "perfect" image at the image plane because the near-field evanescent waves are restored as well. Metamaterials made from metallic nano structures are also designed to achieve super-resolution by taking advantage of the surface resonance effect [68]. The issue with this type of techniques is that special materials are required for both the lens and the medium, and it is usually limited to a certain frequency.

A new high refractive index microsphere based near-field super-resolution imaging technique started to attract more and more interests since the discovery of near-field evanescent wave enhancement by photonic nanojet (PNJ) has been theoretically [69] and experimentally reported [70]. PNJ is a strong near-field focusing field obtained on the shadow side when a microobject, such as microsphere or microcylinder, is illuminated by an incident beam. Typically, microspheres are used for the study of PNJ. The lateral size of the generated PNJ is around 0.5λ or smaller depending on the design parameters of the microobjects and the surrounding medium. According to various researchers' work on the mechanism of how the PNJ is generated [41], the main contribution factors to the quality of the generated PNJ are: (1) the refractive index of the microsphere (n_{sphere}) and the surrounding medium (n_{medium}); (2) the diameter of the microsphere; (3) the wavelength of the incident light.

PNJ was first reported in 2004 when the group was studying the scattering of plane waves by lossless dielectric microcylinders and microspheres [71] - [72]. Their finite-difference time-domain (FDTD) numerical calculation results show that a special type of highly localized tight focusing field can be generated at the shadow side when a microsphere is properly illuminated. They also discovered that the backscattering light generated by a sample, such as a nanoparticle, is significantly increased if it is placed in the PNJ. This discovery opens the development of microsphere based super-resolution imaging.

In 2005, the mechanism of PNJ generation was carefully modelled by a combination of geometrical optics, Mie theory, and angular spectrum theory [73]. The calculation results concluded that the generation of PNJ is because of a combination of various factors: (1) a peak in the angular spectrum; (2) the finite content of the propagating spatial frequencies; (3) a small but also finite content of the evanescent spatial frequencies; and (4) the phase. A 3D spectral analysis of the PNJ [74] was conducted later. Results show that the presence of the evanescent components close to the microsphere surface is crucial in the PNJ generation process. The presence of the evanescent components depends on the refractive index mismatch at the border of the microsphere and the surrounding medium. Therefore, changing the geometry or the material properties will significantly affect the quality of the generated PNJ.

The first experimental confirmation of the existence of PNJ was reported in 2008 [70]. Latex microspheres with different diameters were deposited on a cover glass as the sample. A laser scanning microscope was used to image the generated PNJ. The post processed picture served as direct proof of the existence of PNJs. Since then, the field of PNJ has gained tremendous research interests. Researchers studied the modification of the shape and size of PNJ [75]. Besides the regular shaped microspheres and microcylinders, researchers have started looking into PNJs generated by microparticles of other shapes. Micro-cuboids [76] - [77], micro-disks [78] - [79], core-shell microspheres [80] - [81], micro-axicons [82] - [84], micro-spheroids [85] - [87], truncated microspheres [88], liquid crystals filled micro shells with controlled tuning of the refractive index [89] have all been explored to understand the characteristics of the generated PNJs and their potential applications. Extensive experimental studies were also conducted to investigate the influence of illumination light on the obtained PNJs [90].

In the meantime, application of PNJ in super-resolution imaging [91] and single molecule detection [92] starts to emerge. In 2011, Z. Wang et al. [91] demonstrated the first microsphere based super-resolution imaging system. In their publication, silicon dioxide microspheres were used to generated PNJs. A conventional white light microscope was used to capture the virtual image of the nano patterns formed by the microspheres. Several

sub-diffraction limited pattern samples were used in this experiment and 100 nm features were successfully resolved. The ability to use PNJs generated by microspheres for super-resolution was successfully demonstrated. However, the author also pointed out that the performance of the PNJ based super-resolution imaging may depend on the sample.

More and more applications of PNJs in various fields have been demonstrated in recent years. Large microspheres were explored for super-resolution imaging to increase the FOV [93]. PNJ based super-resolution imaging technique was used for biological samples [94] - [97] and metrology [98]. One fundamental issue with the PNJ based super-resolution imaging approaches is the FOV is limited because of the size of the microsphere used in this scheme. Various methods have been proposed and demonstrated to solve this problem. Micromanipulators were designed for the PNJ based super-resolution imaging system to form a scanning system [99] - [101]. Autonomous microbots were introduced to perform the scanning process [102]. Atomic force microscopy (AFM) systems were modified to integrate the microspheres to build a scanning PNJ based super-resolution imaging [103] - [104]. Thin film embedded microsphere based super-resolution imaging method was reported in [105] - [106]. Many of the reported PNJ based super-resolution imaging approaches were aimed at demonstrating lower and lower resolutions. Their resolution measurement method was arbitrary, which makes it very difficult to compare the results. Therefore, a standard measurement process was proposed [107] - [108].

The microsphere based super-resolution imaging system has great advantages over other super-resolution imaging techniques in terms of cost-effectiveness. The potential applications of microsphere based super-resolution imaging system extends to many research fields where optical observation of sub-diffraction limited samples is required. However, the FOV of these systems remains an issue that limits their further development in various application scenarios. It is important to have more innovative concepts proposed and demonstrated to further develop this technology.

1.3 OVERVIEW OF THE DISSERTATION

In the far-field, unique cylindrical vector beams are employed, and complex amplitude filters are designed to engineer the focusing field in a high NA focusing system. In the near-field, sub-wavelength PNJs generated through the interaction between a high refractive index dielectric microsphere and cylindrical vector beams are carefully studied. The objectives of this project are:

(1) To investigate the focusing performance of various cylindrical vector beams (CVBs) in a high NA focusing system.

(2) To demonstrate the feasibility of engineering the focusing field in the far-field using CVBs and complex amplitude filters. The implementation of the designed complex amplitude filters is also expected to be explored.

(3) To study and understand the mechanism and characteristics of microsphere interaction with optical vector fields. This project intends to carefully investigate the near-field PNJ shaping using various polarized illumination beams.

These objectives are all met with the results published as journal papers or presented in international conferences. My contributions are summarized as follows:

(1) Performed analytical calculation of the focusing performance of different cylindrical vector beams in a high NA focusing system. Specifically, unique focusing fields such as sub-wavelength focusing field, long depth of focus (DOF) optical tube and optical chain are successfully demonstrated utilizing cosine function based amplitude filters and CVB in a high NA focusing system.

(2) Developed the theory of implementing complex amplitude filters using binary optics. Analytical calculation results show that the proposed binary optics filter can achieve almost the same focusing field shaping performance as the complex amplitude filter. More importantly, binary optics filter doesn't have the power attenuation problem and it is much easier to fabricate than the complex amplitude filter with a continuous varying profile.

(3) Demonstrated near-field PNJ shaping using optical vector beams. Numerical results show that one can precisely engineer the overall shape, intensity, location, and transverse and longitudinal size of the generated PNJ by controlling the polarization and the amplitude profile of the illumination beam. Knowledge developed from this work can be used for applications such as PNJ based sensor design in the future.

The dissertation is organized as follows. Chapter 1 is dedicated to the review of various far-field and near-field super-resolution imaging techniques and their underlying principles.

Chapter 2 provides a detailed description of the characteristics of CVBs. Specifically, the mathematical model of the focusing properties of CVBs in a high NA focusing system is introduced.

In Chapter 3, different cylindrical vector beams and complex amplitude filters are designed to precisely engineer the focusing field of a high NA focusing system. The designed complex amplitude filters effectively increase the DOF of the focusing field. The results demonstrate that unique focusing field such as long DOF optical chain, optical tube can be easily achieved utilizing proper cylindrical vector beams and complex amplitude filters in a high NA focusing system.

In Chapter 4, near-field interaction between optical vector fields and high refractive index dielectric microspheres is carefully examined. Calculation results show that the generated PNJs can be shaped in the near-field using different optical vector fields.

Finally, conclusions are drawn, and future works are proposed at the end of the dissertation.

CHAPTER 2   CYLINDRICAL VECTOR BEAM AND ITS FOCUSING PROPERTIES

In this chapter, an overview of the polarization of light is provided. The rapid increase of research interest in cylindrical vector beams (CVBs) is largely driven by the unique focusing properties of these beams in a high NA focusing system. Analytical calculation method based on Richards-Wolf theory is presented to characterize the focusing performace of CVBs in a high NA focusing system.

2.1 POLARIZATION OF LIGHT

Polarization is an important property of light. The vector nature of light and its interactions with matter make many optical devices and optical system designs possible. Polarization propagation and interaction with materials have been extensively explored in optical inspection and metrology, display technologies, data storage, optical communications, materials sciences, and astronomy, as well as in biological studies.

Electromagnetic wave polarization is associated with the time evolution of the field vectors. The polarization state of a field describes the oscillation trajectory of the field vectors. There are several methods that have been developed for analyzing wave polarization, such as Jones matrix, Mueller matrix, and other matrices [109-112].

Let us consider a plane wave propagating along the z-axis in free space. The electric field in the phasor form reads:

$$E(z,t) = Re\{(|E_x|e^{j\phi_{0x}} + |E_y|e^{j\phi_{0y}})e^{j(kz-\omega t)}\} \tag{2.1}$$

where E_x and E_y are the x and y components of the electric field. ϕ_{0x} and ϕ_{0y} are the phases of the x and y components of the electric field. k is the wavenumber and ω is the frequency of the electric field. When $|E_x| \neq |E_y|$ and $\phi_{0x} \neq \phi_{0y}$, the tip of the electric

field vector moves around an ellipse as the time evolves. This polarization state is called elliptic polarization. Although, the electric field is elliptically polarized in general, there are two important special cases. First, the electric field is said to be linearly polarized if the phases of two orthogonal components of the field are the same, $\phi_{0x} = \phi_{0y}$ in Equation (2.1). In this case, the electric field is always directed along a line making the angle $\theta = tan^{-1}\left(\frac{|E_y|}{|E_x|}\right)$ with respect to the x-axis. Second, if the phases of the two orthogonal components differ by $\frac{\pi}{2}$, and $|E_x| = |E_y|$ in Equation (2.1), the wave is said to be circularly polarized. In this case, the electric field always has the same magnitude but is moving along a circle. If the electric field moves counterclockwise around the circle, then the wave is left-handed circularly (LHC) polarized. Otherwise it's right-handed circularly (RHC) polarized.

In the Mueller calculus, the Stokes vector **S** is used to describe the polarization state of a wave. The Mueller matrix **M** is used to describe the polarization altering characteristics of a sample. The Stokes vector is defined relative to the following six measurable quantities (intensities) measured with ideal polarizers in front of a detector: I_H- horizontal linear polarizer, I_V- vertical linear polarizer, I_{45} - 45° linear polarizer, I_{135} - 135° linear polarizer, I_R - right circular polarizer, I_L - left circular polarizer. The Stokes vector is defined as:

$$\mathbf{S} = \begin{bmatrix} s_0 \\ s_1 \\ s_2 \\ s_3 \end{bmatrix} = \begin{bmatrix} I_H + I_V \\ I_H - I_V \\ I_{45} - I_{135} \\ I_R - I_L \end{bmatrix} = \begin{bmatrix} E_x^2 + E_y^2 \\ E_x^2 - E_y^2 \\ 2E_x E_y cos\delta \\ 2E_x E_y sin\delta \end{bmatrix} \tag{2.2}$$

where s_0, s_1, s_2, and s_3 are the Stokes vector parameters. The Stokes vector is a function of wavelength, position on the object, and the light's direction of emission or scatter. Therefore, a Stokes vector measurement is an average over area, solid angle, and wavelength [112]. From the Stokes vector, the following polarization parameters can be defined:

(1) Degree of polarization: $DOP = \dfrac{\sqrt{s_1^2+s_2^2+s_3^2}}{s_0}$

(2) Degree of linear polarization: $DOLP = \dfrac{\sqrt{s_1^2+s_2^2}}{s_0}$

(3) Degree of circular polarization: $DOCP = \dfrac{s_3}{s_0}$

The Stokes vector for a partially polarized light wave $(DOP < 1)$ is treated as a superposition of a completely polarized Stokes vector $\mathbf{S}_P$ and an unpolarized Stokes vector $\mathbf{S}_U$:

$$\mathbf{S} = \mathbf{S}_P + \mathbf{S}_U = \begin{bmatrix} s_0 \\ s_1 \\ s_2 \\ s_3 \end{bmatrix} = s_0 DOP \begin{bmatrix} 1 \\ \frac{s_1}{s_0 DOP} \\ \frac{s_2}{s_0 DOP} \\ \frac{s_3}{s_0 DOP} \end{bmatrix} + (1-DOP)s_0 \begin{bmatrix} 1 \\ 0 \\ 0 \\ 0 \end{bmatrix} \tag{2.3}$$

The polarized portion represents a net polarization ellipse traced by the field vector as a function of time. The ellipse has a magnitude of the semimajor axis a, semiminor axis b, and the orientation of the major axis ψ. Orientation of major axis $\psi = \frac{1}{2}\arctan\left(\frac{s_2}{s_1}\right)$ is defined as the angle between the major axis of the ellipse and the x-axis. The ellipticity parameter e is defined as the ratio of the ellipse's minor to major axis: $e = \dfrac{b}{a} = \dfrac{s_3}{s_0+\sqrt{s_1^2+s_2^2}}$.

The ellipticity angle is $\chi = \arctan\dfrac{b}{a}$. Figure 2 shows an example of a polarization ellipse.
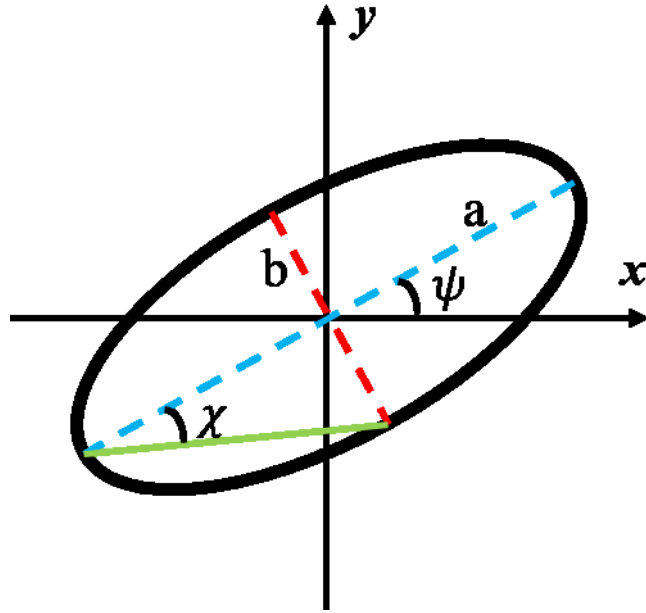
Figure 2 Polarization ellipse.

The total beam power is not usually of interest; the Stokes parameters can be normalized by dividing the Stokes parameters by the total intensity I. When the non-polarized component is also not of interest, the Stokes parameters can be further normalized to obtain:

$$
\mathbf{S} = \begin{bmatrix} s_0 \\ s_1 \\ s_2 \\ s_3 \end{bmatrix} = \begin{bmatrix} 1 \\ \cos(2\psi)\cos(2\chi) \\ \sin(2\psi)\cos(2\chi) \\ \sin(2\chi) \end{bmatrix} \tag{2.4}
$$

where I is the total intensity of the beam, DOP is degree of polarization, $2\psi = arctan\left(\frac{s_2}{s_1}\right)$, and $2\chi = arctan\left(\frac{s_3}{\sqrt{s_1^2+s_2^2}}\right)$. The factor of 2 before ψ represents the fact that any polarization ellipse is indistinguishable from one rotated by 180 degrees, while the factor of 2 before χ indicates that an ellipse is indistinguishable from one with the semi-axis lengths swapped accompanied by a 90-degree rotation. Note that $s_1^2 + s_2^2 + s_3^2 = 1$

after normalization. The three Stokes parameters s_1, s_2, and s_3 can be plotted as a sphere with unity radius for pure polarization states. In other words, the three-dimensional sphere described by Stokes parameters s_1, s_2, and s_3 includes all possible polarization states on its surface. And this sphere is called Poincaré sphere as shown in Figure 3. Partially polarized light, which can be considered a superposition of polarized and unpolarized light, is represented by a point within the volume of the Poincaré sphere.
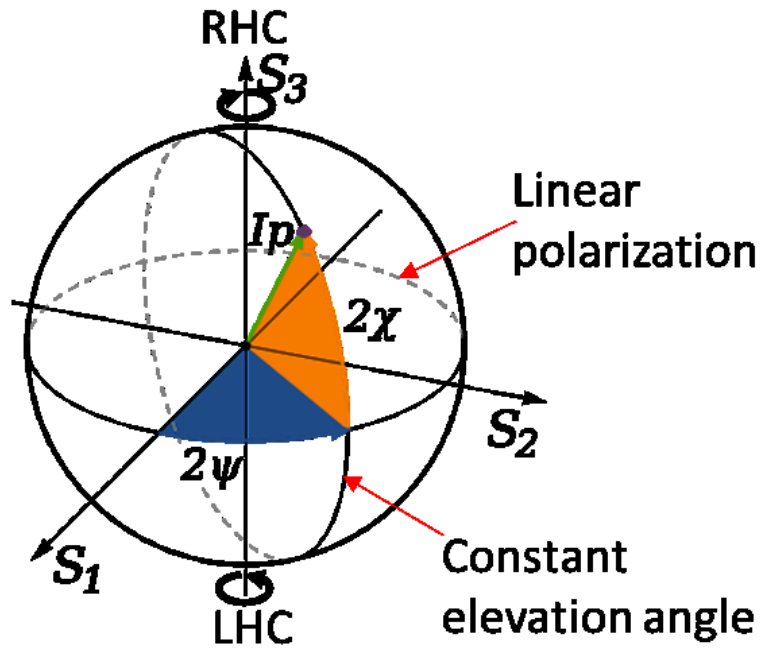
Figure 3 Poincaré sphere.

2.2 INTRODUCTION TO CYLINDRICAL VECTOR BEAMS

Most of the past research on super-resolution focusing and shaping dealt only with spatially homogeneous states of polarization, such as linear, elliptical, and circular polarizations. For these cases, the state of polarization (SOP) does not depend on the spatial location in the beam cross section. Recently there has been an increasing interest in light beams with spatially variant SOPs. Spatially arranging the SOP of a light beam, purposefully and

carefully, is expected to lead to new effects and phenomena that can expand the functionality and enhance the capability of optical systems. Laser beams with cylindrical symmetry in polarization, the so-called CVBs, are vector beam solutions of Maxwell's equations that obey axial symmetry in both amplitude and phase [113].

Radial and azimuthal polarization are two of the most common polarization states (Figure 4(b) and (c)) where the SOP follows radial and azimuthal directions at any point on the beam, respectively. Due to the orthogonality, radial and azimuthal polarizations form the basis for CVBs. Modes with radial and azimuthal polarization are well known in waveguide theory. However, their counterparts in free space are less familiar.
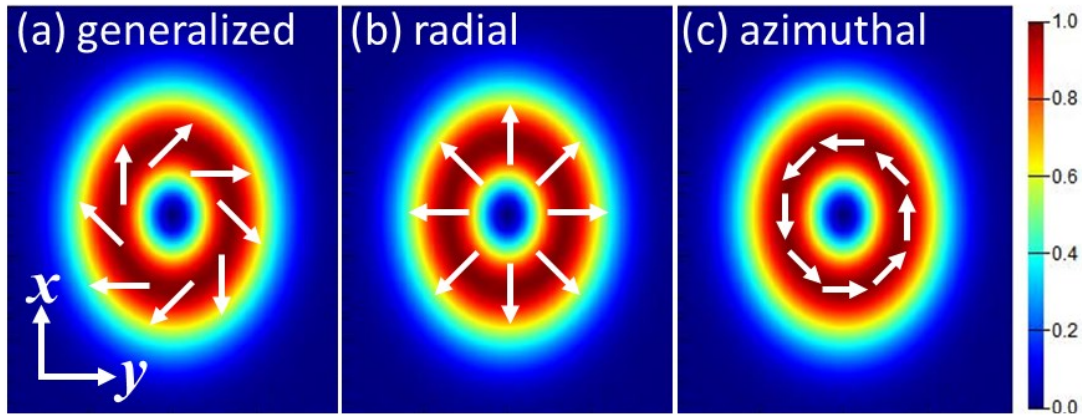
Figure 4 Cylindrical vector beams. **(a)** Generalized CV beam, **(b)** Radially polarized beam, **(c)** Azimuthally polarized beam.

The unique properties of CVBs have recently attracted a lot of research interest. One interesting application is using radially polarized beam for surface plasmon excitation and focusing. Surface plasmon generation has a strong excitation polarization dependence. In principle, a *p* polarized beam is required to excite surface plasmons in a typical total reflection configuration. *p* and *s* polarizations are two orthogonal linear polarization states that are most important for reflection and transmission. *p* polarized (from the German *parallel*) light has an electric field polarized parallel to the plane of incidence, while *s* polarized (from the German *senkrecht*) light is perpendicular to this plane. Researchers

found out that the optimal plasmonic focusing can be obtained with radial excitation polarization for a rotationally symmetric setup [113]. In this case, the entire beam is *p* polarized with respect to the dielectric/metal interface when a radially polarized beam is used, providing an efficient way to generate a highly focused surface plasmon wave. The rapid increase of interest in CVBs was driven largely by the unique focusing properties of these recently discovered beams. The focal spot of a radially polarized beam can be much smaller than the diffraction limited spot size of spatially homogeneously polarized beams in a high NA focusing system mainly because of the creation of a strong and localized longitudinal component [113]. Super-resolution imaging can be realized using CVBs in a high NA focusing system. When tightly focused, a radially polarized beam also exhibits a strong axial component with a smaller spot size centered on the optic axis. The strong axial component provides a large gradient force mainly due to the non-propagating property. The axial scattering and absorption forces will be reduced, which leads to the successful trapping of gold nanoparticles with a higher transverse trapping stiffness and trapping of micrometer-sized dielectric particles with a higher axial and transverse trapping efficiency for radially and azimuthally polarized beams, respectively [113]. In a 4Pi microscopy, both dark and bright spherical focal spot can be created using a radially polarized beam with spatially engineered amplitude and phase distribution.

The focusing of electromagnetic field over a three-dimensional volume has always been an interesting and important research area in both theory and application aspects. The focusing properties of a linearly polarized (scalar) field have been well established by Richards and Wolf [8], [114]. However, for light beams with spatially variant SOPs, the focusing properties have not been thoroughly investigated until recently.

2.3 FOCUSING PROPERTIES OF CVBs IN A HIGH NA FOCUSING SYSTEM

The focusing property of cylindrical vector beams in a high NA focusing system can be numerically studied using the Richards-Wolf vectorial diffraction theory [113] - [116]. The geometry of the physical model is shown in Figure 5. The illumination light is a generalized

CV beam, which assumes a planar wave front over the pupil. The incident field in the pupil plane can be written in cylindrical coordinates (ρ, φ, z) as:

$$\overrightarrow{E_i}(\rho, \varphi) = l_0 P(\rho)\left[cos\varphi_0\overrightarrow{e_\rho} + sin\varphi_0\overrightarrow{e_\varphi}\right] \qquad (2.5)$$

where l_0 is the peak amplitude at the pupil plane and $P(\rho)$ is the axially symmetric pupil plane amplitude distribution normalized to l_0. $\overrightarrow{e_\rho}$ and $\overrightarrow{e_\varphi}$ are unit vectors in the cylindrical coordinate system.
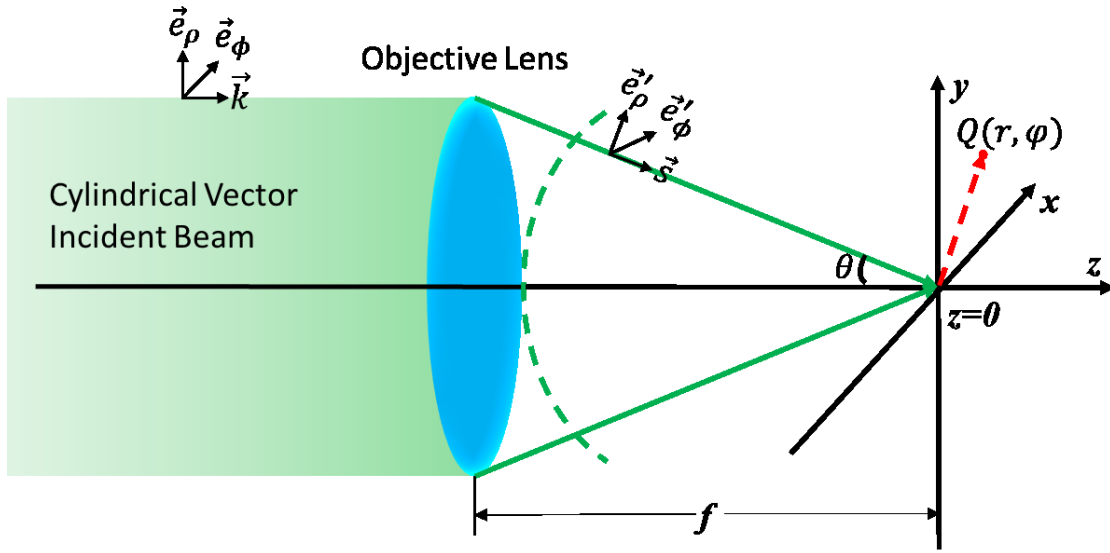
Figure 5 Focusing of a CV beam in a high NA focusing system. f is the focal length of the objective lens. $Q(r, \varphi)$ is an observation point in the focal plane.

A high NA focusing lens produces a spherical wave converging to the focal point. The amplitude distribution over the pupil is mapped onto the spherical wave front through the ray projection function $g(\theta)$ given by:

$$\frac{\rho}{f} = g(\theta) \qquad (2.6)$$

where f is the focal length of the high NA focusing lens. To satisfy the power conseravation requirement:

22

$$[l_0 P(\rho)]^2 2\pi\rho d\rho = [l_0 P(\theta)]^2 2\pi f^2 sin\theta d\theta \qquad (2.7)$$

Therefore, the pupil apodization function $P(\theta)$ on the spherical wavefront can be found with the help of the ray projection function $g(\theta)$:

$$P(\theta) = P(\rho)\sqrt{\frac{g(\theta)g'(\theta)}{sin\theta}} = P(fg(\theta))\sqrt{\frac{g(\theta)g'(\theta)}{sin\theta}} \qquad (2.8)$$

For a typical focusing lens that obey the sine condition, the ray projection function can be written as:

$$\frac{\rho}{f} = g(\theta) = sin\theta \qquad (2.9)$$

Therefore, the pupil plane apodization function can be written as:

$$P(\theta) = P(fsin\theta)\sqrt{cos\theta} \qquad (2.10)$$

The refraction of the focusing lens also changes the polarization unit vectors. The polarization unit vectors after refraction can be developed from Figure 5:

$$\vec{e_r}' = cos\theta(cos\varphi\vec{e_x} + sin\varphi\vec{e_y}) + sin\theta\vec{e_z} \qquad (2.11)$$

$$\vec{e_\varphi}' = \vec{e_\varphi} = -sin\varphi\vec{e_x} + cos\varphi\vec{e_y}] \qquad (2.12)$$

According to the Richards-Wolf theory [8], [114], the EM field near the focal point is given by the diffraction integral over the vector field on the spherical wave front with radius equal to the objective lens focal length f:

$$\vec{E_t}(r,\emptyset,z) = \frac{-ik}{2\pi} \iint_\Omega \vec{a}(\theta,\varphi)\, e^{ik(\vec{s}\cdot\vec{r})}d\Omega$$

$$= \frac{-ik}{2\pi} \int_0^{\theta_{max}} d\theta \int_0^{2\pi} \vec{a}(\theta,\varphi)e^{ik(\vec{s}\cdot\vec{r})} sin\theta d\varphi \qquad (2.13)$$

Where θ_{max} is the maximal angle determined by the NA of the objective lens, k is the wavenumber, and the field strength factor $\vec{a}(\theta,\varphi)$ is given by:

$$\vec{a}(\theta,\varphi) = l_0 f P(\theta)[cos\varphi_0\vec{e_r}' + sin\varphi_0\vec{e_\varphi}'] \qquad (2.14)$$

At any observation point in the vicinity of the focal point, we have:

$$\vec{s}\cdot\vec{r} = zcos\theta + rsin\theta\,cos(\varphi - \emptyset) \qquad (2.15)$$

Therefore, the field near the focal plane can be developed:

$$\vec{E_t}(r,\emptyset,z) = \frac{-ik}{2\pi} \int_0^{\theta_{max}} d\theta \int_0^{2\pi} l_0 f P(\theta)[cos\varphi_0\vec{e_r}'$$

$$+ sin\varphi_0\vec{e_\varphi}']e^{ik(zcos\theta+rsin\theta\,cos(\varphi-\emptyset))}sin\theta d\varphi$$

$$= -iA \int_0^{\theta_{max}} d\theta \int_0^{2\pi} P(\theta)[cos\varphi_0 \begin{pmatrix} cos\theta cos\varphi\vec{e_x} \\ cos\theta sin\varphi\vec{e_y} \\ sin\theta\vec{e_z} \end{pmatrix} +$$

$$sin\varphi_0 \begin{pmatrix} -sin\varphi\vec{e_x} \\ cos\varphi\vec{e_y} \\ 0\vec{e_z} \end{pmatrix}]e^{ik(zcos\theta+rsin\theta\,cos(\varphi-\emptyset))}sin\theta d\varphi \qquad (2.16)$$

This expression is still in Cartesian coordinates. The field components at the focal point expressed in the cylindrical coordinates can be derived using the following transformation relations:

$$\vec{e_r} = cos\emptyset\vec{e_x} + sin\emptyset\vec{e_y} \qquad (2.17)$$

$$\vec{e_{\emptyset}} = -sin\emptyset\vec{e_x} + cos\emptyset\vec{e_y} \qquad (2.18)$$

Then we can obtain the field distribution in the cylindrical coordinates:

$$\vec{E_t}(r,\emptyset,z) = -iA \int_0^{\theta max} d\theta \int_0^{2\pi} P(\theta)[cos\varphi_0 \begin{pmatrix} cos\theta cos(\varphi-\emptyset)\vec{e_r} \\ 0\vec{e_\emptyset} \\ sin\theta\vec{e_z} \end{pmatrix} +$$

$$sin\varphi_0 \begin{pmatrix} 0\vec{e_r} \\ cos(\varphi-\emptyset)\,\vec{e_\emptyset} \\ 0\vec{e_z} \end{pmatrix}]e^{ik(zcos\theta+rsin\theta\,cos(\varphi-\emptyset))}sin\theta d\varphi \qquad (2.19)$$

This expression can be further simplified with the following expression:

$$\int_0^{2\pi} cos(n\varphi)\,e^{ikrsin\theta cos\varphi}d\varphi = 2\pi\, i^n J_n(krsin\theta) \qquad (2.20)$$

where $J_n(x)$ is the Bessel function of the first kind with order n. The amplitude of the radial, longitudinal, and azimuthal components can be written as:

$$E_r(r,\emptyset,z) = A \int_0^{\theta max} P(\theta)\,sin(2\theta)\,J_1(krsin\theta)e^{ikzcos\theta}d\theta \qquad (2.21A)$$

$$E_z(r,\emptyset,z) = i2A \int_0^{\theta max} P(\theta)sin^2\theta J_0(krsin\theta)e^{ikzcos\theta}d\theta \qquad (2.21B)$$

$$E_\emptyset(r,\emptyset,z) = 2A \int_0^{\theta max} P(\theta)\,sin\,\theta J_1(krsin\theta)\,e^{ikzcos\theta}d\theta \qquad (2.21C)$$

The total field distribution in the focal region is:

$$\vec{E_t}(r,\emptyset,z) = E_r\vec{e_r} + E_z\vec{e_z} + E_\emptyset\vec{e_\emptyset} \qquad (2.22)$$

From Equation (2.14) and Equation (2.16), we can see that the radial component of the incident beam contributes to the radial and longitudinal field components near the focal

point, while the azimuthal component in the incident beam contributes only to the azimuthal field component near the focal point. Therefore, radially polarized CVBs can be used in a high NA focusing system in order to achieve long DOF sub-wavelength focusing field.

CHAPTER 3   ENGINEERING OF THE FOCUSING FIELD OF A HIGH NA FOCUSING SYSTEM USING CYLINDRICAL VECTOR BEAMS

Several far-field focusing field engineering schemes are proposed and demonstrated in this chapter. Different CVBs and complex amplitude filters are applied to a high NA focusing system to achieve unique focusing field, such as optical tube and optical chain, with sub-wavelength dimensions or long DOF.

3.1 Cylindrical Vector Beam Engineering For Sub-wavelength Focusing In A High NA Focusing System

With the development of the field of micro/nano-photonics, the requirement for optical elements with a sub-wavelength feature size is urgent [117]. Especially, optical lithography and optical imaging systems generally require small lateral and/or longitudinal dimensions [118] - [119]. As we know, diffraction occurs when propagation of the light wave is perturbed. Based on Abbe's principle, the focal spot size of the plane wave with wavelength λ is limited by $0.51\lambda/NA$ for an aplanatic imaging lens with a high NA. Therefore, considering the difficulties of increasing NA of the focusing system or decreasing the incident wavelength, obtaining super-resolution focusing field is a big challenge in practical applications such as optical fabrication, and imaging [120] - [121].

In order to achieve optical focusing with high lateral resolution, both theoretical and experimental studies about optical super-resolution have been extensively discussed [121] - [126]. For the far-field apodization technique, a variety of filters were proposed to achieve super-resolution focusing for incident beams with different polarizations [118], [122], [127] - [128]. For example, a longitudinally polarized optical needle was achieved by using binary optics for a radially polarized beam in 2008 [122]. More recently, complex amplitude filters have been proposed for focusing radially polarized beams [129] - [131]. Essentially, the amplitude of the incident beam will be modulated by the complex amplitude filter. Therefore, the amplitude profile of the incident beam is important in

designing a filter. For example, Wang's binary optical elements are designed based on a radially polarized Bessel-Gaussian (BG) incident beam [122]. Apparently, the difficulty in fabricating the designed filters is determined by the profile of the incident beams. Recently, many other kinds of beams, such as the Laguerre-Gaussian (LG) beam, high order LG beam, high order BG beam and sinh-Gaussian beam, are discussed in detail [122], [132] - [133]. Generally, results have indicated that the form of the designed filters and their corresponding focusing performance are strongly influenced by the incident beam.

3.1.1 Doughnut Gaussian beam

A new kind of radially polarized beam called doughnut Gaussian (DG) beam is introduced in a high NA focusing system. The DG beam is like a hollow Gaussian beam. In 2010, a sub-wavelength focal spot was achieved by using a radially polarized narrow width annular beam [134]. The DG beam, which is similar to the narrow-width annular beam, is falling to the category of Gaussian beams [135]. Considering that the intensity is null at the center of the doughnut beam, the focusing field of a radially polarized DG incident beam through a high NA lens will exhibit high resolution. In this section, we demonstrate the focusing performance of a high NA focusing system for the radially polarized DG beam. Numerical results indicate that sub-wavelength focusing can be obtained immediately.

For a high NA lens, the electric field of the DG beam at the output pupil is defined by Equation (3.1):

$$E_{\theta_0}^{\omega_0} = \exp\left[-\left(\frac{\sin(\theta)-\theta_0}{\omega_0}\right)^2\right] \tag{3.1}$$

Where ω_0 reflects the beam size at the beam waist of the Gaussian beam. ω_0 is no larger than $\arcsin\left(\frac{NA}{n}\right)$ rad. θ_0 refers to the radius of the DG beam. θ_0 is no larger than $\arcsin\left(\frac{NA}{n}\right)$ rad, and the maximum intensity of the DG incident beam is exactly located at the output pupil's margin for $\theta_0 = \arcsin\left(\frac{NA}{n}\right)$. θ is the variable of the function. Obviously,

the shape of the defined doughnut Gaussian beam is determined by θ_0 and ω_0. To be more specific, the position of the maximum field intensity depends on θ_0. For $\theta_0 = 0$, the beam governed by Equation (3.1) is a conventional Gaussian beam. The width of the DG beam is determined by ω_0. Therefore, $E_{\theta_0}^{\omega_0}$ behaves like $\delta[\sin(\theta) - \theta_0]$ when ω_0 approaches 0. In order to describe the relation between the amplitude profile of the DG beam and those two parameters of the DG beam, the amplitude distribution of the DG beam at the output pupil of the lens with NA = 0.95 is shown in Figure 6(a), (b), (c) and (d) for $\omega_0 = 0.25$ and $\theta_0 = 0.1, 0.2, 0.4$, and 0.8, respectively. Apparently, the radius of the DG beam increases when increasing θ_0.

For a radially polarized DG beam, the intensity distribution near the focus spot $z = 0$ of a high NA objective lens can be numerically analyzed by using the Richards-Wolf theory [113] - [116]. For a radially polarized DG beam governed by Equation (3.1), the focusing field can be expressed as [8], [122], [136]:

$$E_r(r,z) = A \int_0^\alpha \sqrt{cos\theta} \, \sin(2\theta) \, E_{\theta_0}^{\omega_0}(\theta) J_1(krsin\theta) \exp(ikzcos\theta) \, d\theta \qquad (3.2A)$$

$$E_z(r,z) = 2iA \int_0^\alpha \sqrt{cos\theta} sin^2\theta E_{\theta_0}^{\omega_0}(\theta) J_0(krsin\theta) \exp(ikzcos\theta) \, d\theta \qquad (3.2B)$$

where $P(\theta) = \sqrt{cos\theta}$ is the pupil apodization function. $\alpha = \arcsin\left(\frac{NA}{n}\right)$, n is the refractive index of the medium between the lens and sample. It is assumed as air in this calculation. $k = \frac{2\pi}{\lambda}$ is the wavenumber. $E_r(r,z)$ and $E_z(r,z)$ are the radially and longitudinally polarized components near the focus $z = 0$, respectively. The radial and longitudinal components are orthogonal to each other. Therefore, the total field intensity is $|E_t(r,z)|^2 = |E_r(r,z)|^2 + |E_z(r,z)|^2$.
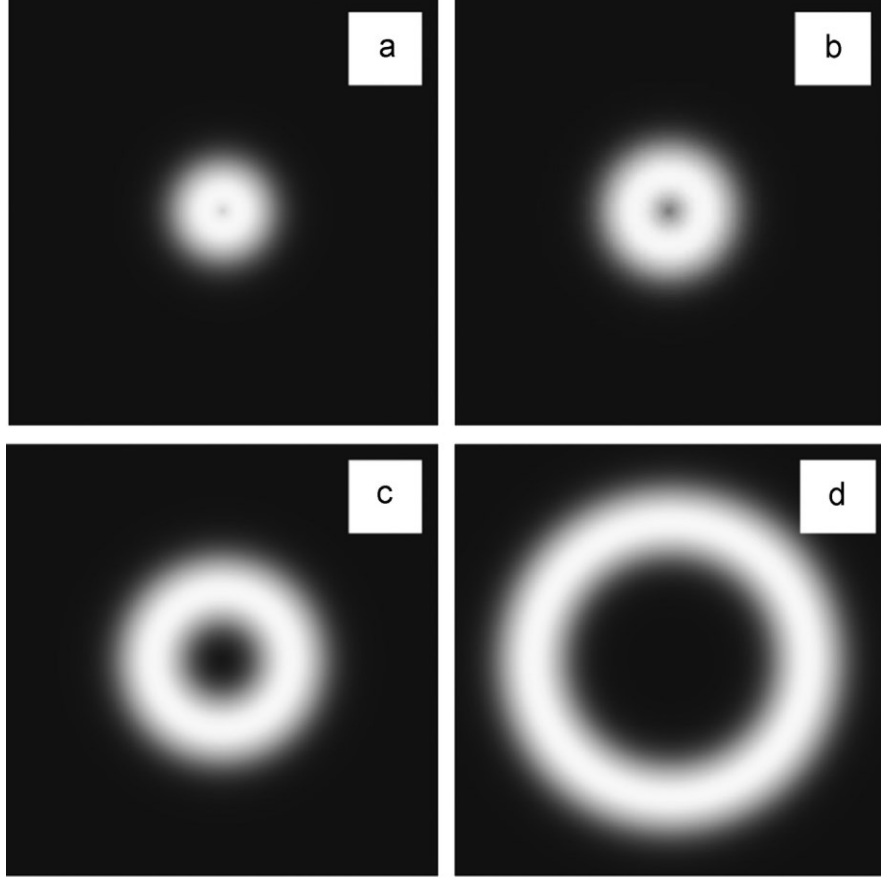
Figure 6 Amplitude distribution of the DG beam for different ω_0 and θ_0. ω_0 is 0.25.(a) $\theta_0 = 0.1$, (b) $\theta_0 = 0.2$, (c) $\theta_0 = 0.4$, and (d) $\theta_0 = 0.8$.

In order to describe the focusing performance, the DOF and the full-width at half-maximum (FWHM) of the focusing spot will be investigated. DOF is defined as the FWHM in the optical axis (z-axis) direction. To describe the impact of the longitudinally polarized component on the focused field, another parameter called beam quality is introduced. The beam quality η is defined as $\eta = \frac{\Phi_z}{\Phi_z + \Phi_r}$, where $\Phi_i = 2\pi \int_0^{r_0} |E_i(r, 0)|^2 r dr$ ($i = r$ and z) and r_0 is the first zero point of the field intensity distribution on the focal plane. In this study, the upper limit of the integration is larger than r_0 for the calculation of η. As previously discussed, $E_{\theta_0}^{\omega_0}(\theta)$ behaves like $\delta(\sin(\theta) - \theta_0)$ when ω_0 approaches 0. Therefore, a diffraction free beam can be obtained by taking advantage of the property of the $\delta(\cdot)$ function in the integral [137]. Theoretically, it indicates that the super-resolution

focusing is possible for small ω_0. In the following section, emphasis will be on analyzing the impact of θ_0.

3.1.2 Focusing performance of a radially polarized DG beam

To investigate the focusing performance of a radially polarized doughnut beam, NA and n are assumed to be 0.95 and 1.0, respectively. Therefore, α in Equation (3.2) is approximately 1.25 rad. Considering that DG has a Gaussian amplitude profile, θ_0 is no larger than $\arcsin\left(\frac{NA}{n}\right)$ rad, and the maximum intensity of the DG incident beam is exactly located at the output pupil's margin for $\theta_0 = \arcsin\left(\frac{NA}{n}\right)$. Due to the nature of the Bessel function, $E_r(0,z)$ is zero while $J_1(0) = 0$. Therefore, the maximum of the field intensity appears at the position $r \neq 0$ for different z. Obviously, the radially polarized component $E_r(r,z)$ will broaden the transversal width of the focusing spot. It means that a small focusing spot can be obtained by reducing the maximum intensity of the radially polarized component and adjusting the position where the maximum intensity appears. For $r = 0$, $J_0(0) = 1$ and $E_z(0,z)$ is the maximum for a chosen z. In this case, the radially polarized component does not contribute to the minimization of the focal spot.

In Figure 7, the focusing performance of the radially polarized DG beam with ($\omega_0 = 0.125$, $\theta_0 = 0.2$) and ($\omega_0 = 0.125$, $\theta_0 = 0.8$) is displayed. For the polarized DG beam with $\theta_0 = 0.2$, the focusing field is dominated by the radially polarized component as shown in Figure 7(a) - (d). The maximum intensity of the radially polarized component is approximately 0.98 at $r = 1.12\lambda$, and it is larger than that of the longitudinally polarized component with the maximum intensity around 0.23 at $r = 0$. Clearly, the maximum total field intensity cannot occur at the optical axis. But it will appear at $r = 1.12\lambda$. In this case, the beam quality is only $\eta = 11.53\%$ and the focusing field near $z = 0$ is dominated by the radial polarization component. Therefore, the focusing spot cannot be achieved at the preset focal point and the FWHM does not apply. It also indicates that the high NA lens failed to converge on the polarized DG beam with small θ_0. However, the maximum

intensity of the longitudinal polarization component increases with the increase of θ_0. Therefore, the longitudinally polarized component is gradually becoming predominant in the focusing field and the focusing spot will appear at the preset focal point. The corresponding beam quality soars up to 77.15%. Obviously, η is increasing with the increase of θ_0. It means that one can obtain a longitudinally polarized focusing field by using the radially polarized DG beam with a large θ_0. As shown in Figure 7(e) - (h), the FWHM is 0.52λ for $\theta_0 = 0.8$. Essentially, with the increase of θ_0, the radius of the DG beam increases. Previous results have indicated that the outer region of the incident beam contributes more to the longitudinally polarized component [127] - [128], [130]. Therefore, a large value of θ_0 will contribute more to the longitudinally polarized focusing spot for the DG incident beam.
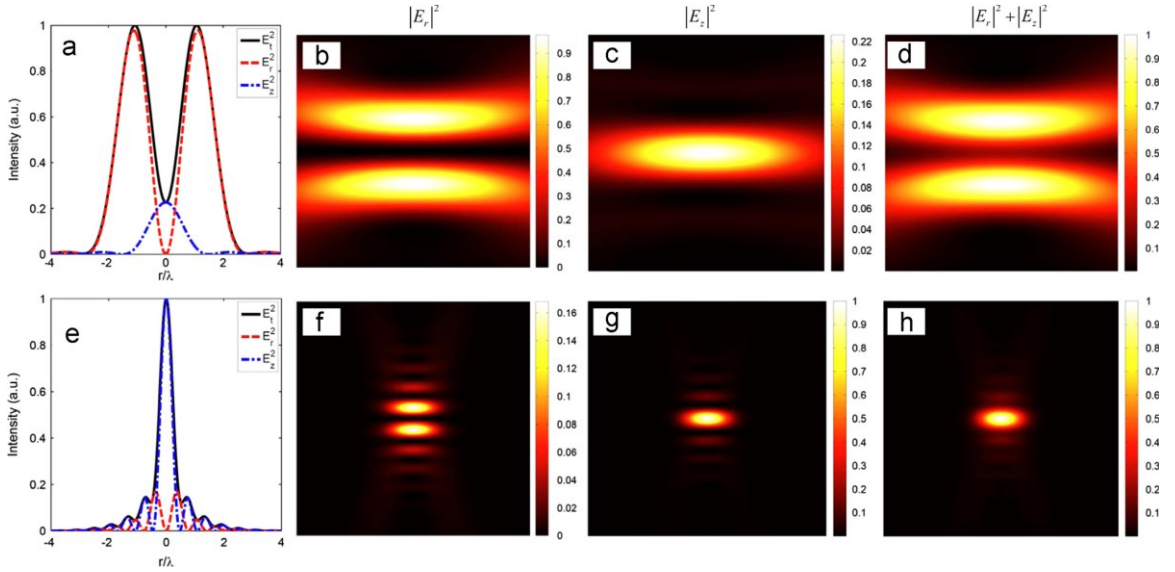
Figure 7 Field intensity distribution of a radially polarized DG beam focused by lens with NA = 0.95. ω_0 is 0.125. **(a)** - **(d)** $\theta_0 = 0.2$ and **(e)** - **(h)** $\theta_0 = 0.8$. **(a)** and **(e)** Intensity distribution on the focal plane $z = 0$. Dashed, dot-dashed and solid curve represent the radial component, the longitudinal component and the total field intensity, respectively. **(b)** - **(d)** and **(f)** - **(h)** Intensity distribution on the r - z plane. **(b)** and **(f)** Radial component $|E_r|^2$. **(c)** **(g)** Longitudinally polarized component $|E_z|^2$. **(d)** and **(h)** Total field $|E_r|^2 + |E_z|^2$.

In order to investigate the impact of θ_0 on the focusing performance, the maximum intensity of the radially (or longitudinally) polarized component and the corresponding

position on the focal plane are numerically calculated for the DG beams with different θ_0. When ω_0 is 0.125, the effect of θ_0 on the focusing performance is shown in Figure 8. The maximum intensity of the radially polarized component decreases from 0.99 to 0.05 with the increase of θ_0, as illustrated by the dot-dashed curve in Figure 8(a).
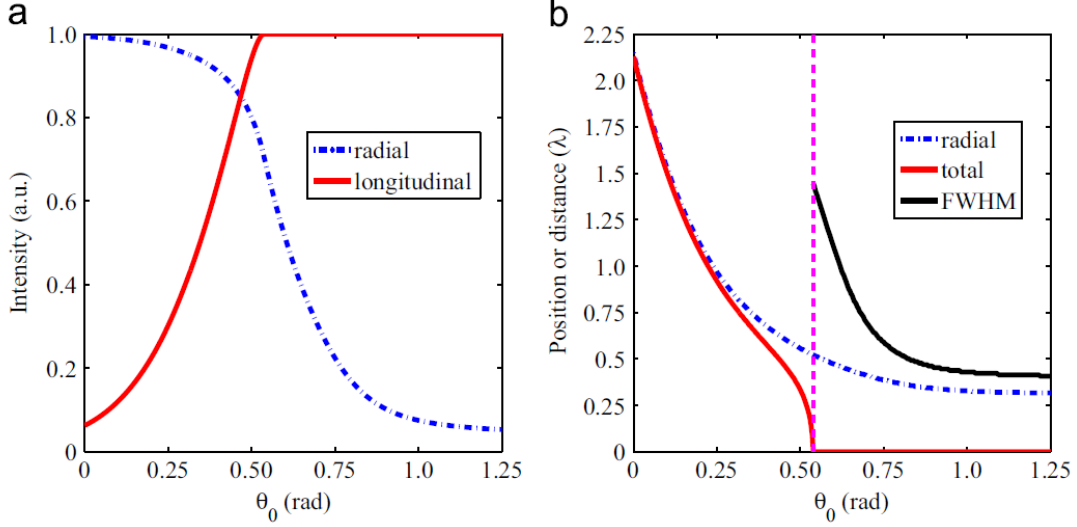
Figure 8 Focusing characteristics of the DG beam with $\omega_0 = 0.125$. **(a)** Maximum intensity value of the radial (dot-dashed curve) and the longitudinal (solid curve) component at the focal plane is varying with the increase of θ_0. **(b)** Dash-dotted curve represents the maximum intensity position of the radial component at the focal plane for different θ_0. Red solid curve represents the maximum intensity of the total field. Black solid curve describes the FWHM of the focusing spot on the focal plane. Dashed line marks the θ_0 when the maximum intensity of the total field appears at focal point.

However, the maximum intensity of the longitudinally polarized component increases with the increase of θ_0 while $\theta_0 < 0.54$. When $\theta_0 \approx 0.47$, the maximum intensity of the radially polarized component is approximately equal to that of the longitudinally polarized component. Therefore, a longitudinally polarized focusing field can be obtained by increasing θ_0 for the polarized DG beam. Meanwhile, as shown in Figure 8(b), the focusing performance can be improved by increasing the value of θ_0. For small θ_0, the maximum of the total field intensity will not occur at $r = 0$ on the focal plane. When θ_0 is larger than 0.54, the focusing field is at $(r = 0, z = 0)$. This trend is described by the dashed line in Figure 8(b). Obviously, the FWHM is slowly decreasing as θ_0 increases. However, the

33

focusing spot cannot be infinitely compressed by increasing θ_0. The impact of the longitudinally polarized component on the focusing field is investigated for varying θ_0 as shown in Figure 9. One can see that the beam quality η increases with the increase of θ_0. In conclusion, the focusing performance is influenced by three factors as shown in Figure 8 and Figure 9. Firstly, the radially polarized component is weakened with the increase of θ_0. Secondly, the peak of the radially polarized component is shifted close to $r = 0$ for large θ_0. Finally, the longitudinally polarized component is enhanced for large θ_0. Obviously, the first and final factors are helpful in obtaining the longitudinally polarized focusing field. While the second factor is important in improving the lateral resolution of the focusing field at the focal plane.
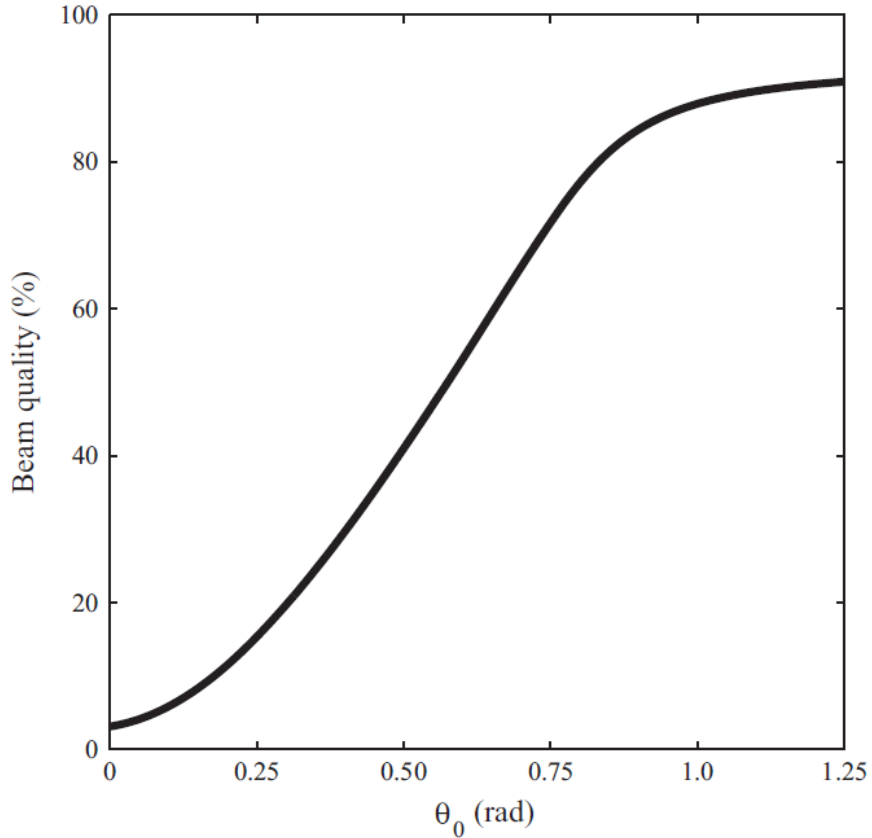
Figure 9 Beam quality of the focusing field at the focal plane for the DG incident beam with $\omega_0 = 0.125$ and θ_0 varying from 0 to 1.25.

In order to further describe the influence of θ_0, the focusing performance of the DG beam with $\theta_0 \approx 0.47$ is thoroughly investigated. The focusing performance of the DG beam with $\omega_0 = 0.125$ and $\theta_0 \approx 0.47$ is displayed in Figure 10 and Figure 11. Although the total field intensity at the focal point is increasing, null intensity appears at the center of the focal plane as shown in Figure 10(c) and the black solid curve in Figure 11. Obviously, a small focusing spot can be achieved with large θ_0 and small ω_0 for DG beam focused by the large NA lens.

In the previous content, it has been pointed out that the focusing characteristics of the DG beam behaves like $\delta(\sin(\theta) - \theta_0)$ when ω_0 is equal to 0. Thus, the difference of the focusing performance between the DG beam and the narrow width annular beam [18] can be further examined in the future. The FWHM increases with the increase of θ_0 for the DG beam. Meanwhile, the Gaussian distribution is reserved in the pupil. However, the narrow-width annular beam is center blocked. Therefore, the depth of focus is elongated for a narrow annular beam. In this case, the depth of focus and the FWHM decreases simultaneously.
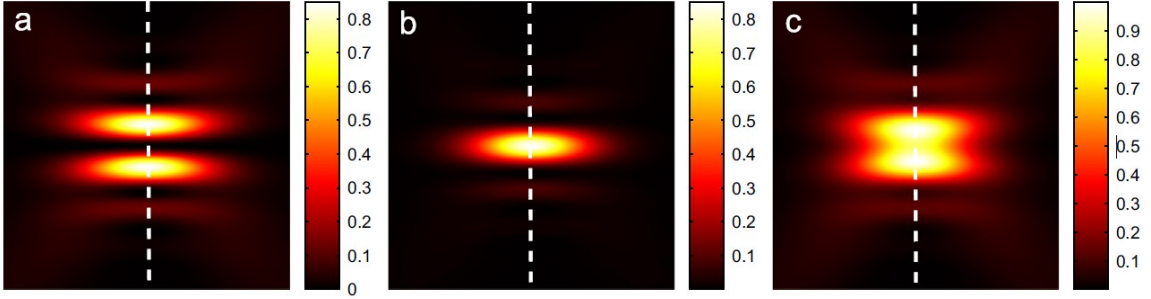
Figure 10 Focusing performance of the DG beam with $\omega_0 = 0.125$ and $\theta_0 = 0.467$. **(a)**, **(b)** and **(c)** Intensity distribution of the radial component, the longitudinal component and the total field intensity, respectively, on the *r-z* plane. *z* axis is ranging from -8λ to 8λ. *r* is ranging from 0 to 4λ. The focal plane is marked by the dashed line.
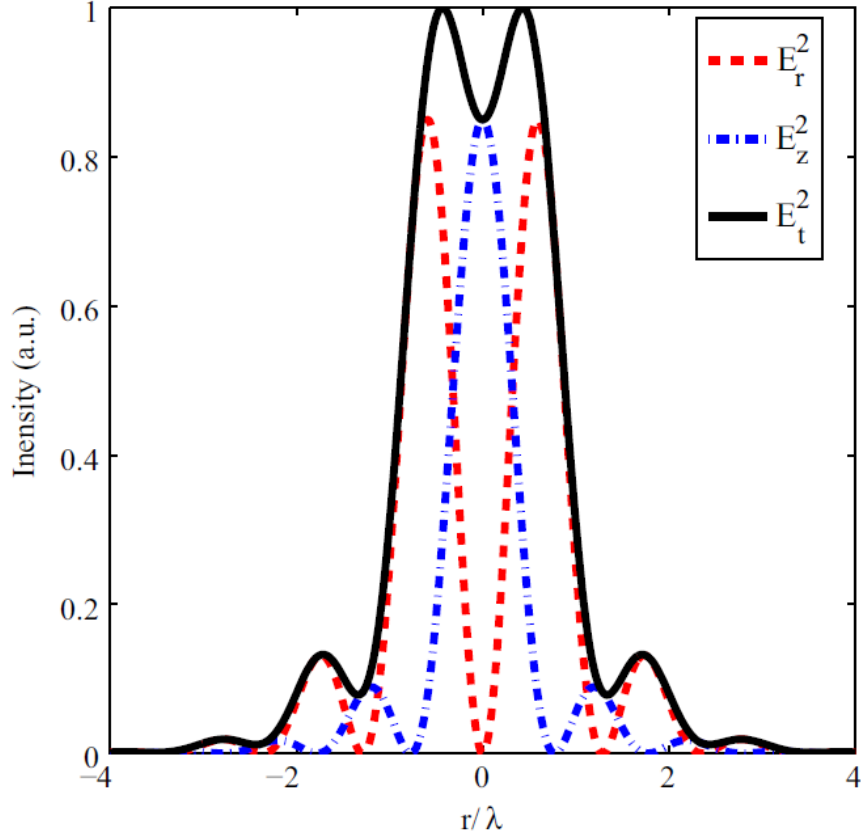
Figure 11 Intensity distribution at the focal plane $z = 0$ for the DG beam with $\omega_0 = 0.125$ and $\theta_0 = 0.467$. Dashed, dot-dashed and solid curve represent the radial component, the longitudinal component and the total field, respectively.

3.1.3 Summary

In this section, the focusing performance of the radially polarized DG beam by high NA lenses is investigated based on the Richards-Wolf integral theory [113] - [116]. The focusing performance, such as the FWHM and the intensity distribution at the focal plane, is systematically analyzed. Specifically, the effect of θ_0 on the focusing performance was discussed in detail. The magnitude distribution of the DG beam is controlled by ω_0 and θ_0. The position of the maximum intensity in the focusing field is determined by θ_0. When θ_0 is small, the DG beam failed to achieve focusing on the preset focal plane. While θ_0 is relatively large, one can easily obtain a sub-wavelength focusing spot and overcome the diffraction limit. Compared with the narrow width annular beam, the depth of focus and

the FWHM decrease simultaneously for the DG incident beam. The DG beam has potential application in the field of super-resolution microscopy and high density optical storage.

3.2 COMPLEX AMPLITUDE FILTER DESIGN FOR LONG DOF FOCUSING IN A HIGH NA FOCUSING SYSTEM

In Equation (2.21), the exponential component $e^{ikz\cos\theta}$ determines the longitudinal distribution of the focusing field. The center of the focusing field is at $z = 0$. In order to increase the depth of focus of the focusing field, a complex amplitude filter based on the cosine function is designed and validated for radially polarized incident beams.

3.2.1 Complex amplitude filter design

The complex amplitude filter can be mathematically expressed by Equation (3.3):

$$F_N(\theta) = \sum_{p=1}^{N} c_p \cos(km_p \cos\theta) \tag{3.3}$$

where c_p is an amplitude adjustment parameter, m_p is displacement distance along the optical axis (z-axis), N is the number of the cosine functions, and k is the wavenumber of the incident beam. Considering Equation (3.3) describes the transmission amplitude, it should be normalized by the maximal absolute value of $F_N(\theta)$. Once $F_N(\theta)$ is introduced, $l_0(\theta)$ can be replaced by $l_0(\theta)F_N(\theta)$.

Now let's take $N = 1$ as an example to explain the working principle of the designed complex amplitude filter. When $N = 1$, the complex amplitude filter can be written as:

$$F_1(\theta) = c_1 \cos(km_1 \cos\theta) \tag{3.4}$$

According to Euler transformation, cosine function can be expressed in terms of the summation of two exponential functions:

$$cos\phi = \frac{1}{2}[\exp(i\phi) + \exp(-i\phi)] \tag{3.5}$$

Therefore Equation (3.4) can be rewritten as follows by substitute Equation (3.5) into Equation (3.4):

$$F_1(\theta) = c_1 \cos(km_1 cos\theta) = \frac{c_1}{2}[\exp(ikm_1 cos\theta) + \exp(-ikm_1 cos\theta)] \tag{3.6}$$

According to Equation (2.21), the focusing field for the incident beam $l_0(\theta)F_1(\theta)$ can be expressed as:

$$E_r(r,z) =$$
$$\frac{c_1}{2}A \int_0^{\theta_{max}} P(\theta)\sin(2\theta)J_1(krsin\theta)l(\theta)[e^{ik(z+m_1)cos\theta} + e^{ik(z-m_1)cos\theta}]d\theta \tag{3.7}$$

In principle, Equation (3.7) can be rewritten in a much simpler format:

$$E_r(r,z) = \frac{1}{2}[E_r(r,z+m_1) + E_r(r,z-m_1)] \tag{3.8}$$

It is clear from Equation (3.9) that the incident beam will be focused at $z = +m_1$ and $z = -m_1$ when the $N = 1$ complex amplitude filter is introduced. In principle, the focusing field can be designed to achieve long DOF by optimizing the m_p parameter of the complex amplitude filter.

To better understand how this complex amplitude filter can be used to engineer the focusing field, we introduce this filter to a high NA focusing system. Assuming NA $= 0.95$ and the incident beam is a radially polarized Bessel-Gaussian beam (BG). The BG can be described by the following equation:

$$l(\theta) = \exp\left[-\beta^2 \left(\frac{sin\theta}{sin\alpha}\right)^2\right]J_1\left(2\gamma\frac{sin\theta}{sin\alpha}\right) \tag{3.9}$$

Where $\alpha = \arcsin\left(\frac{NA}{n}\right)$, β and γ are the two parameters that control the amplitude profile of the BG incident beam. When there is no complex amplitude filter applied to the focusing system, the intensity of the radial component, the longitudinal component and the total field at the focal plane $z = 0$ along a radial axis for the BG with $\beta = 1$ and $\gamma = 1$ can be calculated using Equation (2.21). The results are shown in Figure 12.
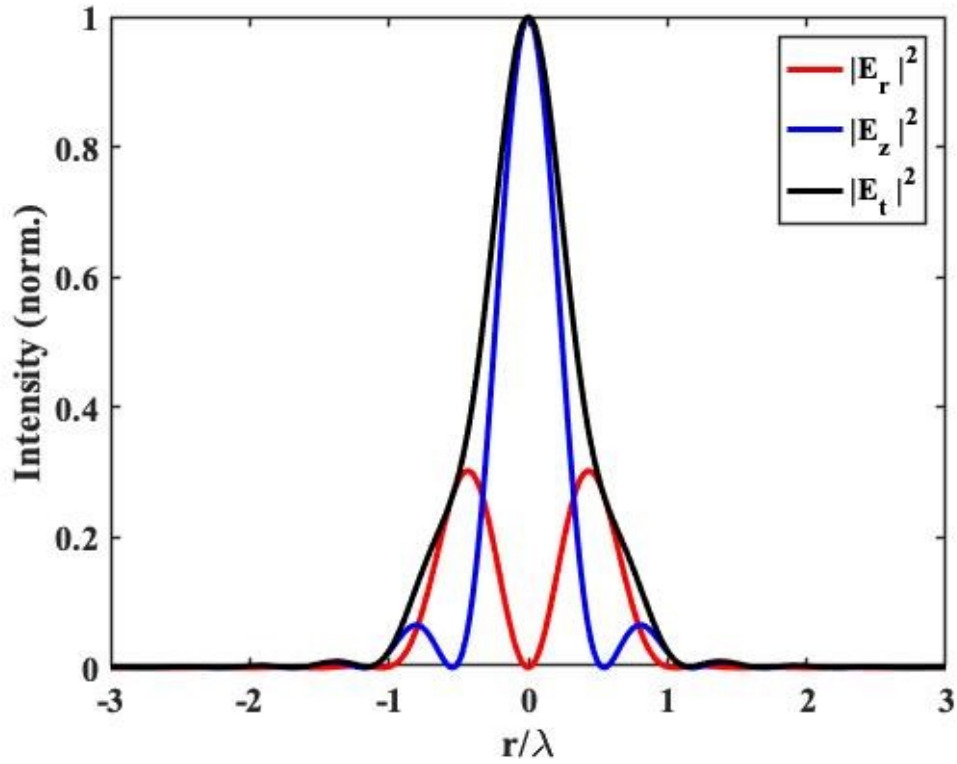
Figure 12 Intensity distribution at the focal plane $z = 0$ along a radial axis for the BG with $\beta = 1$ and $\gamma = 1$. NA = 0.95. Red, blue and black curves represent the radial component, the longitudinal component and the total field, respectively.

Figure 13 shows the intensity of the radial component, the longitudinal component and the total field along the optical axis. The DOF in this case is approximately 0.8λ.
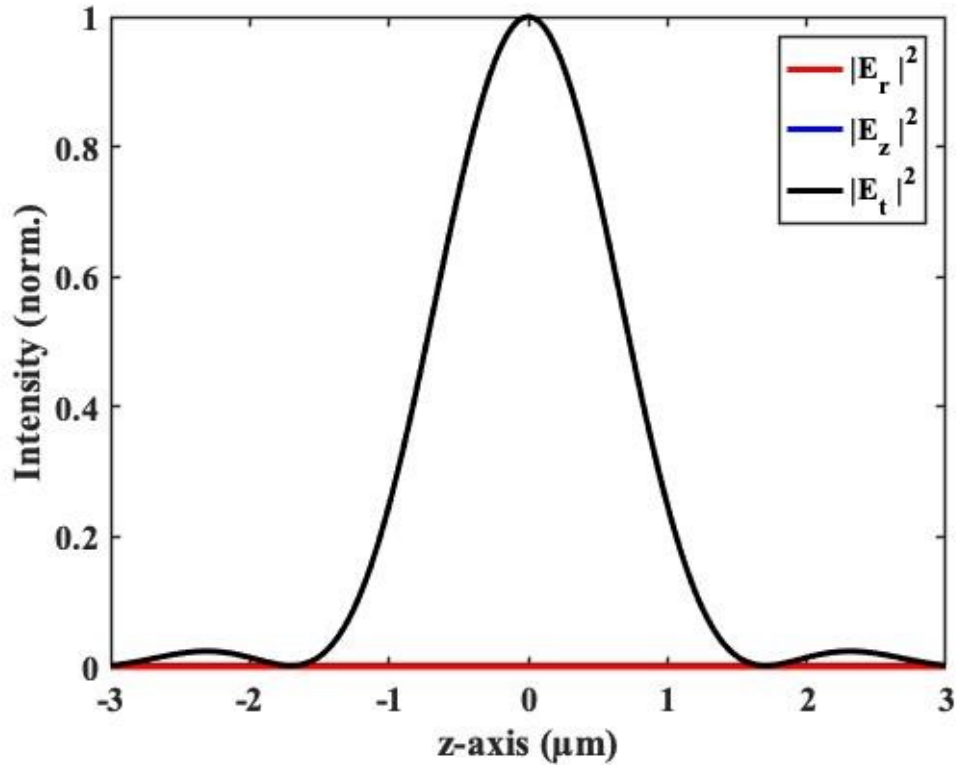
Figure 13 Intensity distribution along the optical axis direction for the BG with $\beta = 1$ and $\gamma = 1$. NA = 0.95. Red, blue and black curves represent the radial component, the longitudinal component and the total field, respectively.

If we apply a simple N = 1, $c_1 = 1, m_1 = 0.9$ cosine function based complex amplitude filter to the same high NA focusing system, the filter will split the focusing field into two spots located 1.8λ apart from each other. This will effectively increase the depth of focus of the focusing system. The profile of the complex amplitude filter is shown in Figure 14. The focusing field intensity calculation results for the longitudinal and radial directions are shown in Figure 15.
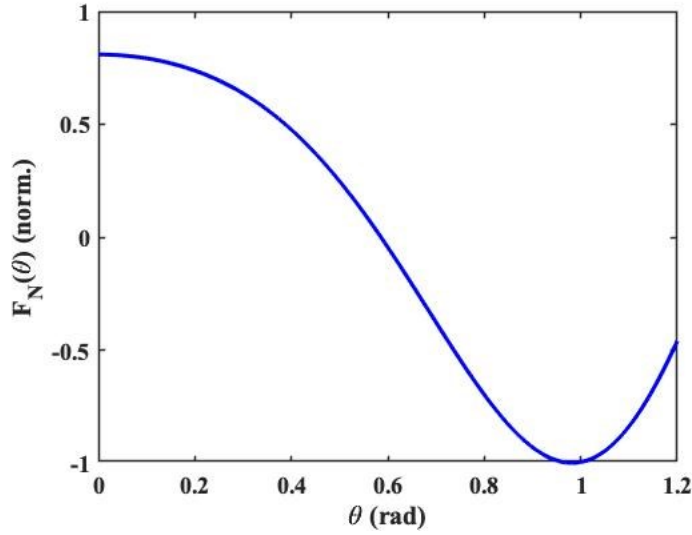
Figure 14 The profile of the cosine function based complex amplitude filter when N = 1, and $c_1 = 1, m_1 = 0.9$.

From Figure 15(b) we can see that the DOF has been improved significantly compared to Figure 13. The calculation results show that the DOF is approximately 2.2λ after the simple N=1, $c_1 = 1, m_1 = 0.9$ complex amplitude filter has been employed. It's almost three times longer than the one without the complex amplitude filter.
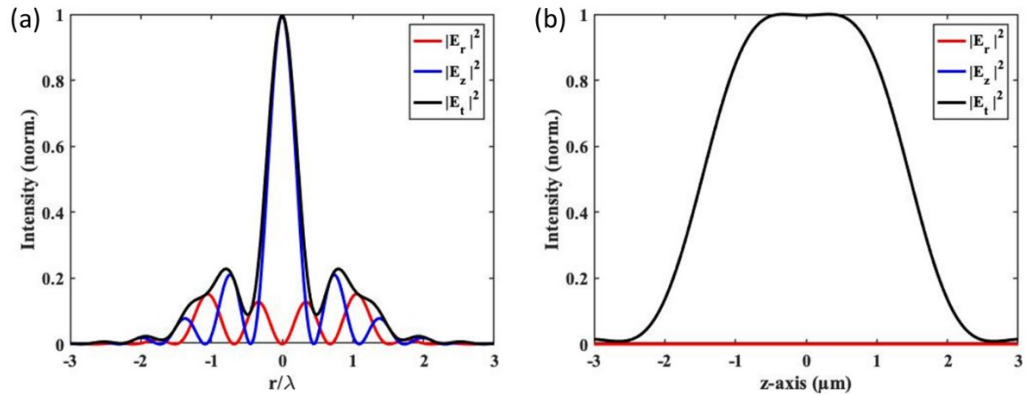
Figure 15 **(a)** Intensity distribution at the focal plane $z = 0$ along a radial axis and **(b)** Intensity distribution along the optical axis for the BG incident beam with $\beta = 1$ and $\gamma = 1$. NA = 0.95. Red, blue and black curves represent the radial component, the longitudinal component and the total field, respectively. The cosine function based complex amplitude filter, N = 1, and $m_1 = 0.9$, is applied in this case.

41

3.2.2 Simplified complex amplitude filter design

In Equation (3.3), there are two parameters c_p and m_p need to be determined to design a filter. To simplify the complex amplitude filter design process, a modulation factor $(2p - 1)$ is introduced to replace c_p in Equation (3.3). The modified complex amplitude filter can be mathematically expressed as:

$$F_N(\theta) = \sum_{p=1}^{N} \cos[km_p(2p - 1)\cos\theta] \tag{3.10}$$

Figure 16 demonstrates the filter profiles for three different cosine based complex amplitude filters. These three filters have different N values. They will be introduced to the same high NA focusing system and their performance will be discussed in detail.
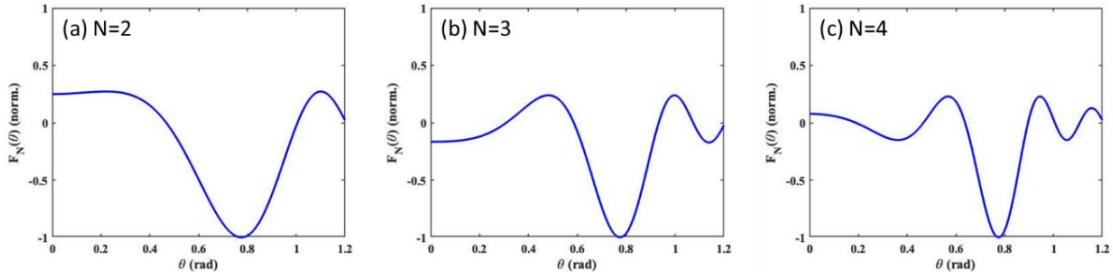
Figure 16 The profile of the modified complex amplitude filter when N = 2, 3, and 4. $m_1 = 0.7$ for all cases.

Figure 17 and Table 1 summarize the performance of the designed filters with different N values. Obviously, the DOF increases significantly with the increase of the number of cosine functions employed in the complex amplitude filter. The DOF reaches 9.6λ when N = 4, and $m_p = 0.7$ filter is used. Optimization algorithms can be used to tailor the focusing field according to specific application scenarios. Parameter m_p must be carefully chosen in the filter design process in order to achieve uniform and long DOF focusing field.
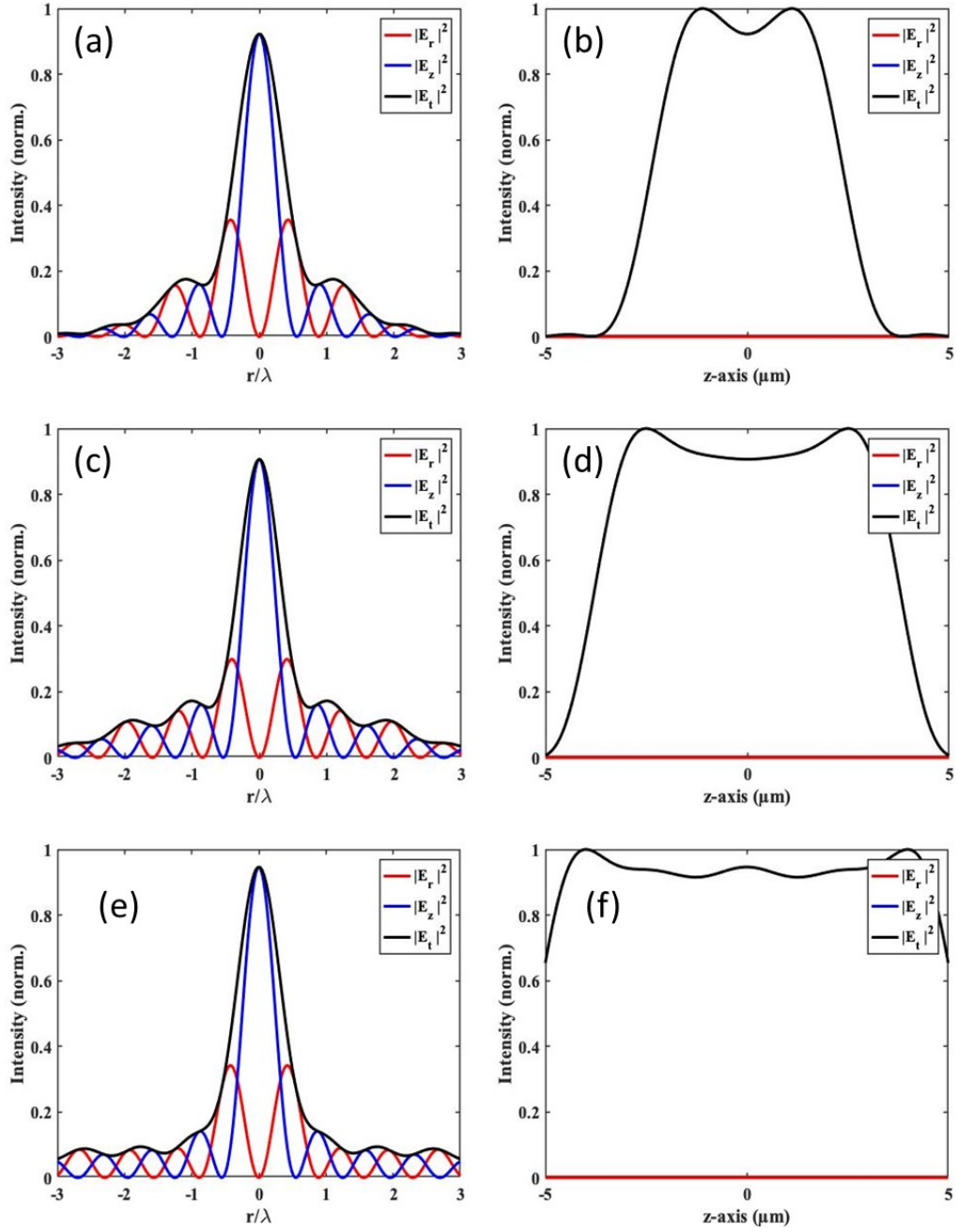
Figure 17 **(a)**, **(c)** and **(e)** represents the intensity distribution at the focal plane $z = 0$ along a radial axis. **(b)**, **(d)** and **(f)** represents the intensity distribution along the optical axis. The incident beam is the BG with $\beta = 1$ and $\gamma = 1$. NA = 0.95. Red, blue and black curves represent the radial component, the longitudinal component and the total field, respectively. A cosine function based complex amplitude filter, **(a)**, **(b)** N = 2, $m_p = 0.7$; **(c)**, **(d)** N = 3, $m_p = 0.7$; **(e)**, **(f)** N = 4, $m_p = 0.7$, is applied to the high NA focusing system.

Table 1 Comparison of the focusing performance of different cosine function based complex amplitude filter designs. The incident beam is the BG with $\beta = 1$ and $\gamma = 1$. NA $= 0.95$.

Filter Design	DOF	FWHM
No filter	0.8	0.68
N = 2, $m_p = 0.7$	3.8	0.84
N = 3, $m_p = 0.7$	6.6	0.74
N = 4, $m_p = 0.7$	9.6	0.80

In order to design a focusing field with a long depth of focus, choose large N and m_p values first so that the focusing field can be split into multiple individual focusing spots. Then the parameter m_p can be further optimized based on the FWHM of each focusing spots and their locations on the optical axis. For example, Figure 18(a) illustrates the focusing field when N $= 5$ and $m_p = 3$. Obviously, 10 individual focusing spots can be observed because N $= 5$. A value for m_p can be easily found after a quick calculation of FWHM of each focusing spot and their locations on the optical axis. In this case, $m_p = 0.7$ is chosen and the result is shown in Figure 18(b). A long DOF focusing field is successfully achieved. High performance filters can be designed utilizing advanced optimization algorithms.
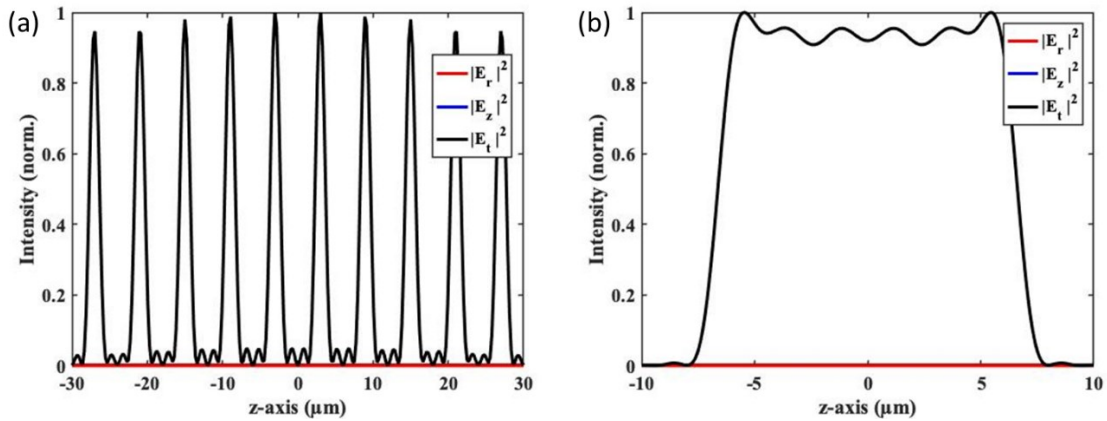
Figure 18 The intensity distribution along the optical axis for (a) N $= 5$, $m_p = 3$, and (b) N $= 5$ and $m_p = 0.7$. The incident beam is the BG beam with $\beta = 1$ and $\gamma = 1$. NA $= 0.95$. Red, blue and black curves represent the radial component, the longitudinal component and the total field, respectively.

When the parameter N increases to a particular level, only a certain region in the filter has relatively high transmittance. When N approaches infinity, the transmittance function of the cosine based complex amplitude filter will become a two-dimensional δ function. The filter becomes an infinitely narrow ring filter. Figure 19 shows the cosine function based complex amplitude filter profile when N = 10000, $m_p = 0.6$.
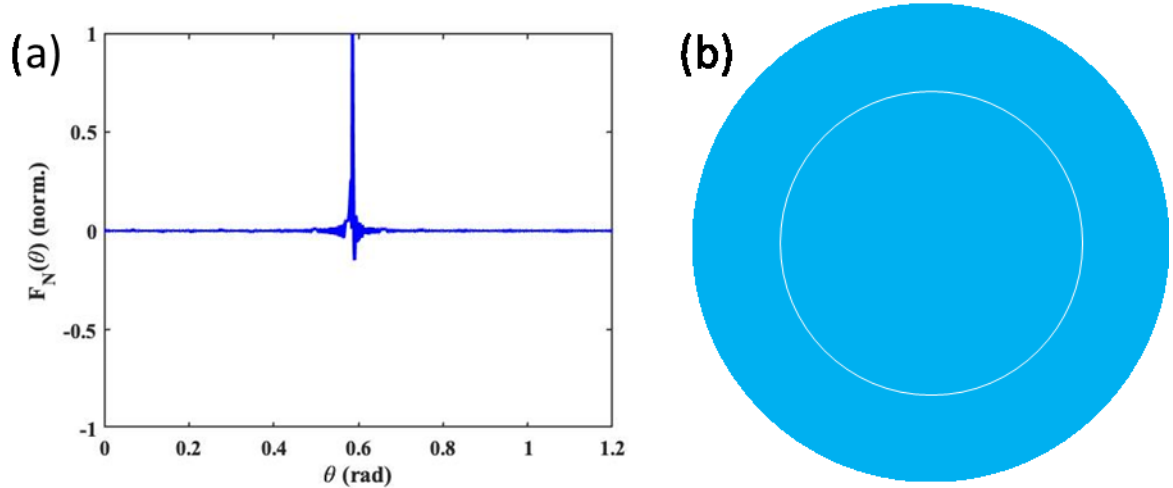
Figure 19 The (a) profile and (b) a schematic drawing of the cosine function based complex amplitude filter profile when N = 10000, $m_p = 0.6$.

3.3 CYLINDRICAL VECTOR BEAM ENGINEERING FOR LONG DOF FOCUSING IN A HIGH NA FOCUSING SYSTEM

In this section, cosine function based complex amplitude filters are applied to a high NA focusing system to achieve long DOF focusing field. The performance of the complex amplitude filter in each application is discussed in detail.

3.3.1 Generation of longitudinally polarized optical chain using 4π focusing system

High NA focusing systems illuminated by radially polarized beams are drawing plenty of attentions due to their ability to generate various focusing patterns, which may find applications in areas such as super-resolution focusing, optical lithography, microscopy

imaging and particle manipulation [120], [122], [138], [139]. High-density optical data storage has been experimentally demonstrated by focusing a radially polarized beam in [120]. To obtain a desired focusing field, beam engineering methods such as far-field apodization and complex amplitude filtering have been applied to a polarized incident beam in a high NA focusing system [122], [131], [140] - [141]. As a result, super-resolution spot [120], [140], optical needle [122], [131], [142], bottle-hollow beam [141], optical chain [143] - [145] and spherical spot [146] - [148] have been achieved numerically or experimentally. For example, a sharp focus generated by a radially polarized beam was experimentally verified for the first time in 2003 [140]. In 2008, a longitudinally polarized optical needle was first generated in a high NA focusing system with the radially polarized Bessel-Gaussian incident beam modulated by a binary phase optical element [122].

Among various types of focusing patterns, an optical chain, which is an array of either bright focusing spots or dark spots, has been widely investigated for its ability to trap multiple particles and multilayer data recording [143] - [145], [149] - [153]. Polarization control method, amplitude filter and dipole source reverse method have been proposed to produce multiple focusing spots [144], [147], [154]. A quasiperiodic optical chain was produced using a diffractive optical element illuminated by a radially polarized beam [143]. Multiple equidistant focusing spots were created by a complex amplitude filter [150]. However, high axial resolution, longitudinal polarization and multiple controllable focusing spots have not been achieved simultaneously. In this section, a longitudinally (z-axis) polarized optical chain is achieved in a 4π focusing system with a complex amplitude filter. The illuminating beam is radially polarized. The axial resolution can be remarkably improved in a 4π focusing system with high NA [155], [156]. To analyze the focusing performance of the high NA focusing system, the vectorial Debye integral is employed [116]. The radially polarized component of the focusing field is destructive interference at the focusing spot on the optical axis. Therefore, the optical chain is highly longitudinally polarized with axial super-resolution. More uniform-intensity focusing spots on the optical chain can be easily obtained by adjusting parameters of the proposed filter.

As shown in Figure 20, a 4π focusing system is composed of two high NA lenses directly facing each other. The two lenses are arranged in such a way that their optical axes and foci are overlapped. If the focusing fields of the left and right incident beams are $E_{left}(r, z)$ and $E_{right}(-r, -z)$, respectively, the total electrical field $E(r, z)$ is expressed as [22]:

$$E(r, z) = E_{left}(r, z) + E_{right}(-r, -z) \tag{3.11}$$

where the negative sign in front of r represents the opposite polarization direction of the right beam relative to the left beam. The negative sign in front of z represents the opposite incident direction. For a high NA lens illuminated by the radially polarized beam, the electric field near the focus $z = 0$ is governed by Richards-Wolf's integral [113] - [116]. Therefore, for the left radially polarized BG incident beam, the radially polarized component $E_r(r, z)$ and the longitudinally polarized component $E_z(r, z)$ can be expressed as follows [116]:

$$E_r(r, z) = A \int_0^\alpha l(\theta)\sqrt{\cos\theta}\, \sin(2\theta) J_1(kr\sin\theta)e^{ikz\cos\theta}\, d\theta \tag{3.12A}$$

$$E_z(r, z) = 2iA \int_0^\alpha l(\theta)\sqrt{\cos\theta}\sin^2\theta J_0(kr\sin\theta)e^{ikz\cos\theta}\, d\theta \tag{3.12B}$$

where A is a constant coefficient and $\alpha = \arcsin\left(\frac{NA}{n}\right)$. $J_0(\cdot)$ and $J_1(\cdot)$ respresents the zero- and first-order Bessel function of first kind, respectively. $\sqrt{\cos\theta}$ is the pupil apodization function obeying the sine condition. $k = \frac{2\pi}{\lambda}$ is the wave number and λ is the wavelength. $l(\theta)$ is the amplitude profile of the BG incident beam given by [122]:

$$l(\theta) = \exp\left[-\beta^2 \left(\frac{\sin\theta}{\sin\alpha}\right)^2\right] J_1\left(2\gamma \frac{\sin\theta}{\sin\alpha}\right) \tag{3.13}$$

where β and γ are the parameters that determine the amplitude profile of the BG incident beam.

In order to obtain the longitudinally polarized optical chain, a complex amplitude filter based on the cosine function is introduced as follows [131], [150]:

$$F_N(\theta) = \sum_{p=1}^{N} c_p \cos[km_p(2p-1)\cos\theta] \qquad (3.14)$$

where c_p is an amplitude factor and m_p is a displacement along the optical axis. N is the number of the cosine function. The field intensity of the optical chain is determined by c_p and m_p, while the focusing spot number on the optical chain is determined by N. $F_N(\theta)$ is normalized because the transmissivity of the filter cannot be larger than 1. The BG incident beam in Equation (3.13) will be replaced by $l(\theta)F_N(\theta)$ after it has been modulated by the complex amplitude filter.
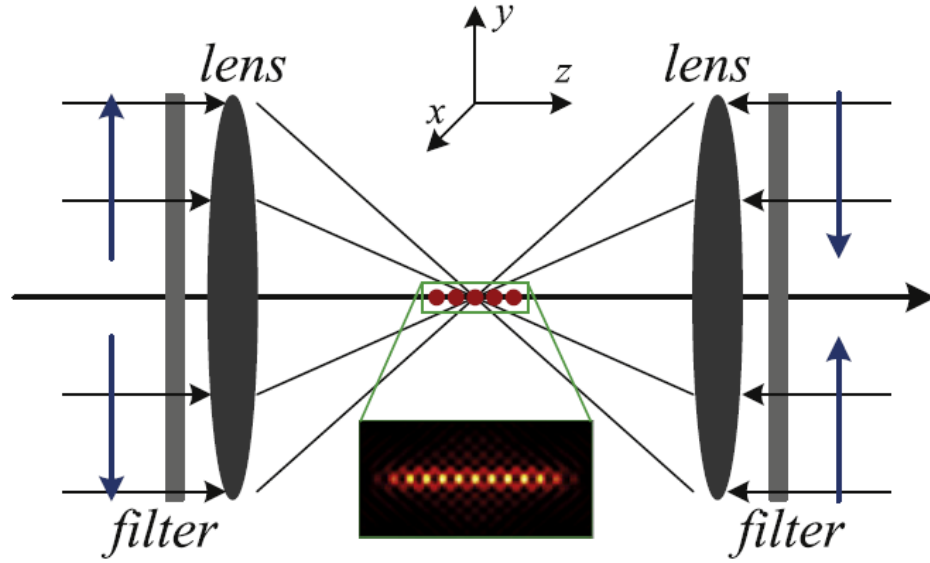
Figure 20 Schematic of a 4π high NA focusing system integrated with complex amplitude filters illuminated by two counter-propagating radially polarized BG. The blue arrows represent the directions of radial polarization vectors. Lower inset: generated longitudinally polarized tight focusing optical chain.

Based on Equations (3.11) - (3.14), the field intensity distribution near the focal spot $z = 0$ of a high NA 4π focusing system shown in Figure 20 can be easily obtained. Here, we assume that NA = 0.95, n = 1.0 and $\alpha \approx 1.25$. β and γ are set to 1.0 in Equation (3.13).

For each lens illuminated by the radially polarized BG, the corresponding intensity distribution is displayed in Figure 21. The FWHM Δr of the focusing spot on the focal plane is approximately 0.68λ [122]. The DOF Δz is about 1.45λ. The focusing spot can be treated as a prolate ellipsoid. The volume of the focusing spot is approximately $2.81\lambda^3$ using the volume formula $V = \frac{4\pi(\Delta r)^2 \Delta z}{3}$, where Δr and Δz are FWHM and DOF of a focusing spot, respectively [120], [157]. Additionally, the polarization conversion efficiency η is defined as $\eta = \frac{\Phi_z}{\Phi_r + \Phi_z}$, where $\Phi_{r(z)} = 2\pi \int_0^{r_0} \left| E_{r(z)}(r,0) \right|^2 r dr$ and $r_0 = 0.5\Delta r$ [122]. The calculated polarization conversion efficiency η for the aforementioned single lens focusing system is approximately 85%.
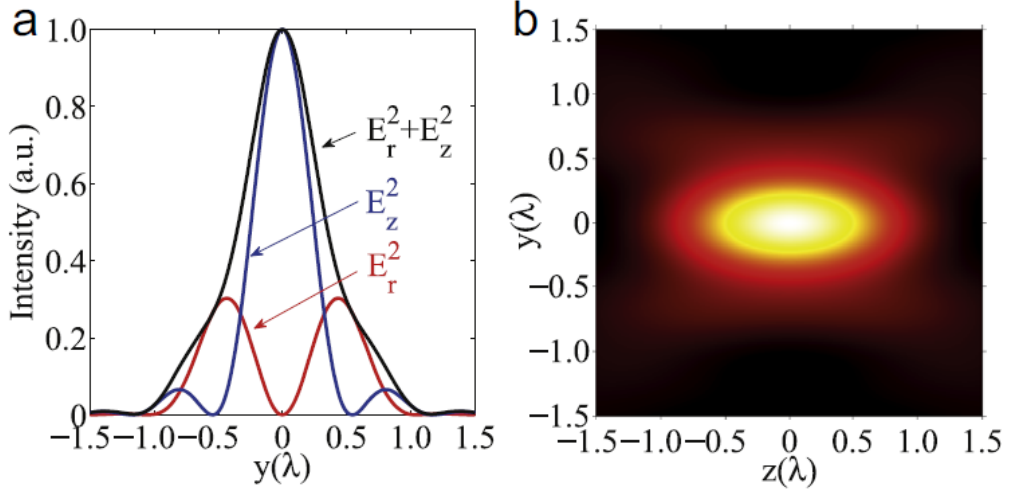
Figure 21 Intensity distribution in the focal region of a tight focusing lens with NA = 0.95 illuminated with a radially polarized BG. NA is 0.95. **(a)** Radial, longitudinal and total intensity distribution on the focal plane. **(b)** Intensity distribution on the y-z plane. The FWHM and DOF are 0.68λ and 1.45λ, respectively.

Based on the preceding discussion, one can see that the FWHM and DOF of the focusing spot are quite large in a single lens focusing system. A super-resolution DOF optical chain can be obtained when the complex amplitude filter as described in Equation (3.14) is applied to a 4π focusing system. NA of both lenses is chosen as 0.95. In order to obtain an optical chain with uniform intensity, the complex amplitude filter with N = 1, $c_1 = 1$ and $m_1 = 0.914$ is adopted in the 4π focusing system. The corresponding field intensity

distribution near the focal region is shown in Figure 22. Among the five focusing spots on the optical axis, three spots have approximately equal intensity. The focusing field is clearly elongated along the optical axis by the designed complex amplitude filter. The position (r, z) of the three spots are shown in Figure 22(b) and Table 2.
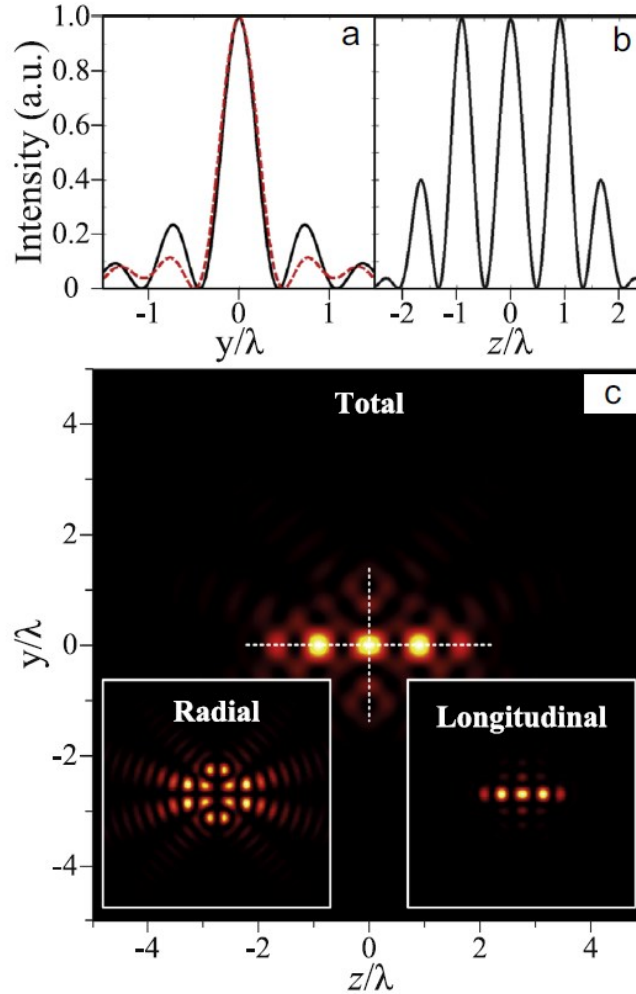
Figure 22 Intensity distribution in the focal region of the 4π focusing system illuminated by a radially polarized BG modulated by the complex amplitude filter with $N = 1$, $c_1 = 1$ and $m_1 = 0.914$. **(a)** Lateral intensity distribution on the focal plane (solid curve) and on the plane $z = \pm0.91\lambda$ (dashed curve). **(b)** Axial intensity along the horizontal dashed line in **(c)**. **(c)** Total intensity distribution in the y-z plane. The vertical and horizontal dashed lines represent the y- and z-axis, respectively. Insets, the intensity distribution of the radially and longitudinally polarized component.

Table 2 Optical chain generated by 4π focusing system illuminated by radially polarized BG with complex amplitude filters.[a]

Serial No.	-3	-2	-1	0	1	2	3
N=1							
Position (λ)	-	-	-0.91	0	0.91	-	-
FWHM (λ)	-	-	0.45	0.42	0.45	-	-
DOF (λ)	-	-	0.42	0.49	0.42	-	-
N=2							
Position (λ)	-	-1.41	-0.71	0	0.71	1.41	-
FWHM (λ)	-	0.51	0.51	0.50	0.51	0.51	-
DOF (λ)	-	0.35	0.36	0.36	0.36	0.35	-
N=3							
Position (λ)	-2.09	-1.40	-0.71	0	0.71	1.40	2.09
FWHM (λ)	0.52	0.52	0.51	0.51	0.51	0.52	0.52
DOF (λ)	0.34	0.35	0.36	0.36	0.36	0.35	0.34

[a]Serial numbers of the focusing spot in the optical chain are in the first row. 0 indicates the focusing spot is located at the focus point. Negative sign represents the opposite direction of z-axis.

For the focusing spot located at the focus, the lateral intensity distribution on the focal plane is displayed as the solid curve in Figure 22(a). The FWHM is approximately 0.42λ, which is smaller than half of the wavelength. Obviously, it achieves super-resolution. For a radially polarized incident beam, the focusing field is composed of both radial and longitudinal components. Because the maximum of the radial component is not on the optical axis, the size of the focusing spot will increase by this component. However, the intensity of the radial component at the focal plane diminishes due to the destructive interference. As shown in the inset of Figure 22(c), the intensity of the radial component on the focal plane is zero and it is very small near the focal spot. Therefore, the resolution is enhanced in this system. The analysis can be applied to the other two focusing spots on the optical axis. The DOF is 0.49λ, which is only one-third the size of the focusing spot in a single lens focusing system with the same parameters [122]. The spot volume is approximately $0.36\lambda^3$. Meanwhile, the focusing field is symmetric with respect to the $z = 0$ plane. The focusing spots located at $(0, \pm 0.91\lambda)$ are identical. Their FWHM and DOF are 0.45λ and 0.42λ, respectively. The DOFs of the three focusing spots on the optical chain are approximately equal. Obviously, the axial resolution is improved in the 4π system with NA = 0.95. As shown in Figure 22(a), the lateral intensity distributions of the main lobe of

the three focusing spots are almost the same because the solid and the dashed curves between the first two zero points are nearly overlapping. The secondary maximum is different. The value is much smaller than that at $r = 0$. It does not affect the resolution of the main lobe. The corresponding spot volume is approximately $0.36\lambda^3$. The volume is about one-eighth that of a focusing spot produced in a single lens focusing system. The resolution of the focusing spot produced in 4π focusing system is improved significantly. The improvement in resolution is mainly due to the decrease in DOF of the focusing spot produced by the constructive interference at the position where the focusing spot is located. As shown in the insets of Figure 22(c), the intensity of the radially polarized component along the y-axis is zero. The middle focusing spot is completely longitudinally polarized. Because the radially polarized component disappears, the FWHM of the longitudinally polarized focusing spot decreases sharply. It can achieve super-resolution in the lateral direction. For the convenience of description, the focusing spots located at $z = \pm 0.91\lambda$ are called side focusing spots. It is obvious from Figure 22 that the intensity of the radially polarized component on the cross-section $z = \pm 0.91\lambda$ is significantly smaller than that of the longitudinally polarized component. A highly longitudinally polarized super-resolution optical chain is achieved. Specifically, it is necessary to point out the difference between the multiple focusing spots in the optical chain and the equidistant multi-focus generated by a single lens focusing system [150]. The equidistant multi-focus was directly generated by a complex amplitude filter described by Equation (3.14) and a single lens focusing system. Therefore, the FWHM and DOF of the focusing spots on the equidistant multi-focus are as large as that of the focusing spot shown in Figure 21. In contrast, the FWHM and DOF of the focusing spots on the optical chain are smaller than half of the wavelength and can achieve super-resolution. Additionally, the focusing spots on the optical chain are highly longitudinally polarized. The equidistant multi-focus has both radially and longitudinally polarized components.

Previously, the optical chain with three uniform intensity spots was achieved with $N = 1$. One can easily obtain a long optical chain with more uniform intensity focusing spots by increasing N in Equation (3.14). In Figure 23, the optical chains with five and seven focusing spots are displayed for $N = 2$ and 3. When $N = 2$, c_p and m_p are chosen as $c_1 = $

$c_2 = 1$, $m_1 = 0.75$ and $m_2 = 2.1$, respectively. As shown in Figure 23(c) and (d), there are five uniform spots along the optical axis with intensity fluctuation less than 2%. The FWHM of the five spots is approximately 0.50λ. It can be seen that the main lobes of the lateral intensity distribution of the five spots are nearly overlapping as shown in Figure 23(a). As shown in Table 2, the DOF of the five focusing spots on the optical chain is approximately 0.35λ, which is one-fourth of that in the single lens. The focusing spots are sub-diffraction limit in the longitudinal direction. The shapes of the five spots are similar and their spot volumes are around $0.38\lambda^3$. Meanwhile, the intensity of the radially polarized component is much less than that of the longitudinally polarized component. Therefore, the obtained optical chain has a high axial resolution and small volume and it is highly longitudinally polarized.

As shown in Figure 23(b), (c) and (e), the optical chain with seven uniform intensity spots, whose intensity fluctuation is less than 2%, is obtained for N = 3. Shown in Table 2, the FWHM on the focal plane is 0.51λ, while others are either 0.51λ or 0.52λ. The DOF is ranging from 0.34λ to 0.36λ. Meanwhile, the spot volume does not exceed $0.41\lambda^3$. Due to the destructive interference of the radially polarized component at the positions where the focusing spots are located, the obtained optical chain is highly longitudinally polarized. When the parameter N increases from 1 to 3, the number of focusing spots on the optical chain increases from 3 to 7. The length of the optical chain is elongated with the increase of N as well. Essentially, the number of focusing spots in the optical chain is equal to 2N + 1. When N is quite large, more c_p and m_p ($p = 1, ..., N$) need to be determined. In this case, an optimization algorithm can be developed in order to obtain optimal c_p and m_p efficiently.
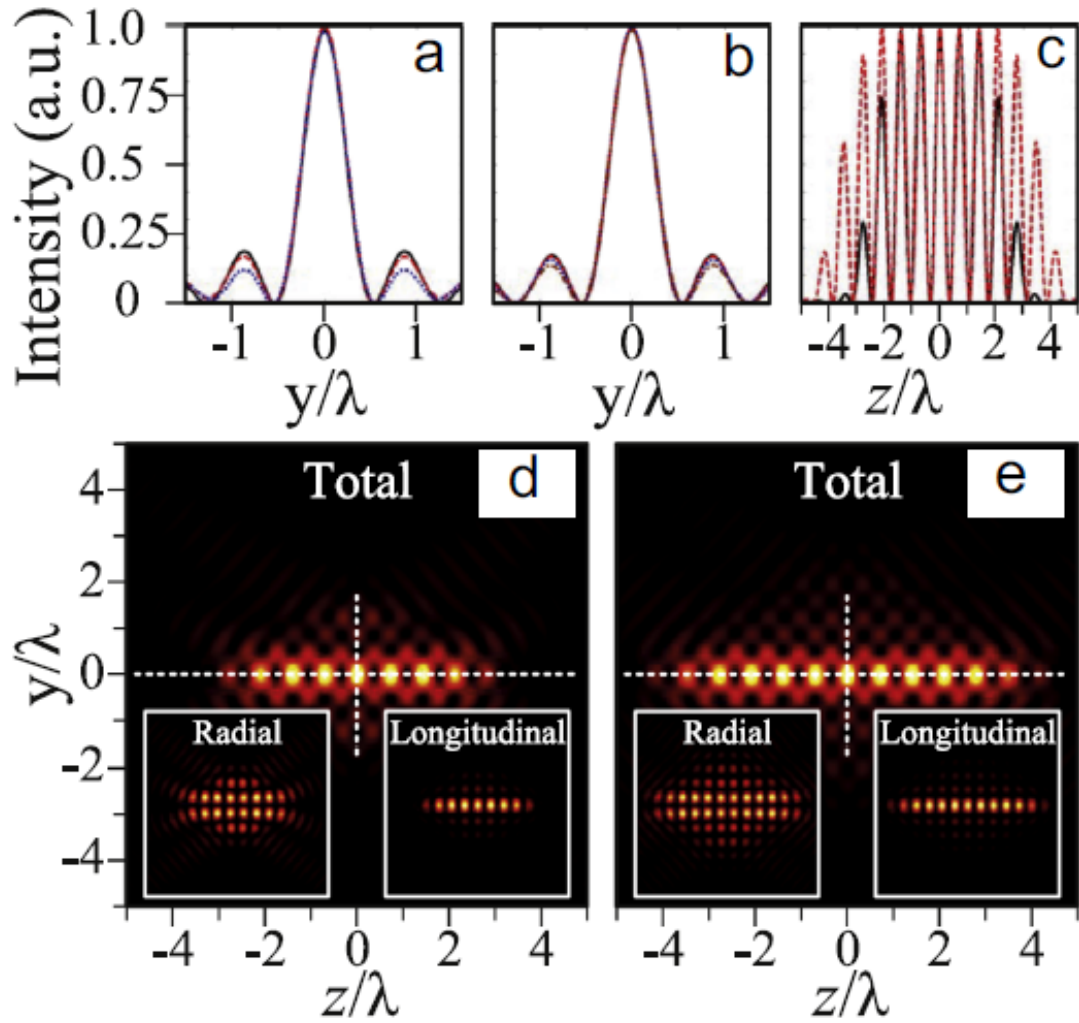
Figure 23 Intensity distribution in the focal region of the 4π focusing system illuminated by a radially polarized BG modulated by the complex amplitude filter with N = 2 and 3. For N = 2, $c_1 = c_2 = 1$, $m_1 = 0.75$ and $m_2 = 2.1$. For N = 3, $c_1 = 1$, $c_2 = 0.98$, $c_3 = 0.85$, $m_1 = 0.7$, $m_2 = 2.1$ and $m_3 = 3.5$. **(a)** Lateral intensity distribution on the focal plane (solid curve) and the plane where the peaks locate (dashed and dotted curves) for N = 2. **(b)** Lateral intensity distribution on the focal plane (solid curve) and on the plane where the peaks are located (dashed, dotted and dot-dashed curves) for N = 3. **(c)** Solid and dashed curves represent the axial intensity along the horizontal dashed lines in **(d)** and **(e)**. **(d)** Total intensity distribution in the *y-z* plane for N = 2. The vertical and horizontal dashed lines represent the *y* and *z* axes. **(e)** Total intensity distribution in the *y-z* plane for N = 3. The vertical and horizontal dashed lines represent the *y* and *z* axes. Insets in **(d)** and **(e)**: intensity distribution of the radially and longitudinally polarized components.

54

Experimentally, the 4π focusing system requires the two opposite-position lenses that are coaxial and confocal. The influence of the deviation of the lens optical axes and the shift of the foci on the focusing performance is investigated. Let us first consider the optical axes mismatching case first. For simplicity, it is assumed that the optical axes of the referred lenses are parallel, and their foci are in the same transverse plane. d_r is defined as the distance between the two off-axial optical axes. In order to describe the focusing performance clearly, the point located at $\frac{d_r}{2}$ is chosen as the origin of a new coordinate. The focusing spot located at the origin is explored. For a single lens, the focusing field is composed of radial and longitudinal components. The maximum of the longitudinally polarized component is on the optical axis of the lens, while the radially polarized component on the cross section is a doughnut distribution around the optical axis [122], [136]. The interference effect due to the two longitudinally polarized components will decrease with the increase of d_r. However, the intensity of the interference pattern of the two radial components will fluctuate for increasing d_r because of the doughnut distribution [136]. As displayed in Figure 24(a), the total field intensity at the origin will decrease and then increase with the increase of d_r, and ultimately approaches zero for sufficiently large d_r. Due to the lateral deviation of the optical axes, the lateral size of the focusing spots on the optical chain increases with increasing d_r as shown in Figure 24(c). The intensity of the optical chain gradually diminishes for sufficiently large d_r. Only two separate bright focusing zones appear along the dashed lines in Figure 24(e) and (f).
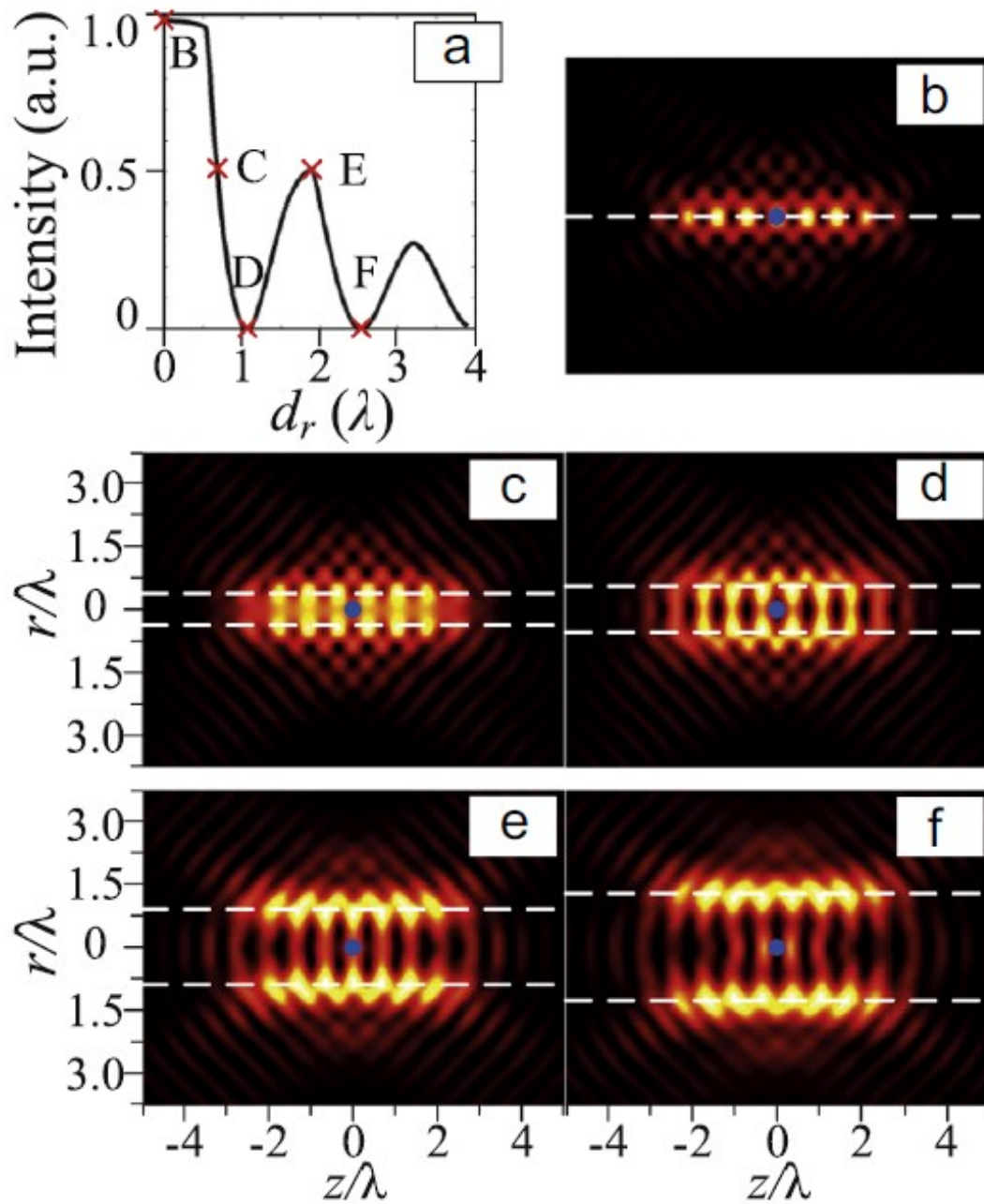
Figure 24 Influence of the off-axis distance on the focusing performance. **(a)** Intensity of the origin (marked by blue dots) for different off-axis distance d_r. **(b)-(f)** represent the intensity distribution on the r-z plane for d_r = 0, 0.68λ, 1.07λ, 1.89λ and 2.54λ, respectively. Intensity at the origin in **(b)-(f)** is shown in **(a)** as labeled by cross signs located at B, C, D, E and F. Dashed lines in **(b)-(e)** are the optical axes of lens in the 4π focusing system.

Another common alignment error in a 4π focusing system is foci shifting in the optical axis direction. In this case, the optical axes of the two lenses are overlapped but shifted in the optical axis direction. d_z is defined as the distance between the two foci as shown in Figure 25(a)-(d). Apparently, the effective interference zone is reduced when d_z increases. The number of focusing spots on the optical chain will cut down at the same time. Eventually, the interference effect can be neglected when d_z is larger than DOF of each polarized component and no optical chain will be obtained. If there is no complex amplitude filter, the DOF of the focusing field generated by the left or right lens is approximately 1.45λ.
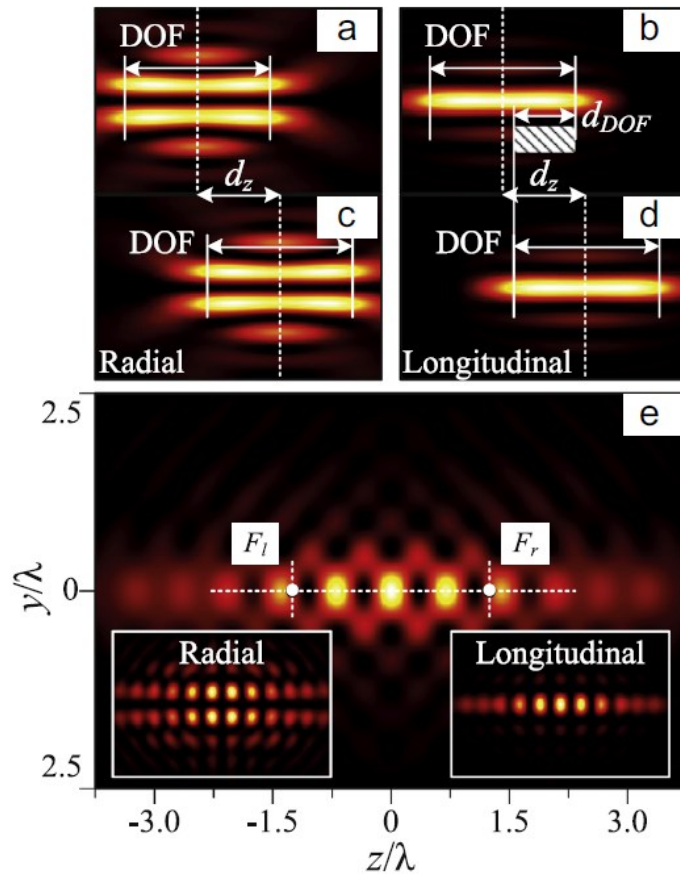
Figure 25 Schematic of the 4π focusing system with their foci located at different positions. **(a)** and **(b)** Intensity distribution of radially and longitudinally polarized component generated by the left lens in Figure 20, while **(c)** and **(d)** represent the intensity distribution of that generated by the right lens. Position of the focus is marked by dotted lines in **(a)** - **(d)**. Shadow region indicates the overlapped DOF. d_{DOF} is the overlapped range. **(e)** Total intensity distribution for N = 2 and $d_z = 2.5\lambda$. Insets in **(e)** are the interference intensity distributions of radially and longitudinally polarized components.

Therefore, the interference intensity can be ignored when d_z is larger than 1.45λ. When the complex amplitude filter is adopted, DOF of the focusing system is elongated. Large DOF will assure the generation of the optical chain even for a relatively significant foci shifting. This result is very important in experimental realization. For example, there are five focusing spots in Figure 23(d) when d_z is zero, while three focusing spots still exist in Figure 25(e) for $d_z = 2.5\lambda$. Meanwhile, the FWHM and DOF of each focusing spot in the effective interference zone remain the same as that with $d_z = 0$. Therefore, a 4π focusing system with the proposed complex amplitude filter is robust for axial focus shifting.

In this section, a scheme based on a 4π high NA focusing system and a complex amplitude filter is proposed to obtain an optical chain for a polarized BG incident beam. The optical chain is highly longitudinally polarized with a high axial resolution and a small spot volume. It is highly longitudinally polarized since the radially polarized component is destructive interference at the focusing spots. The FWHM is approximately half the wavelength. The DOF of the focusing spots on the optical chain is significantly reduced and is only one-fourth that of a single lens with the same parameters. The spot volume is smaller than $0.41\lambda^3$. A long optical chain with more focusing spots can be easily achieved by increasing N. The off-axis and foci shifting are also investigated. The results indicate that the referred scheme is robust for the foci shifting. It is, therefore, believed that the proposed scheme can be used in various applications such as confocal microscopy, nanoparticle optical trapping and manipulating.

3.3.2 Generation of hollow beam with radially polarized vortex beam and complex amplitude filter

Recently, focusing beams with different polarization have attracted tremendous attention due to vast potential in the field of optical measurements, optical recording, and optical trapping [116], [120] - [122], [140], [150], [156]. In 2003, a tight focal spot was first achieved using a radially polarized incident beam and an annular aperture [140]. Since then, various amplitude and phase filtering methods have been proposed [122], [129] - [131], [158] and experimentally validated to obtain a sharper focal spot [120]. A super-

resolution focal spot was achieved and has been used in optical disk writing with high intensity [120]. In 2008, a longitudinally polarized optical needle with high lateral resolution was first proposed, based on a binary optical element for BG with radial polarization [122]. A global search optimization algorithm was used to obtain an optimal DOF during the design of the elements used for phase modulation [122], [130]. Meanwhile, other focusing patterns, such as a doughnut beam and the special polarized beam, were also investigated, based on filtering technology [150], [159] - [162]. For example, the uniform transversally polarized light tunnel was achieved for an azimuthally polarized beam [159].

The hollow beams, or the so-called light tunnels, have potential application in nanoparticle trapping and are widely investigated [150], [163] - [169]. An example is an ultra-long optical tube generated by a discrete complex amplitude filter derived from the magnetic dipole array [163]. For a radially polarized BG, the axial intensity is not zero [122], [129], [162]. However, the null axial intensity is obtained by introducing a high-order vortex phase plate for different polarized beams according to [160]. The research result indicates that the focusing field is changed by the vortex phase plate [170]. For example, transversally polarized optical needles were achieved by the first-order vortex phase and a binary phase plate for an azimuthally polarized incident beam [159]. These studies have demonstrated that the vortex phase is of great importance in realizing novel focusing patterns [159], [160], [170] - [172].

In this section, a second-order vortex phase plate is introduced to implement a hollow beam for a radially polarized BG incident beam. When the second-order vortex phase plate is introduced, a null axial intensity appears and provides the opportunity to obtain a hollow beam. Furthermore, one can acquire the focusing field with long DOF by decreasing the NA of the focusing system. However, the lateral size of a hollow beam increases as the NA decreases. Therefore, a complex amplitude filter is employed to achieve a hollow beam with both small lateral size and large DOF in the proposed high NA focusing system for a radially polarized incident beam.

In a high NA focusing system, the electric field near the focus spot ($z = 0$) in a vacuum is described by Richards-Wolf's integral theory [113] - [116]. For the polarized incident beam with a second order vortex phase, the focusing field is written as follows [8], [136]:

$$E(r, \varphi, z) =$$
$$-iA \int_0^\alpha \int_0^{2\pi} l_0(\theta)V(\phi)\sqrt{cos\theta}sin\theta e^{ik(zcos\theta+rsin\theta\,cos(\phi-\varphi))}P(\theta,\phi)d\theta d\phi \quad (3.15)$$

where (r, φ, z) are the cylindrical coordinates of the focal region, the focal point is located at $z = 0$, θ and ϕ are the spherical angular coordinates of the output pupil of the focusing system, respectively, A is a constant, $l_0(\theta)$ is the amplitude distribution of the incident beam governed by the BG function [122], $V(\phi) = e^{i2\phi}$ is the second-order vortex phase, which can be realized by a phase plate, $\alpha = arcsin\left(\frac{NA}{n}\right)$, where n is the refractive index of the surrounding media of the focusing system, k and $P(\theta, \phi)$ are the wavenumber and the polarization matrix, respectively, and $P(\theta, \phi)$ is given as follows for a radially polarized beam [160], [163], [173]:

$$P(\theta, \phi) = \begin{bmatrix} cos\phi cos\theta \\ sin\phi cos\theta \\ -sin\theta \end{bmatrix} \quad (3.16)$$

The elements in the polarization matrix $P(\theta, \phi)$ for a radially polarized beam represent the x, y, and z components of the focusing field. Integration over ϕ in Equation (3.15) can be expressed by the Bessel function [160]:

$$\int_0^{2\pi} V(\phi)e^{ikrsin\theta\,cos(\phi-\varphi)} \begin{bmatrix} cos\phi cos\theta \\ sin\phi cos\theta \\ -sin\theta \end{bmatrix} d\phi$$
$$= -\frac{e^{i2\varphi}}{2} \begin{bmatrix} i(e^{i\varphi}J_3(t) - e^{-i\varphi}J_1(t))cos\theta \\ (e^{i\varphi}J_3(t) + e^{-i\varphi}J_1(t))cos\theta \\ -2J_2(t)sin\theta \end{bmatrix} \quad (3.17)$$

where $t = krsin\theta$ and $J_m(\cdot)$ is the m-order Bessel function. In Equation (3.17), $J_m(\cdot)$ (m = 1, 2, and 3) is zero for $t = 0$. The corresponding x-, y-, and z- polarized components are

null intensity on the optical axis. Therefore, the focused field exhibits the characteristic of a hollow beam. As previously discussed, the long DOF and small lateral size cannot be achieved simultaneously without using a filter. Therefore, the complex amplitude filter, based on the cosine function, is employed and validated in producing an optical needle with high lateral resolution for a radially polarized incident beam [131], [150]. The complex amplitude filter can be expressed as follows:

$$F_N(\theta) = \sum_{p=1}^{N} c_p \cos[km_p(2p-1)\cos\theta] \qquad (3.18)$$

where c_p is an amplitude adjustment parameter, m_p is displacement distance along the optical axis (z-axis), N controls the number of the cosine functions adopted in the filter, and k is the wavenumber of the incident beam. Considering that Equation (3.18) describes the transmission amplitude, it should be normalized by the maximal absolute value of $F_N(\theta)$. Once $F_N(\theta)$ is introduced, $l_0(\theta)$ can be replaced by $l_0(\theta)F_N(\theta)$.

Combining Equations (3.15), (3.17), and (3.18), the z-polarized component of the focused field can be expressed as follows:

$$E(r,\varphi,z) =$$
$$-i\frac{Ac_1}{2}\int_0^\alpha l_0(\theta)\sqrt{\cos\theta}\sin^2\theta e^{i2\phi}J_2(k\rho\sin\theta)[e^{ik(z+m_1)\cos\theta} + e^{ik(z-m_1)\cos\theta}]d\theta \qquad (3.19)$$

Equation (3.19) can be rearranged as:

$$E_z(r,\varphi,z) = E_z(r,\varphi,z+m_1) + E_z(r,\varphi,z-m_1) \qquad (3.20)$$

Obviously, the z-polarized component of the focusing field is the sum of the two individual focusing fields with the focal spots located at $z = \pm m_1$, respectively. If m_1 is equal to zero, then Equation (3.20) becomes Equation (3.17). Similar expressions for x- and y-components can be obtained and the total field intensity is given by $|E_x(r,\varphi,z)|^2 + |E_y(r,\varphi,z)|^2 + |E_z(r,\varphi,z)|^2$. Clearly, multifocus spots appear and the distance between

61

the focal spots is $2m_1$. The axial intensity distribution is determined by m_1. Therefore, DOF with uniform intensity can be obtained by adjusting the parameter m_1. Apparently, long DOF can be obtained as well by increasing N, which means more cosine functions should be employed.

For a radially polarized BG without using additional phase plate, previous research results have demonstrated that the intensity along the optical axis is not zero [116], [122], [130]. However, the null intensity occurs at the optical axis for the BG with a second-order vortex phase $e^{i2\phi}$. Generally, the BG incident beam $l_0(\theta)$ is expressed as follows [116], [122]:

$$l(\theta) = \exp\left[-\beta^2 \left(\frac{sin\theta}{sin\alpha}\right)^2\right] J_1\left(2\gamma \frac{sin\theta}{sin\alpha}\right) \tag{3.21}$$

where $J_1(\cdot)$ is the first-order Bessel function. β and γ are beam parameters that are taken as unity in this research, assuming n and NA are 1 and 0.95, respectively. $\alpha = \arcsin\left(\frac{NA}{n}\right)$ is approximately equal to 1.25. The intensity distributions of the total field, x-, y-, and z-components near the focal point are shown in Figure 26. The bright (dark) areas indicate the regions with high (low) electric intensity. Numerical results indicate that the intensity is zero on the z-axis and the null center appears for x-, y-, and z- polarized components, which confirms that the hollow beam is obtained for a radially polarized BG with a second-order vortex phase plate. The total electric intensity on the x-z plane is symmetric with respect to the z-axis [see Equation (3.15)]. The outer (inner) diameter D_o (D_i) of the hollow beam is defined as the outer (inner) full width at half-maximum (FWHM) at the focal plane [3]. D_o and D_i are marked by lines AD and BC, respectively, as is shown in Figure 27(a). Therefore, the thickness of the hollow beam can be defined as $0.5(D_o - D_i)$. The region along the z-axis with an intensity higher than 80% of the maximum intensity is regarded as the DOF of the focusing field, which is highlighted by a dashed line in Figure 27(b). It can be clearly seen that the DOF is 0.96λ for the focused beam with a second-order vortex phase. The inner diameter D_i of the total field at the focal plane is 0.60λ, and the outer diameter D_o is 1.71λ. Therefore, the corresponding thickness of the obtained hollow beam is approximately 0.56λ. D_i is determined by the order of vortex and NA of the focusing

system. Thus, it increases with the increase of the order of the vortex phase for a fixed NA. The second order is the smallest order that one can obtain a hollow beam for a radially polarized beam when NA = 0.95 [160]. The longitudinally polarized component is axial symmetric about the z-axis. However, the intensity distribution of the x- and y-polarized components is twisted on the transversal plane.
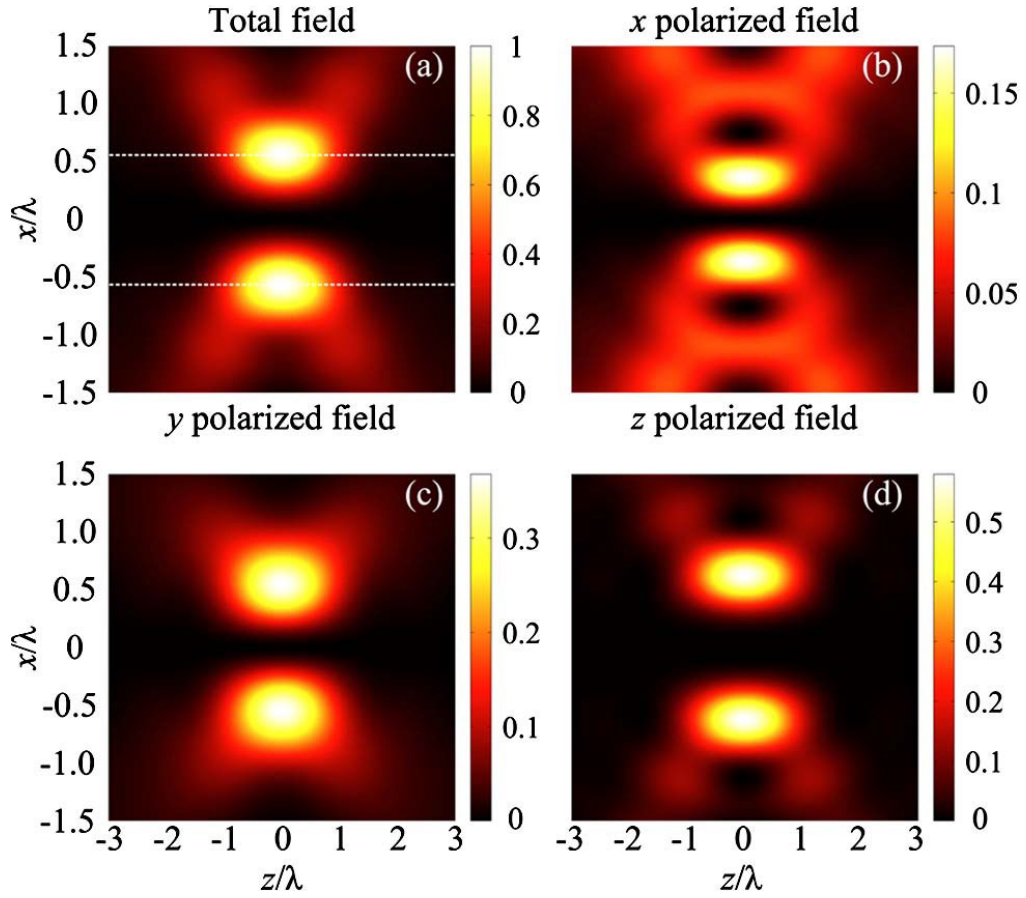
Figure 26 Focusing field intensity distribution at the x-z plane for the radially polarized BG incident beam with a second-order vortex phase in the focusing system with NA = 0.95. **(a)** Total electric energy intensity near the focal point. The dotted lines, which mark the position of the maximum intensity, are parallel to the z axis. **(b)** - **(d)** are the intensity distributions of x-, y-, and z-polarized components, respectively.

To elongate the DOF of a hollow beam for a radially polarized incident beam with a second-order vortex phase, a complex amplitude filter based on the cosine function is introduced, as described in Equation (3.18). To verify the validity of the proposed complex amplitude filter in designing a hollow beam with a long DOF, the simplest filter with N =

1 is investigated. Generally, the values of c_p and m_p are obtained using an optimization algorithm. For the simplest filter, the parameter c_1 can be taken as unity and the amplitude filter $F_1(\theta)$ is rewritten as $\cos(km_1\cos\theta)$, where $k = \frac{2\pi}{\lambda}$ is the wave number. Through an empirically direct search procedure, the value of m_1 can be determined. According to the calculation, $m_1 = 0.5$ is taken to generate the hollow beam with a long DOF. In this case, the expression for the designed complex amplitude filter is written as $F_1(\theta) = \cos(0.5kcos\theta)$. For $m_1 = 0.5$, the distance between the two peaks is 1.0λ. The complex amplitude profile of the filter $F_1(\theta)$ is shown in Figure 28(a). The corresponding focusing characteristics of the radially polarized incident beam with a second-order vortex phase are displayed in Figure 28(b) - (d). In Figure 28(b), the bright (dark) areas represent the regions with high (low) electric intensity. One can see that the high intensity occurs along the z-axis at a position where the dashed lines exist and DOF is approximately equal to 2.28λ, which is nearly 2.4 times that without using a filter (0.96λ). The distance between the dashed lines is approximately 1.33λ. Apparently, one can conclude that long DOF can be achieved using the designed complex amplitude filter by comparing Figure 28(c) with Figure 27(b). In Figure 28(c), uniform intensity distribution is achieved in the region of the DOF. The lateral intensity distributions of the focused hollow beam on the planes $z = 0$ and $z = 1.14\lambda$ are shown in Figure 28(d). In Figure 28(d), the outer (inner) diameter of the hollow beam are marked by lines AD (BC). D_o and D_i are 2.23λ and 0.63λ, respectively. D_o and D_i of the designed hollow beam are approximately equal to 130% and 113% that of the focusing beam without using a filter, respectively. The corresponding thickness of the hollow beam is approximately 0.80λ. The DOF will increase for the radially polarized BG incident beam by employing a second-order vortex phase and a complex amplitude filter, although the lateral size may slightly increase when compared with the case without a filter. The dot-dashed curve in Figure 28(d) represents the transverse intensity distribution on the plane $z = 1.14\lambda$, which is the end position of the DOF. The transverse intensity distributions at $z = 0$ and $z = 1.14\lambda$ are nearly the same. The insets in Figure 28(d) are the two-dimensional transverse intensity distributions on the $z = 0$ and $z = 1.14\lambda$ planes. On the $z = 0$ plane, the null center appears and is surrounded by a ring-like intensity distribution.
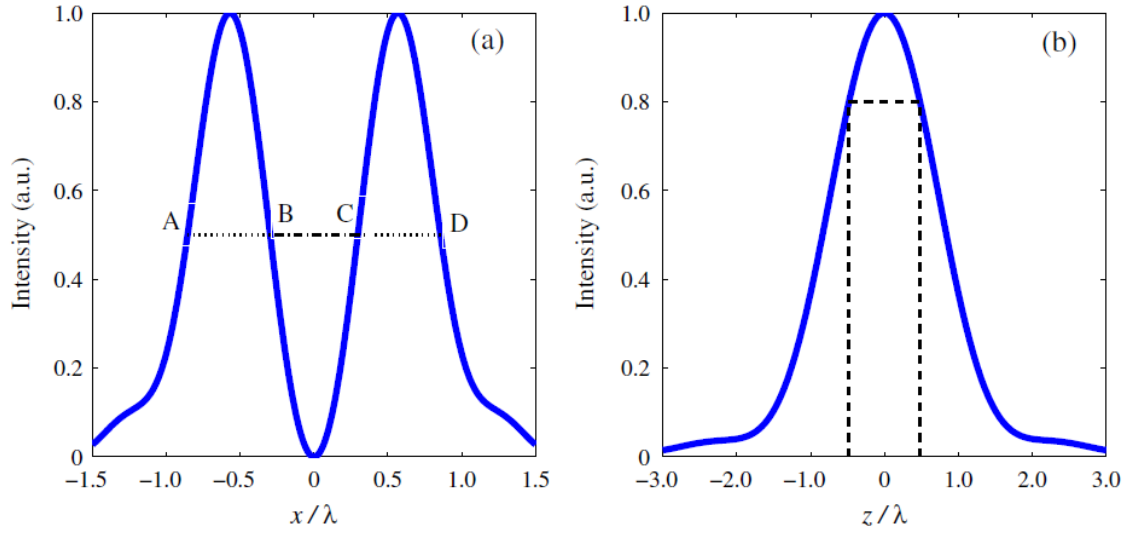
Figure 27 Focusing field intensity at the *x-z* plane for a radially polarized BG with a second-order vortex phase in the focusing system with NA = 0.95. **(a)** Intensity distribution at the focal plane *z* = 0. **(b)** Intensity distribution along the dotted lines in Figure 26**(a)**. DOF of the focusing field is labeled by the dashed line.

The numerical results indicate that total intensity does not depend on φ at the transversal plane. However, the intensity patterns of the *x*- and *y*-polarized components in front of and behind the focal point are opposite, which implies that the generated field is twisted. There are two intensity peaks that are symmetric about the *z*-axis for the *x*- and *y*-polarized components. To describe the twisted *x*- and *y*-polarized components, the positions of the intensity peaks for the two components are shown in Figure 29 for different *z*.
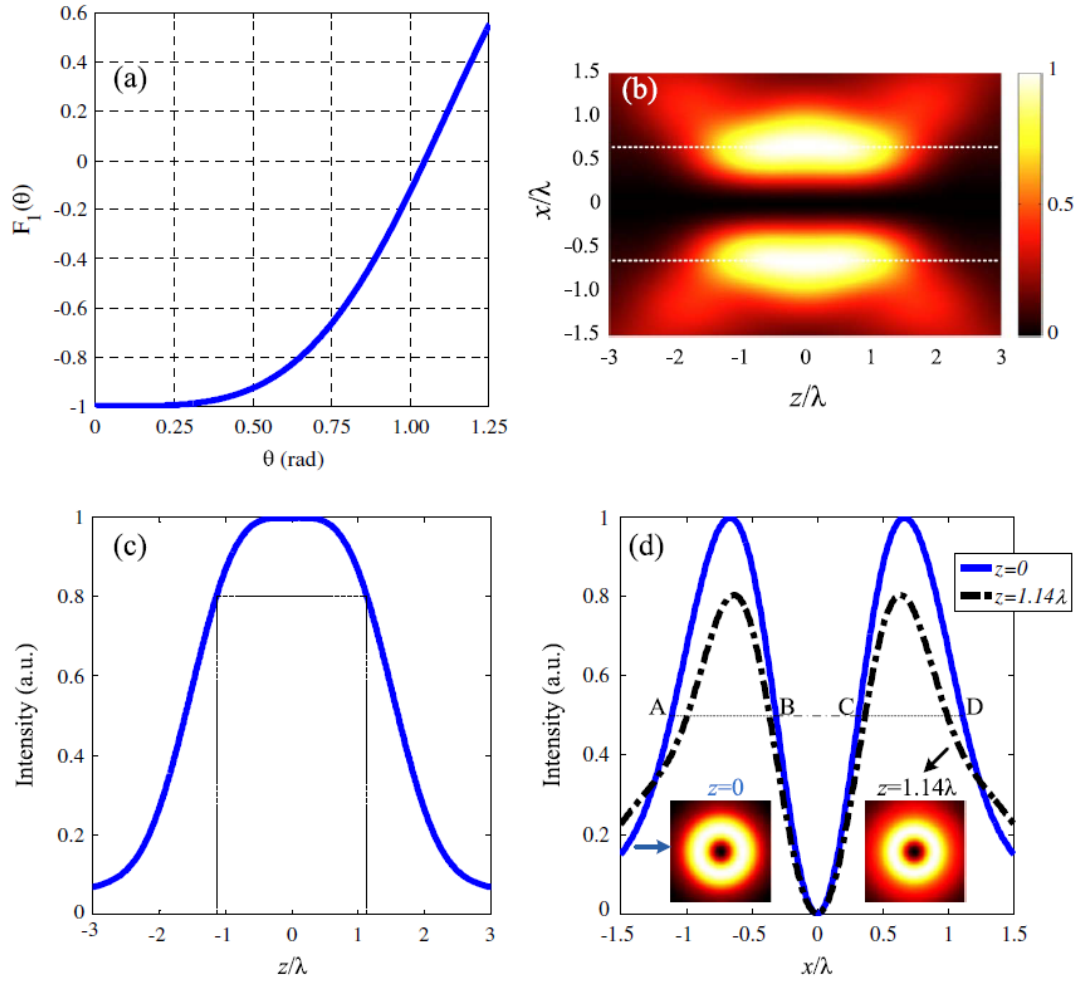
Figure 28 **(a)** Amplitude transmittance of the complex amplitude filter for N = 1, $c_1 = 1$, and $m_1 = 0.5$, and **(b)** the corresponding intensity distribution in the y-z plane, where white areas represent high field intensity. **(c)** Longitudinal intensity profile along dashed lines, where maximum of intensity is located in **(b)**. DOF is approximately 2.28λ, and the range of DOF is marked by the dashed lines. **(d)** Lateral intensity distribution at different longitudinal positions of z. AD and BC mark outer and inner diameters D_o and D_i, respectively.

In Figure 29, the two black solid curves represent position information for the intensity peaks of the x-polarized component at different z. It is seen that the black solid curves are symmetric about the origin and twisted along the z-axis. The same characteristics exist for the y-polarized component. Numerical results also indicate that lines connecting the two intensity peaks of the x- or y-polarized components are perpendicular. To further demonstrate the observation, the intensity distributions of the x-, y-, and z-polarized components in front of, on, and behind the focus are shown in Figure 30. Their intensity

66

peaks are marked by ×. By comparing Figure 30(a1), (a2), (c1), and (c2), one can see that the intensity distributions of the x- and y-polarized components are twisted. The intensity peaks are in the first and the third quadrants for $z = -1.14\lambda$, whereas they are in the second and fourth quadrants for $z = 1.14\lambda$. The intensity distribution on the focal plane does not twist for the x- and y-polarized components. Meanwhile, the field intensity distribution does not twist along the optical axis for the z-polarized component. In addition, the lines connecting the two intensity peaks in (a1) [or (c1)] are perpendicular to those in (a2) [or (c2)], according to Figure 30(a1) and (a2) [or (c1) and (c2)]. On the focal plane, the intensity peaks are at the y-axis for the x-polarized component, whereas they are located at the x-axis for the y- polarized component. In a Cartesian coordinate system, the intensity distributions of the x- and y-polarized components twist at the defocus plane. In the cylindrical coordinate system, transverse polarized components are radial and azimuthal. The radial E_r and azimuthal E_φ components can be expressed by E_x and E_y, i.e., $E_r = E_x cos\varphi + E_y sin\varphi$ and $E_\varphi = E_y cos\varphi - E_x sin\varphi$, where $r = \sqrt{x^2 + y^2}$ [116]. If vortex phase is not applied in the radially polarized incident beam, then the azimuthal component E_φ is zero everywhere in image space. In the cylindrical coordinate system, the intensity distributions of the radial and azimuthal components are always cylindrically symmetric whenever near or out of focus, as shown in the insets in Figure 31. The intensity distributions of the components at the focus plane are given as comparisons with that at the defocus plane. The intensity distributions of the polarized component at the plane $z = -1.14\lambda$ and $z = 1.14\lambda$ are identical. However, the phase of the polarized components shows twisting and rotating on different defocus planes and a second-order vortex. For example, for the azimuthally polarized component, the phase jumps from $-\pi$ to π along the radius. However, the phase jump appears as a curve at the defocus plane. For the radially polarized components, similar results appear. Additionally, phase distributions at different defocus planes are determined by ρ and φ. Phase singularity occurs on the optical axis for null central intensity.
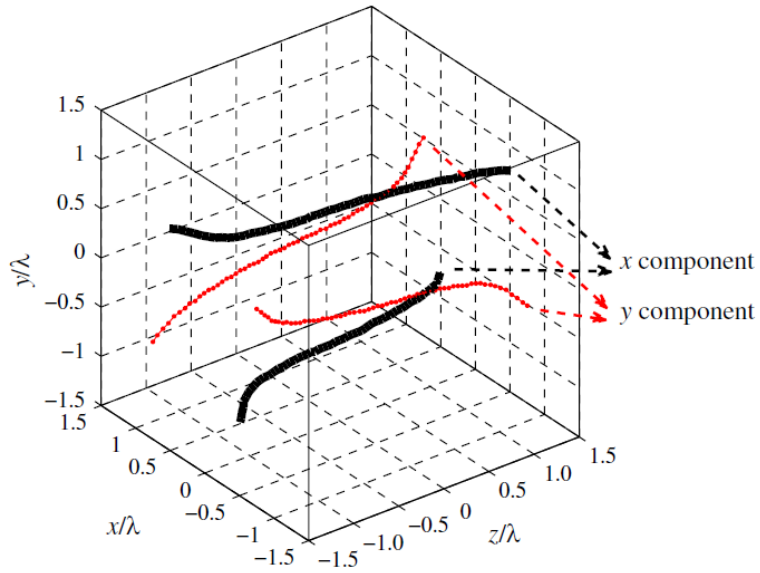
Figure 29 Positions of the maximum intensity of the *x*- and *y*-polarized components on different transversal planes along the z-axis. Black and red solid curves represent the *x*- and *y*-polarized components, respectively.
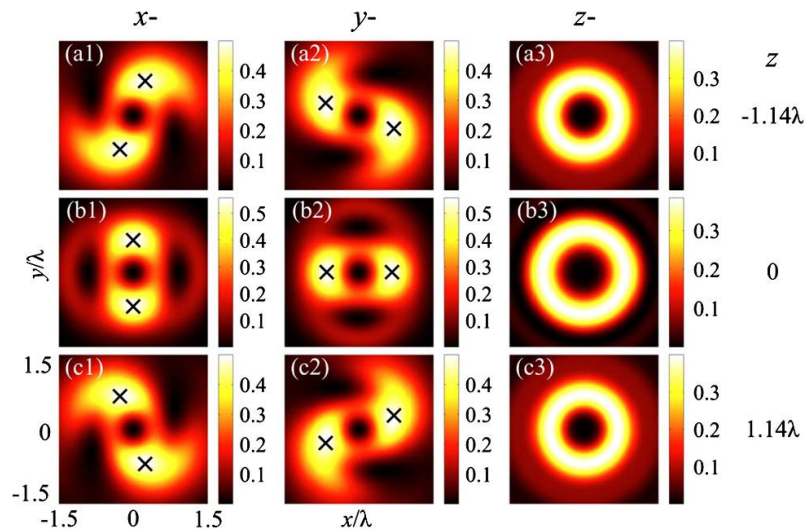
Figure 30 Intensity distributions of the *x*-, *y*-, and *z*-polarized components at different transverse planes along the optical axis. **(a1)** - **(a3)** Intensity distributions at transverse plane $z = -1.14\lambda$, **(b1)** - **(b3)** at $z = 0$, and **(c1)** - **(c3)** at $z = 1.14\lambda$, respectively. Intensity distributions **(a1)**, **(b1)**, and **(c1)** for the *x*-polarized component; **(a2)**, **(b2)**, and **(c2)** for the *y*- polarized component; and **(a3)**, **(b3)**, and **(c3)** for the *z*- polarized component. Positions of maximum intensity are marked by × for the *x*- and *y*-polarized components. There are two equal intensity peaks in the *x*- and *y*-polarized components. Field intensity of the *z*-polarized component is symmetrical with respect to the *z*-axis.

Considering the principle of the filter, the length of DOF will be determined by the parameter N. For a long DOF, more cosine functions are involved. This means that N increases. Since c_1 is assumed to be unity, the value of 2N − 1 parameters, which are c_2; c_3; … ; c_N and m_1; m_2; … ; m_N, should be determined for producing a hollow beam with a long DOF. c_i is used to control the relative amplitude of each cosine function. The values of those parameters are determined by optimization algorithms. However, the achievement of a long DOF is time-consuming when N is greater than 1. For example, if N is 20, then 39 parameters (c_2, …, c_{20}, m_1, …, m_{20}) need to be determined. To demonstrate the dependence of the DOF on N, N = 2 in Equation (3.18) was considered. In this case, there are only three parameters to determine: c_2, m_1, and m_2. Numerical calculations indicate that the DOF is approximately 3.4λ while the values of c_2, m_1, and m_2 are 0.65, 0.80, and 2.3, respectively. The DOF is approximately 3.5 times longer than that of the focusing field without using an amplitude filter. At the focal plane, the outer diameter D_o and the inner diameter D_i are approximately 1.82λ and 0.62λ, respectively. They are approximately 106% and 110% that of the focusing field without any filter.
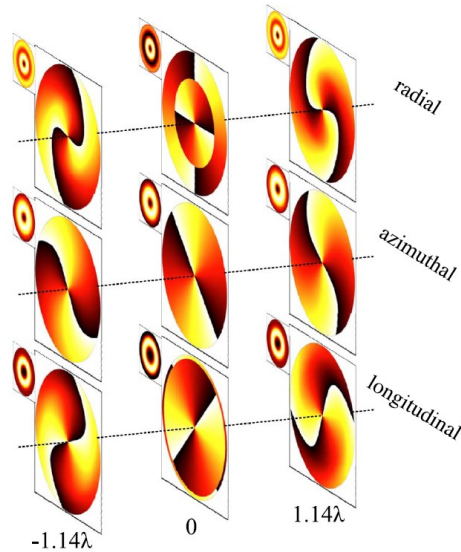
Figure 31 Phase distributions of the radially, azimuthally, and longitudinally polarized components at different transverse planes along the optical axis. $\rho_{max} = 1.5\lambda$. White and dark regions represent high and small phase (or intensity in the insets). Insets represent the intensity distributions of the corresponding polarized component. Total fields are the sum of the intensity of the radial, azimuthal, and longitudinal components.

A long DOF hollow beam has been achieved by focusing a radially polarized BG with a second-order vortex phase and a complex amplitude filter. The scheme was analyzed using Richards-Wolf's theory [113] - [116]. The null center was realized by introducing the second-order vortex phase. The DOF was elongated by an amplitude filter based on cosine functions. Numerical results indicate that the intensity distribution of the obtained hollow beam keeps almost invariant along the optical axis over a long distance (approximately 3.4λ, which is 3.5 times of that of the focusing field without a filter) for $N = 2$. The inner and the outer diameters of the hollow beam are slightly changed. The intensity twist of the *x*- and *y*-polarized components was observed after introducing the second-order vortex phase. Such a beam may find applications in the field of optical trapping and guiding.

3.3.3 Focusing performance of radially polarized BG with fractional vortex phase modulation

In section 3.3.2, a vortex phase plate is introduced to create a hollow focusing field. The vortex phase filter can be described by $V(\phi) = e^{\pm im\phi}$ where $m = 0$, 1, 2, 3 … is the topological charge of vortex phase. Most of the research focuses on integer topological charge. For a focusing system with a high NA, the focusing field intensity distribution modulated by vortex phase filters with fractional topological charge has not been well studied.

In this section, the vortex phase plate with fractional topological charge, which can be described by $V(\phi) = e^{\pm i\kappa\phi}$ ($\kappa > 0$), is introduced to a high NA focusing system with a radially polarized BG $l(\theta)$ as the incident light. Therefore, the incident vortex beam $e_i(\theta, \phi)$ is given by the following equation:

$$e_i(\theta, \phi) = V(\phi)l(\theta) \tag{3.22}$$
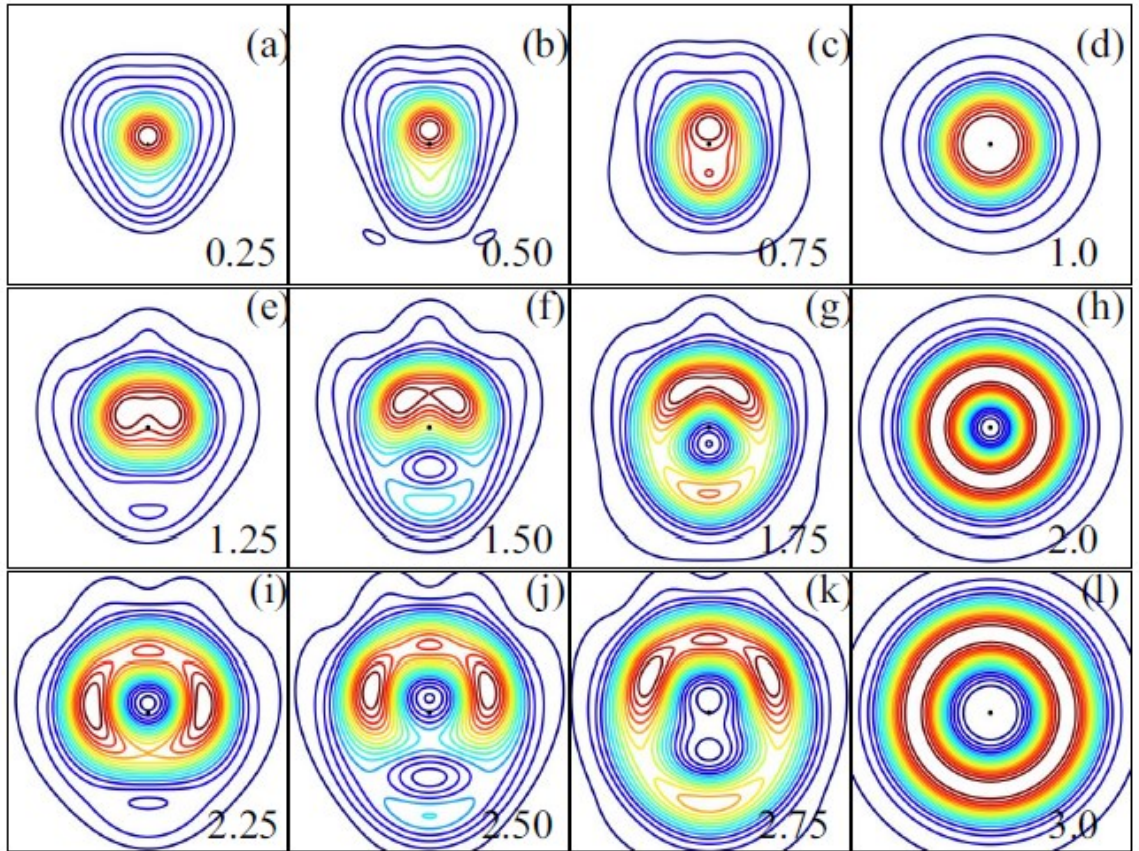
Figure 32 The focusing field intensity distribution contour plots ($3\lambda \times 3\lambda$) at the focal plane when different fractional vortex phase filters are used. NA=0.95. κ is shown at the right bottom corner of each plot. **(d)**, **(h)** and **(l)** show the regular integer orders. The black dots in each plot represent the coordinate origins.

Figure 32 shows the total focusing field intensity distribution on the focal plane when κ varies from 0 to 3 with an interval of 0.05. For integer orders, $\kappa = 1, 2, 3$, the focusing field intensity distribution is symmetrical with respect to the optical axis as shown in Figure 32 (d), (h), and (l). The field intensity on the optical axis decreases with the increase of the order.

When the vortex order κ is non-integer, the focusing field intensity distribution is symmetrical with respect to the y-axis. For example, the contour map curves are not concentric circles anymore when $\kappa = 0.25$ as shown in Figure 32(a). The only intensity peak deviates from the center and appears on the positive y-axis side. Notice that a

secondary peak starts showing up on the negative y-axis when $\kappa = 0.75$. Apparently, there is a power redistribution on the focal plane in the process as κ increases from 0 to 1. Compare Figure 33(a1) and (e1), this power redistribution causes a focusing spot lateral size increase at the focal plane. In the process of κ changing from 1 to 2, there are more intensity peaks showing up on the focal plane. The power redistribution causes the focusing field on the focal plane to become a ring shaped distribution. Figure 32(h) shows a null center exists in the focusing field at the focal plane. Further increasing the vortex order will increase the lateral size of the focusing field and the diameter of the null center.

For a radially polarized incident beam, the focusing field has three polarization components: the x-, and y- polarization components in the lateral plane and the z- polarization component in the longitudinal direction. Figure 33 shows the total, x-axis polarized component, y-axis polarized component, and z-axis polarized component intensity distributions when κ varies from 0 to 1 at a step of 0.25. When κ is an integer, the x-, y-, and z- polarization components are all symmetric with respect to the optical axis. When $\kappa = 0$, the z- polarization component is not zero on the optical axis, while the x-, and y- polarization components are not zero when $\kappa = 1$. Therefore, the total field intensity distribution is symmetric with respect to the optical axis, but its intensity is not zero on the optical axis. When $\kappa \geq 2$ and κ is an integer, a zero intensity can be created on the optical axis because the three polarization components are all zero on the optical axis. In this case, a hollow beam can be generated.

When κ is a fraction, the symmetry with respect to the x-axis disappears. The x-, and y- polarization components are not orthogonal to each other anymore. Compare Figure 33(a1) - (e1) (or (a2) - (e2), (a3) - (e3) and (a4) - (e4)), the intensity redistribution is clearly shown. The hollow focusing field is very important for many applications. For example, a hollow focused laser beam is introduced to deplete unwanted spontaneous emission in a STED microscope. A vortex focusing laser beam carries unique orbital angular momentum that can be used for nanoparticle trapping and transportation.
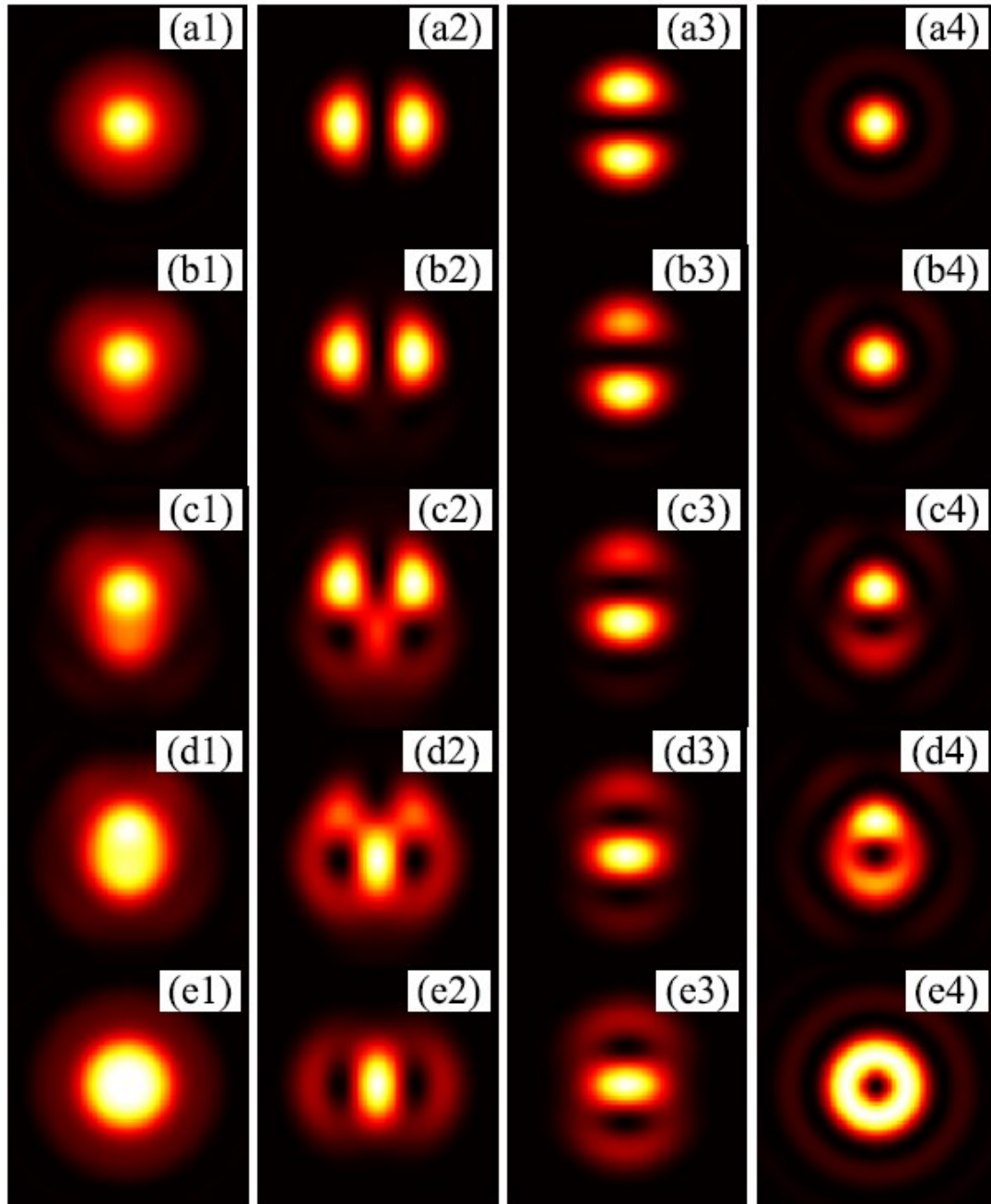
Figure 33 Focusing field intensity distribution at the focal plane when different fractional vortex phase filters are used. **(a1) - (a4)** $\kappa = 0$, **(b1) - (b4)** $\kappa = 0.25$, **(c1) - (c4)** $\kappa = 0.5$, **(d1) - (d4)** $\kappa = 0.75$, and **(e1) - (e4)** $\kappa = 1$ show the total, x-axis polarized component, y-axis polarized component, and z-axis polarized component intensity distributions, respectively.

3.4 GENERALIZED COMPLEX AMPLITUDE FILTER

In previous sections, cosine function based complex amplitude filters have been discussed. Unique focusing fields have been successfully demonstrated utilizing these filters in a high NA focusing system. In this section, the general form of complex amplitude filters and the fabrication of these filters will be discussed.

3.4.1 Sine function based complex amplitude filter

Cosine function based complex amplitude filters have been discussed in section 3.2. Sine function can also be used to construct complex amplitude filter for focusing field shaping. The sine function based complex amplitude filter can be mathematically expressed as:

$$F_N(\theta) = \sum_{p=1}^{N} \sin[km_p(2p - 1)\cos\theta] \tag{3.23}$$

Take N = 1 as an example, the filter can be written as:

$$F_1(\theta) = \sin(km_1\cos\theta) = \frac{1}{2i}\left[e^{ikm_1\cos\theta} - e^{-ikm_1\cos\theta}\right] \tag{3.24}$$

Therefore, the radial component of the focusing field can be obtained from Equation (2.21):

$$E_r(r,z)$$
$$= \frac{1}{2i}A \int_0^{\theta_{max}} P(\theta)\sin(2\theta) J_1(kr\sin\theta)l(\theta)[e^{ik(z+m_1)\cos\theta} - e^{ik(z-m_1)\cos\theta}]d\theta \tag{3.25}$$

Equation (3.25) can be rewritten in a simpler format:

$$E_r(r,z) = \frac{1}{2i}[E_r(r,z + m_1) - E_r(r,z - m_1)] \tag{3.26}$$

In comparison to Equation (3.10), the main difference is that the focusing field described by Equation (3.26) becomes the difference between the two split components. This could cause null intensity at the center because of the phase difference between the two split components. This type of filters is not ideal for applications that require a uniform focusing field. Figure 34 demonstrates the focusing performance of the sine function based complex amplitude filter with N = 1, $m_p = 0.7$. From Figure 34(b), we can see that there is a null intensity center between the two split spots. m_p needs to be finely adjusted in order to obtain a uniform focusing field. But the DOF will decrease. Compared to the focusing performance of cosine function based complex amplitude filter, it is much more difficult to optimize the sine function based complex amplitude filter to obtain a focusing field with a long DOF. However, extra tuning parameters can be introduced to the sine function based complex amplitude filter to compensate for the null intensity center so that a uniform long DOF focusing field can be achieved.
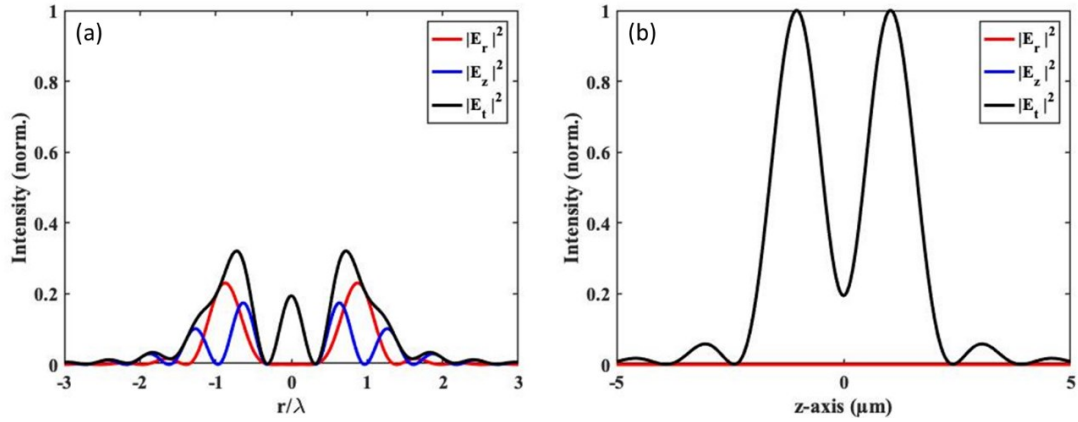
Figure 34 **(a)** Intensity distribution at the focal plane $z = 0$ along a radial axis and **(b)** intensity distribution along the optical axis for the BG with $\beta = 1$ and $\gamma = 1$. NA = 0.95. Red, blue and black curves represent the radial component, the longitudinal component and the total field, respectively. The sine function based complex amplitude filter with N = 1, and $m_1 = 0.7$ is applied in this case.

3.4.2 General form of complex amplitude filters

The cosine and sine function based complex amplitude filters can be written in general form as:

$$\sum_{n=1}^{N} \cos[(2n-1)Mkcos(\theta)] \tag{3.27A}$$

$$\sum_{n=1}^{N} \sin[(2n-1)Mkcos(\theta)] \tag{3.27B}$$

Assuming $x = \cos(\theta)$, Equation (3.27) can be rewritten as:

$$\sum_{n=1}^{N} \cos[(2n-1)Mkx] \tag{3.28A}$$

$$\sum_{n=1}^{N} \sin[(2n-1)Mkx] \tag{3.28B}$$

All the complex amplitude filters designed in previous sections are linear combinations of these two functions shown in Equation (3.28).

Simple trigonometry can be applied to further study the characteristics of these complex amplitude filters. In trigonometry mathematics, we have:

$$A \cdot \cos(Mkx) + B \cdot \sin(Mkx) = \sqrt{A^2 + B^2} \sin(Mkx + \varphi) \tag{3.29}$$

where $\varphi = \arcsin\left(\frac{A}{\sqrt{A^2+B^2}}\right)$. Equation 3.29 can be rearranged in the following form:

$$\sqrt{A^2 + B^2} \sin(Mkx + \varphi)$$
$$= \sqrt{A^2 + B^2} \sin\left[\left(M + \frac{\varphi}{kx}\right)kx\right] = \sqrt{A^2 + B^2} \sin[M'kx] \tag{3.30}$$

where $M' = M + \frac{\varphi}{kx}$. Comparing Equation (3.30) and Equation (3.28), it is easy to see that the complex amplitude filter constructed by the linear combination of the cosine and sine

functions is equivalent to a sine function based complex amplitude filter. However, the adjustment coefficients are different. In Equation (3.30), the horizontal adjustment parameter M' has a new term $\frac{\varphi}{kx}$. Because of the existence of this new term, the focusing field splits into multiple focal spots and distribute unevenly along the optical axis. The uneven distribution of the focal spots offers the opportunity to fine tune the amplitude and location of each spot to optimize the overall shape of the focusing field.

It has been demonstrated that the designed complex amplitude filters can be utilized to shape the focusing field and achieve various unique focusing fields for different application scenarios. The problem with the designed amplitude filter is that it will attenuate the optical field. Theoretically, the DOF can achieve infinite length by introducing more and more cosine functions to the complex amplitude filter. The attenuation effect of the complex amplitude limits the increase of DOF at a certain level. Another drawback with the designed complex amplitude filter is fabrication. Notice that the designed complex amplitude filter has a continuously varying profile as shown in Figure 16. In practice, it is very difficult to fabricate high precision filters with such a complicated profile. It is challenging to apply the complex amplitude filters in real applications due to these problems. To address these issues, binary optics can be designed based on the complex amplitude filters.

3.4.3 Implementation of complex amplitude filters using binary optics

As discussed in section 3.4.2, the generalized form of the complex amplitude filter can be expressed using Equation (3.28). $\cos(nMkx)$ and $\sin(nMkx)$ form an orthogonal basis when n is a natural number. According to the trigonometric Fourier series theory, a binary filter can be constructed in the following form:

$$BF = \sum_{n=1}^{+\infty} \frac{1}{2n-1} \sin[2\pi(2n-1)Mx] \qquad (3.31)$$

where $x = \cos(\theta)$. After normalization, the binary optics filter can be written as:

$$BF(\theta) = \frac{BF}{\max(BF)} \qquad (3.32)$$

To verify the performance this binary optics filter design method, $M = 0.9$ is chosen and $BF(\theta)$ can be calculated accordingly:

$$BF(\theta) = \begin{cases} 1, & \theta < 0.586 \\ -1, & 0.586 \leq \theta < 1.29 \\ 1, & \theta \geq 1.29 \end{cases} \qquad (3.33)$$

Equation (3.33) and Figure 35(a) illustrate the designed binary optics filter. From Figure 35(a), one can see that the amplitude transmittance profile has a binary shape. A binary optics filter can then be fabricated based on the parameters given in Equation (3.33). Figure 35(b) shows the focusing performance of this binary optics filter. A long DOF focusing field can be clearly observed and the intensity distribution along the optical axis has good uniformity. Compared to the result shown in Figure 15(b), the DOF achieved using this binary optics filter is almost the same as the focusing field obtained from using the cosine function based complex amplitude filter. This can be explained by the fact that only low frequency (small n in Equation (3.31)) components have a relatively big contribution to the filter function. In principle, binary optics filter designed using trigonometric Fourier series method can also achieve high focusing field shaping performance. Most importantly, it doesn't have the power attenuation problem and it is much easier to fabricate than the complex amplitude filter with a continuous varying profile.
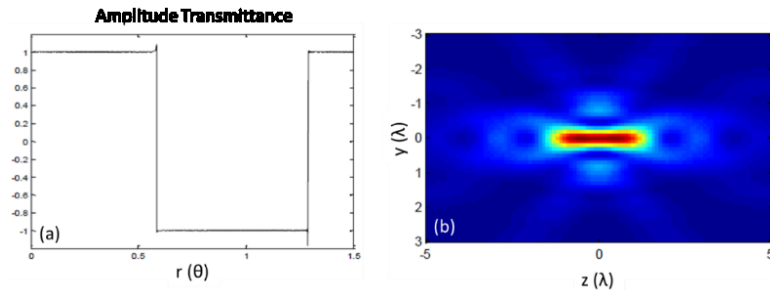
Figure 35 **(a)** Binary optics filter designed based on complex amplitude filters, and **(b)** focusing field shaping performance of the designed Binary optics filter

3.5 SUMMARY

In this chapter, a radially polarized doughnut Gaussian beam is studied first. The radially polarized doughnut Gaussian beam is introduced to a high numerical aperture focusing system to generate a sub-wavelength focal spot. The focusing characteristics of a radially polarized doughnut Gaussian beam by a high numerical aperture lens are theoretically investigated based on the Richards-Wolf diffraction integral theory [113] - [116]. Numerical results indicate that sub-wavelength focusing can be easily obtained for a radially polarized doughnut Gaussian incident beam. Therefore, the radially polarized doughnut Gaussian beam is of great importance in the super-resolution focusing field.

In order to achieve long depth of focus, a cosine function based complex amplitude filter is designed to increase the length of the depth of focus in a high NA focusing system. The cosine function based complex amplitude filter can split the focusing field into two or more components in the optical axis direction. In principle, the focusing field can be designed to achieve long DOF by optimizing the m_p parameter of the complex amplitude filter. Therefore, the focusing field can be engineered for various applications.

By taking advantage of the designed complex amplitude filters, hollow beams with a long focal depth are generated from a radially polarized BG with a second-order vortex phase filter. The null intensity on the optical axis is achieved by introducing the second-order vortex. The long focal depth is a result of the amplitude filtering based on cosine functions and Euler transformation. Numerical results indicate that the focal depth of a hollow beam is improved from 0.96λ to 2.28λ with a slight increase of the transverse size for the simplest amplitude filter design. The intensity distribution twist phenomenon of the *x*- and *y*-polarized components around the optical axis due to the introduction of the vortex phase is also discussed. It is believed that the proposed optical system can be used to achieve applications such as nanoparticle acceleration and optical trapping.

Also, a longitudinally polarized optical chain is generated in a 4π focusing system. The radially polarized Bessel-Gaussian incident beam is modulated by a complex amplitude filter. Longitudinally polarized focusing spots with uniform intensity, high axial resolution and small spot volume area are achieved in the carefully designed optical system. The number of focusing spots in the optical chain is controllable by adjusting the complex amplitude filter. As an example, a longitudinally polarized optical chain with seven uniform intensity focusing spots is obtained. The volume of each focusing spot is reduced by about seven times and the axial resolution is only one-fourth of that in a single lens system with the same parameters. The influence of optical axes mismatching and foci shifting on the focusing performance is also investigated. The focusing system with the complex amplitude filter permits a large focus shifting because of the elongated depth of focus. It is expected that this research can be further used in the field such as nanoparticle optical trapping and manipulating.

Finally, the general form of complex amplitude filters has been discussed. To address the optical power attenuation and the difficulty of fabrication issues of the complex amplitude filter because of its continuous varying profile, binary optics filter is designed using trigonometric Fourier series method. The focusing performance has been demonstrated and results show that binary optics filter can achieve the same focusing field shaping performance as the cosine function based complex amplitude filter. The binary optics filter also has the benefit of no significant power attenuation problem and it is much easier to fabricate than the complex amplitude filter with a continuous varying profile.

CHAPTER 4   NEAR-FIELD PHOTONIC NANOJET SHAPING USING CYLINDRICAL VECTOR BEAMS

In the previous chapter, cylindrical vector beams, such as radially polarized DG and BG are introduced into a high NA focusing system to achieve various unique sub-wavelength focusing patterns. In this chapter, cylindrical vector beams are used to illuminate dielectric microspheres in order to generate near-field sub-wavelength PNJs. Results show that one can precisely engineer the overall shape, intensity, location, and transverse and longitudinal size of the generated PNJ by controlling the polarization and the amplitude profile of the illumination beam.

When a microparticle such as a microsphere or microcylinder is properly illuminated, it can diffract light to form a tight focusing spot near the surface of the microparticle. This non-resonant near-field focusing spot is called photonic nanojet [69]. PNJ emerges at the shadow-side of the illuminated microparticle as a highly confined, high intensity sub-wavelength electromagnetic hot spot. It was first reported in 2004 [69], [72] when the group was studying the scattering of plane waves by lossless dielectric microcylinders and microspheres. Due to their special characteristics, PNJs have been widely studied in applications such as super-resolution imaging [91], [93], [97], [174] - [177], biomedical sensors [94] - [97], nanoparticle detection and manipulation [178], [179], all-optical switching [180] - [181], nano-photolithography [182] - [186], and Raman signal enhancement [187] - [189]. In addition to regular shaped microspheres and microcylinders, researchers have started looking into PNJs generated by microparticles of other shapes. Micro-cuboids [76] - [77], micro-disks [78] - [79], core-shell microspheres [80] - [81], micro-axicons [82] - [84], micro-spheroids [85] - [87], truncated microspheres [88], liquid crystals filled micro shells with controlled tuning of the refractive index [89] have all been explored to understand the characteristics of the generated PNJs and their potential applications.

The mechanism for generating a PNJ is a complex scattering, refraction and diffraction process. Previous research results have shown that PNJ emerges because of the

constructive interference between the illumination field, the scattered field, and the diffracted field [74]. To better understand the generation mechanism of PNJs, systematic studies have been conducted to investigate the impact of various parameters such as refractive index contrast, microparticle size and shape, and illumination wavelength on the generated PNJs [190]. Several approaches have been proposed and experimentally investigated to control and manipulate the intensity, lateral and/or longitudinal dimension of PNJs. For example, various functional structures have been fabricated on the microsphere [191] - [194] to achieve modification of the beam size and working distance of the photonic nanojet. However, plane waves were frequently used as the incident beams in most of the published literature. Only a few research groups adopted laser beams in their research. Laser source was used when Kim et al. experimentally observed and engineered PNJs in 2011 [90]. Later in 2014, Han et al. studied Gaussian beam [86] and zero-order Bessel beam [87] scattering by micro-spheroids. Gaussian beam was also used to generate highly confined PNJs from a crescent-shape refractive index profile in microsphere [195].

In addition, the polarizations of the incident beams also have an impact on the generated PNJs. In 2017, Darafsheh et al. analyzed the properties of the PNJs generated by dielectric microcylinders as a function of different key parameters [190]. These parameters included the size and refractive index of the microcylinder, index contrast between the microcylinder and the surrounding medium, shape of the microcylinder, polarizations, and wavelength of the incident plane wave light. In their study, only linearly polarized plane waves were examined. The results showed that higher intensity and smaller PNJ beam waist was achieved when the incident light was polarized perpendicular to the orientation of the microcylinder compared with the case when incident light was polarized parallel to the microcylinder. Also mentioned in [190], micro-particles illuminated by radially polarized beams can achieve tighter focusing and this effect is expected to be more pronounced with microspheres than with microcylinders due to the geometrical symmetry effect. Kim et al. [90] experimentally investigated how the wavelength, amplitude distribution, polarization, and a break in symmetry of the axial-symmetric structure of the illumination light affected the position, localization and shape of the PNJs. In their experiment results, hollow PNJs

were clearly observed from microspheres illuminated by a cylindrical vector laser beam with an azimuthal polarization.

In this chapter, characteristics of the PNJs generated from microspheres illuminated by different polarized beams were explored using the FDTD numerical calculation method. The polarized beams included linearly polarized beams, circularly polarized beams, radially polarized beams, and azimuthally polarized beams. Our work showed how the polarization of the illumination beam affected specific properties of the generated PNJ. These results will enhance our ability to engineer PNJs for various applications in different fields such as super-resolution imaging, nano-particle detection and trapping, and microparticle-assisted biomedical sensors.

4.1 NUMERICAL STUDY MODEL

The geometry of the numerical study model and the corresponding characteristic parameters of the generated PNJ are shown in Figure 36. The microsphere with a diameter of D and a refractive index of n_p was surrounded by a medium with a refractive index of n_m. The microsphere was illuminated by a polarized beam with a free space wavelength of λ. So, the wavelength in the medium was $\frac{\lambda}{n_m}$. In this work, we studied the impact of illumination polarizations on the obtained PNJs by characterizing the following 4 important parameters: the maximum field intensity, the effective focal length (EFL), the transverse and the longitudinal sizes of the PNJ. EFL was measured from the center of the microsphere to the maximum intensity point of the PNJ. The transverse and longitudinal sizes were represented by FWHM of the PNJ electric field distribution.
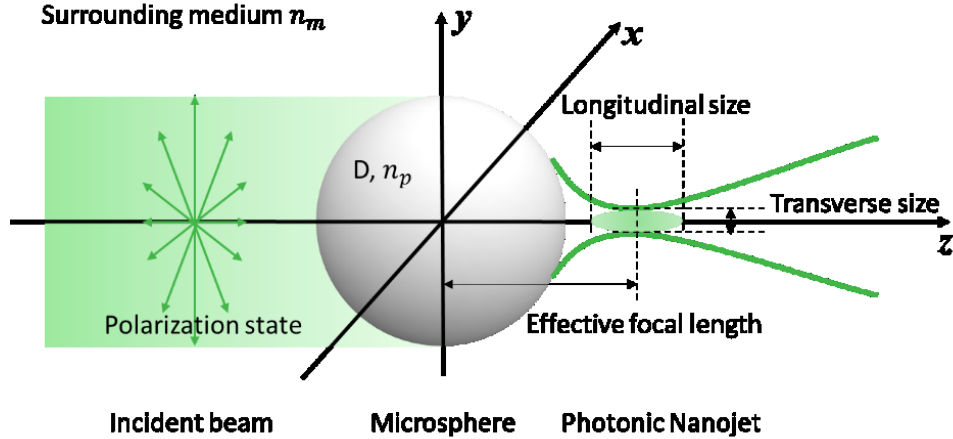
Figure 36 Schematic illustration of the model of PNJ generated by a microsphere

FDTD is a widely used numerical analysis method for computational electrodynamics. Time dependent Maxwell's Equations can be discretized in time and space and then solved in a leapfrog manner. It was used by [69] in 2004 to first demonstrate the existence of PNJs. FDTD numerical calculations were performed for our model to systematically investigate the influence of illumination polarizations on PNJs. Based on the theoretical study results in [190] and experimental work in [90], we chose a polystyrene (PS) microsphere (n_p=1.6) with a diameter D of 10 µm immersed in air (n_m=1) for calculation. These parameters were chosen so that sub-wavelength PNJs can always be obtained outside of microspheres for different illumination scenarios. In addition to the regular plane wave illumination cases, linearly, circularly, radially and azimuthally polarized Gaussian beams were carefully examined. Figure 37 illustrates the amplitude profiles and the polarization patterns of the 4 types of polarized Gaussian beams [113] applied to the microsphere model. The illumination wavelength was chosen as λ = 532 nm. In all cases, the illumination source was coherent and assumed to propagate along the z-axis. So E_z component of the illumination beam was set to zero to indicate that it was transversely polarized at the source plane before illuminating the microsphere.
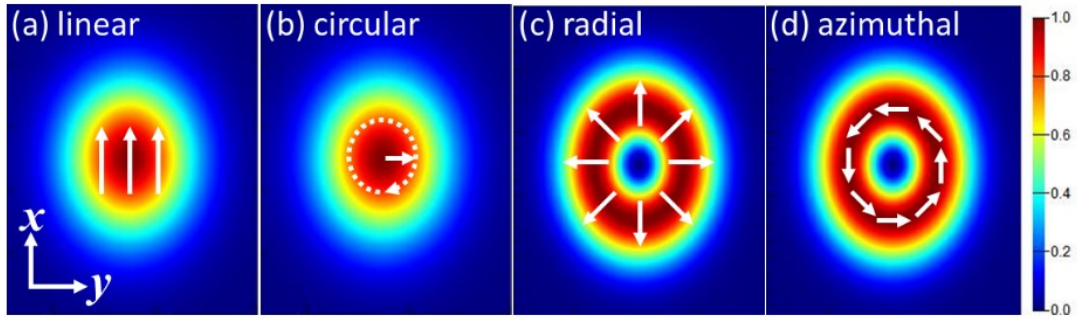
Figure 37 Illustration of the amplitude profiles and the polarization of the linearly **(a)**, circularly **(b)**, radially **(c)**, and azimuthally **(d)** polarized Gaussian beams. The amplitude distribution is normalized to the maximum amplitude for each of the polarization states.

When a polarized light beam propagates through a microsphere, its polarization state is modulated by the microsphere as illustrated in Figure 38. This polarization modulation phenomenon significantly affects the near-field intensity distribution and generates different types of PNJs. By studying the microsphere's near-field focusing performance, PNJs can be engineered for different application scenarios.
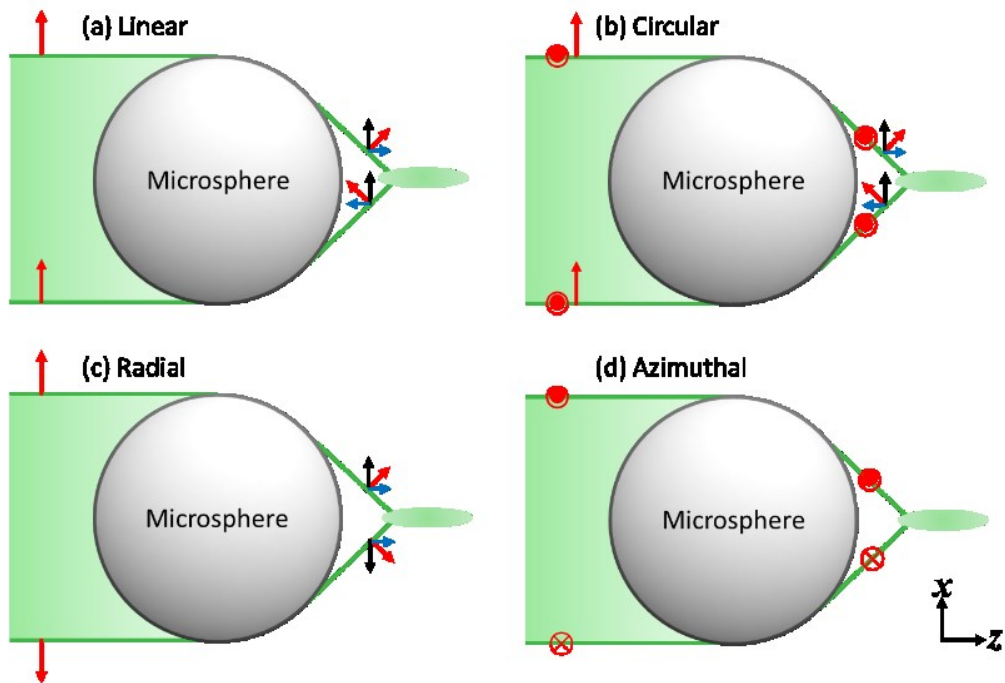
Figure 38 Illustration of polarization conversion by microspheres for **(a)** linear polarization, **(b)** circular polarization, **(c)** radial polarization, and **(d)** azimuthal polarization. The signs $\otimes$ and $\odot$ indicate the polarization of electromagnetic field pointing in and out of the plane, respectively.

Numerical error always exists, and the calculation results will never give exactly the correct solution. Therefore, it is important to understand the sources of numerical errors and methods that can be taken to reduce the error to an acceptable level for a specific model. It is desirable to balance between an acceptable level of error and the computational costs because reducing the error often involves increased calculation time and computational resources.

When Maxwell's equations are examined in FDTD, the updated value of the electric field in time at any point in space is dependent on the current value of the electric field and the numerical curl of the local distribution of the magnetic field in space. The magnetic field value can be updated in a similar manner. However, it becomes quite complicated to calculate the numerical curl when considering multiple dimensions. In 1966, Kane Yee [115] proposed spatially staggering the vector components of the electric field and magnetic field about rectangular unit cells of a Cartesian grid so that each electric field vector component is located midway between a pair of magnetic field vector components, and conversely. This scheme is known as Yee lattice, and remains at the core of many FDTD software. In addition, Yee proposed a leapfrog scheme for marching in time wherein the electric field and magnetic field updates are staggered so that the electric field updates are conducted midway during each time-step between successive magnetic field updates, and conversely. The explicit time-stepping scheme avoids the need to solve equations simultaneously, but it requires an upper bound on the time-step to ensure numerical stability. Generally, there are several sources of error that need to be considered in FDTD models.

First, the perfectly matched layer (PML) boundary condition. PML boundary conditions are implemented as an absorbing material and used to absorb incident light with minimal reflections. In practice, there will always be a small amount of reflections due to the discretization of the PML equations. The reflection from the PML can re-interfere with the source or the true scattered fields leading to incorrect results. This error can be monitored and minimized by adjusting the incident angle. Increasing the number of PML layers can also reduce the reflection.

Second, FDTD Yee grid error. In the FDTD numerical calculation process, the material at each position of the Yee cell is evaluated first to determine which material it is in. Then the electric field at that location is calculated using only that specific material property. One problem with the discretized Yee cell model is that it is unable to resolve structure variations occurs within any Yee cell and causes grid dispersion error. The dispersion relation on the FDTD grid is not identical to the free space case when the spatial and temporal mesh sizes are finite. Another problem is that it causes geometric error. It is impossible to resolve arbitrary geometric features when the spatial and temporal mesh sizes are finite. In principle, this type of error can be minimized by reducing the spatial and temporal mesh to 0. But computers always have finite precision numbers and there is always a limit to how small the mesh size can be used without introducing other type of numerical errors. In this numerical calculation model, non-uniform graded mesh has been utilized to reduce the FDTD grid dispersion and geometric errors in a highly computationally efficient way.

Third, finite sized temporal mesh. When the size of the temporal mesh is finite, the permittivity is not exactly the same as the theoretical model used to describe dispersive materials.

As discussed above, numerical calculation results will never give the "correct" answer, but more accurate solution is usually not available for a lot of models in practice. In order to determine the possible sources of error and quantify the level of error from the FDTD numerical calculation model, convergence testing of results from an FDTD simulation is necessary. To understand the convergence of a certain model, one can vary certain parameters, such as the mesh size, in multiple steps.

$$\Delta\sigma(i) = \sqrt{\frac{\int [\sigma(i) - \sigma(i-1)]^2 d\lambda}{\int [\sigma(i)]^2 d\lambda}} \tag{4.1}$$

where $i=1, \ldots, N$ is the calculation step, σ_i and σ_{i-1} represent the numerical calculation results of the parameter under testing at adjacent calculation steps. Ideally, we want to find the point where this quantity becomes zero which means the results stop changing. In practice, we usually see that $\Delta\sigma(i)$ becomes flat at certain point which means that the error in the model is dominated by another parameter, but this parameter under testing still has a contribution to the calculation error. It is also useful to considering the absolute error:

$$\Delta\sigma_a(i) = \sqrt{\frac{\int[\sigma(i)-\sigma(N)]^2 d\lambda}{\int[\sigma(i)]^2 d\lambda}} \tag{4.2}$$

This definition can give us a good estimate of the absolute error if we assume the result for a certain parameter under testing at step N is much closer to the "correct" solution than at step i. Note that this definition won't give a good estimate when i is approaching N where the error will be significantly underestimated. Nonetheless, these quantities will give us the best estimate of errors in the absence of the exact solution.

The materials used in the microsphere focusing model are not highly dispersive in the optical range, but the microsphere has a smooth curved surface. It is challenging to resolve a smoothly varying surface using Yee grid. However, this issue can be addressed by reducing the mesh size because the microsphere structure is micrometer scale. Specifically, non-uniform graded mesh has been applied to the critical region including the incident side and the shadow side of the microsphere to reduce the FDTD grid error in a highly computationally efficient way. The convergence testing process starts with the investigation of PML boundary condition because the mesh size parameter takes longer time to optimize. Due to the complexity of three-dimensional simulations and the limitation on computational resources, the contribution from each source to the overall error below 10^{-3} (0.1%) is considered acceptable in this model. In order to meet this goal, 8 layers of PML is used and 10 μm (approximately 20λ) is chosen as the distance from the structure to the PML. The minimum mesh size at the critical region is set at 1 nm after convergence testing.

4.2 PLANE WAVE ILLUMINATION

Due to its simplicity, a plane wave is frequently used to generate a PNJ [69], [72], [190]. In this study, we showed the PNJ generated in our model with a linearly polarized plane wave illumination as the first step. Then a circularly polarized plane wave was introduced to our model. The results for the linearly polarized plane wave illumination case were used as a reference to evaluate other cases in the following sections.

4.2.1 Linear polarization

When a microsphere is illuminated by the x- axis linearly polarized plane wave, the total field intensity $|E_t|^2$ distribution of the PNJ in the transverse plane (xy-plane) shows an elongated shape along the illumination light polarization direction as shown in Figure 39(a). The $|E_x|^2$, $|E_y|^2$, and $|E_z|^2$ components, normalized to the maximum total intensity, are also shown in Figure 39(b)-(d). Obviously, the $|E_x|^2$ component dominates the generated PNJ and the $|E_y|^2$ component is nearly zero in the transverse plane. However, it is worth mentioning that a longitudinal component $|E_z|^2$ is also introduced by the microsphere in the transverse plane. The explanation is that light rays converge strongly, and their polarization rotates accordingly when they pass through the microsphere as illustrated in Figure 38(a). Clearly, both $|E_x|^2$ component (black arrow) and $|E_z|^2$ component (blue arrow) exist after polarization conversion. The black arrows pointing in the same direction meaning $|E_x|^2$ components have a same phase, and thus constructive interferences are shown on the optical axis. However, the blue arrows on the upper part and lower part of the microsphere pointing in the opposite directions means a π phase difference is introduced in the $|E_z|^2$ components. Hence, destructive interferences occur at the center and constructive interferences occur at outer regions. The longitudinal component is not as strong as the $|E_x|^2$ component, but it still has a significant contribution to the total field and produce a PNJ with an elongated shape along the x-axis in the transverse plane. Intuitively, in the case of the y-axis linearly polarized plane wave

illumination, the PNJ will show the same elongated shape but the long axis will be parallel to the y-axis.

The intensity distributions of the total field, the $|E_x|^2$, $|E_y|^2$, and $|E_z|^2$ components in the longitudinal plane (xz-plane) are shown in Figure 39(e)-(h). The white curves in these figures represent the microsphere surface. A high intensity sub-wavelength near-field PNJ is obtained.

Figure 39 Transverse and longitudinal electric field intensity distribution of the PNJ generated with the x-linearly polarized plane wave illumination. **(a)-(d)** intensity distribution of total field, $|E_x|^2$, $|E_y|^2$, and $|E_z|^2$ components in the transverse plane, respectively. **(e)-(h)** intensity distribution of total field, $|E_x|^2$, $|E_y|^2$, and $|E_z|^2$ components in the longitudinal plane, respectively. All the data are normalized to the maximum total intensity and the white curve in the bottom figures represent the microsphere surface unless otherwise specified. The calculation parameters, $\lambda = 532$ nm, $n_m = 1.0$, $n_p = 1.6$, D $= 10$ μm, remain unless otherwise specified.

The intensity profile of different components along the x-, y- and z- axes are shown in Figure 40. The normalized maximum intensity in the total field is $|E_t|^2/|E_0|^2 = 599$, where $|E_0|^2$ represents the incident intensity. We can see from Figure 39 that the contribution from $|E_y|^2$ component is negligible because the incident field is purely x- axis linearly polarized. Along the x-axis (Figure 40(a)), $|E_z|^2$ component has two peaks and the intensity of the peaks are approximately 20% of the maximum total field intensity. The distance between these two peaks is 380 nm. The existence of these two peaks causes the

90

slight expansion of the width of the PNJ in the *x*-axis direction. Along the *y*-axis (Figure 40(b)), the total field $|E_t|^2$ is almost identical to $|E_x|^2$. Due to the asymmetric contribution of the $|E_z|^2$ component on the *x*- and *y*- axes, the generated PNJ shows an elongated shape in the transverse plane accordingly. The FWHM of the total intensity along the *x*-axis, d_x, is approximately 400 nm while the dimension along the *y*-axis, d_y, is approximately 260 nm. Considering the incident wavelength is 532 nm, the lateral dimension of the generated PNJ on the *y*-axis is less than $\lambda/2$. In the *z*-axis direction as shown in Figure 40, there are multiple intensity peaks inside the microsphere. The dimension of the PNJ in the longitudinal direction is also much larger than in the transverse plane. The EFL defined as the distance from the center of the microsphere to the point where the maximum intensity of the PNJ is located is 5.05 µm. Note that the radius of the microsphere is 5 µm. Since the maximum intensity point is very close to the surface of the microsphere and the field distribution inside the microsphere is quite complex in the longitudinal direction. It is not feasible to use FWHM to represent the longitudinal size of the PNJ. In fact, the longitudinal size of PNJ d_z is defined as a measurement starting from the maximum intensity point to one of the half maximum point which is located in the opposite direction of the microsphere. In this case, d_z = 530 nm, is about the size of one wavelength.

Figure 40 Intensity distribution of PNJ generated with the x-linearly polarized plane wave illumination in the transverse plane along the **(a)** *x*-, **(b)** *y*- axes, and in the longitudinal plane along the **(c)** *z*-axis, respectively. The light blue shading in **(c)** indicates the field intensity variations inside the microsphere.

4.2.2 Circular polarization

In many applications, the elongated shape in one direction of the focusing field in the transverse plane under linear polarization illumination condition is undesirable. In contrast, a circularly polarized plane wave illumination can produce a perfectly symmetric focusing spot with respect to the optical axis in the transverse plane, as shown in Figure 41(a). In this case, the contribution of the two transverse components $|E_x|^2$ and $|E_y|^2$ are identical. The field distribution results in the transverse plane in Figure 41(b) and (c) demonstrate that $|E_x|^2$ and $|E_y|^2$ components have similar shape and intensity. Figure 42 (a) and (b) quantitatively verify that $|E_x|^2$ and $|E_y|^2$ components are equivalent in this case. In the meantime, the $|E_z|^2$ component also has a contribution to the total field similar to the linear polarization case even though its contribution is much smaller compared to the $|E_x|^2$ and $|E_y|^2$ components. It should be noted that the $|E_z|^2$ component is ring-shaped (Figure 41(d)) as opposed to two peaks along one axis (Figure 39(d)) due to the time-varying nature of the electric field vectors of the circular polarization state. Therefore, a symmetric spot in the transverse plane is obtained when these components are added together to form the PNJ. The disadvantage of the ring-shaped $|E_z|^2$ component is that it tends to enlarge the size of the generated PNJ in the transverse plane.

Detailed electric field data can be extracted from Figure 42 to characterize the obtained PNJ. The normalized maximum intensity in the total field is still $|E_t|^2/|E_0|^2 = 599$ and the EFL remains 5.05 µm since it's still under plane wave illumination condition. The only difference here is the polarization state. The $|E_x|^2$ and $|E_y|^2$ components each contribute approximately 50% to the maximum total intensity. While the maximum intensity of the $|E_z|^2$ component only reaches approximately 12% of the maximum intensity of the total field. The transverse dimensions of the total field are $d_x = d_y = 320$ nm. Considering both the $|E_x|^2$ and $|E_y|^2$ components only have a transverse size of 280 nm, it is clear to see the negative impact of the $|E_z|^2$ component on expanding the transverse size of the generated PNJ.

Figure 41 Transverse and longitudinal electric field intensity distribution of the PNJ generated with the circularly polarized plane wave illumination. **(a)-(d)** intensity distribution of total field, $|E_x|^2$, $|E_y|^2$, and $|E_z|^2$ components in the transverse plane, respectively. **(e)-(h)** intensity distribution of total field, $|E_x|^2$, $|E_y|^2$, and $|E_z|^2$ components in the longitudinal plane, respectively.

Figure 42 Intensity distribution of PNJ generated with the circularly polarized plane wave illumination in the transverse plane along the **(a)** x-, **(b)** y- axes, and in the longitudinal plane along the **(c)** z- axis, respectively.

In practice, a circularly polarized beam can be obtained using a quarter-wave plate to convert a linearly polarized beam into either left or right circular polarization states. Alternatively, liquid crystal devices such as spatial light modulators can be used to modulate laser light at will. Since right and left circular polarization possess the same symmetry characteristics, this research only shows results for right circular polarization. For the elliptical polarization illumination, the shape of the PNJ in the transverse plane

varies continuously between the shapes of the linear cases and the circular cases depending on the phase and the strength of the two polarization axes.

4.3   GAUSSIAN BEAM ILLUMINATION

Most lasers produce a beam that can be approximated as a Gaussian beam whose electric and magnetic field amplitude profiles are characterized by the Gaussian function. Here, the electric field amplitude profile of the Gaussian beam is defined as $E = \exp\left(-\frac{x^2+y^2}{\omega_0^2}\right)$, where ω_0 is the beam waist radius, x, and y are rectangular coordinates. The beam size was set to $\omega_0 = 5$ µm so that the Gaussian beam can fully illuminate the microsphere. As for the polarization state of the Gaussian beam, two new polarization states - radial and azimuthal polarizations - are thoroughly studied. The amplitude profiles and the polarizations of these four types of polarized Gaussian beams are shown in Figure 37.

4.3.1   Linear polarization

In the case of linearly polarized Gaussian beam illumination, the results are shown in Figure 43 and Figure 44. Compared to the linearly polarized plane wave, the electric field intensity distributions have almost the same shape due to the same polarization state. The $|E_x|^2$ component still has the most contribution to the total field in the x-linearly polarized Gaussian beam illumination scenario. The $\left|E_y\right|^2$ component has nearly zero presence in the total field. The two weak peaks of the $|E_z|^2$ component, which are approximately 13% of the maximum total intensity and located 420 nm apart, slightly expand the total field in the x-axis direction.

In addition to the influence of the polarization state, the source intensity profile difference also has an obvious impact on the PNJ. First, the normalized maximum intensity in the total field is $|E_t|^2/|E_0|^2 = 206$, a smaller number compared to the plane wave case. Note that the source amplitude is set to 1 for both the plane wave and the Gaussian beam in our

calculation. Therefore, the maximum intensity in the total field is lower in the Gaussian beam case simply because the Gaussian beam pumps less energy into the system. In practice, laser beams usually have very high intensity so the obtained PNJs under laser beam illumination can also achieve very high intensity.
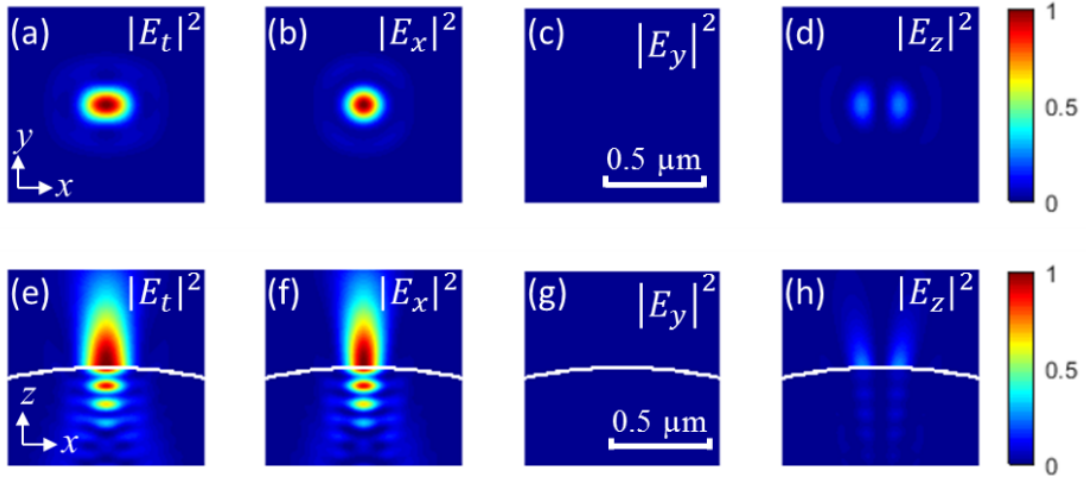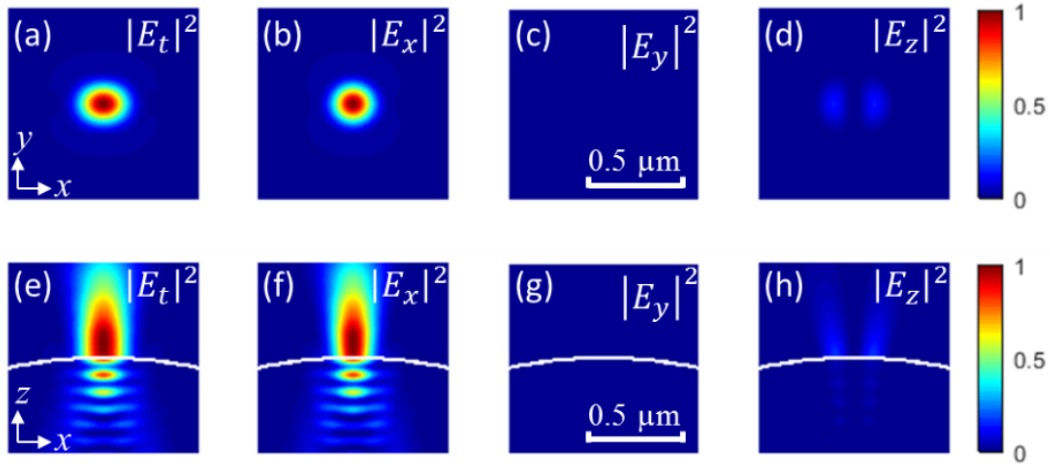

Figure 43 Transverse and longitudinal electric field intensity distribution of the PNJ generated with the linearly polarized Gaussian beam illumination. **(a)-(d)** intensity distribution of total field, $|E_x|^2$, $|E_y|^2$, and $|E_z|^2$ components in the transverse plane, respectively. **(e)-(h)** intensity distribution of total field, $|E_x|^2$, $|E_y|^2$, and $|E_z|^2$ components in the longitudinal plane, respectively.
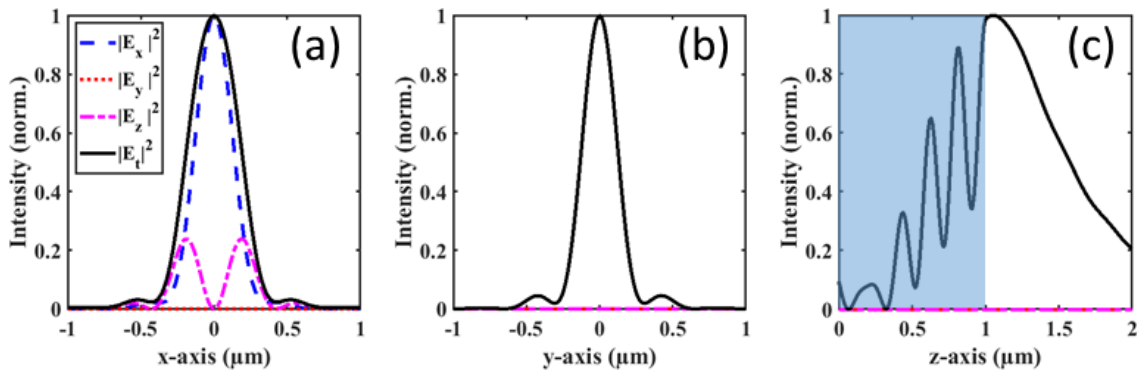

Figure 44 Intensity distribution of PNJ generated with the linearly polarized Gaussian beam illumination in the transverse plane along the **(a)** x-, **(b)** y- axes, and in the longitudinal plane along the **(c)** z-axis, respectively.

Second, compared with the plane wave excitation mode, the obtained PNJs have almost the same transverse dimensions but a much larger longitudinal size for the Gaussian beam excitation mode. The transverse dimensions of the generated PNJ, which are $d_x =$

400 nm, $d_y = 320$ nm, and the longitudinal dimension $d_z = 620$ nm can be obtained from Figure 44. Also, the EFL is 5.16 µm in the Gaussian beam illumination scenario compared to an EFL of 5.05 µm in the plane wave case. So, the PNJs emerge at a location farther away from the surface of the microsphere than those generated by the plane waves. These phenomena can be explained by the spherical aberration effect of the microsphere [112]. Light rays that strike a spherical surface off-center are refracted more than ones that strike close to the center. Spherical aberration causes the incoming light to end up focusing at different points after propagating through a spherical object. The object under study here is a perfect microsphere so it has strong spherical aberration. The illumination beam is a Gaussian beam which has high intensity along the optical axis and a relatively low intensity in the outer region. Therefore, the center of the Gaussian beam will have a much larger contribution to the focusing field than the outer part. That's why the location of the maximum intensity point in the longitudinal direction moved away from the microsphere surface when the illumination light changed from a plane wave to a Gaussian beam.

4.3.2 Circular polarization

Figure 45 and Figure 46 show the results for the circularly polarized Gaussian beam illumination case. As discussed in the previous section, the shape of the PNJ in the transverse plane is very similar to the plane wave illumination except for some details caused by the source intensity profile difference.

The normalized maximum intensity in the total field is the same as the linearly polarized Gaussian beam case $|E_t|^2/|E_0|^2 = 206$. The total field in the transverse plane is symmetric with respect to the optical axis and the transverse dimensions are $d_x = d_y = 360$ nm. Both the $|E_x|^2$ and $|E_y|^2$ components have a transverse size of 320 nm. Even though the longitudinal component $|E_z|^2$ is very weak. The peak intensity of $|E_z|^2$ only accounts for approximately 7% of the maximum total intensity. It still has a negative influence of expanding the transverse size of the PNJ from 320 nm to 360 nm. In the longitudinal

direction, $d_z = 620$ nm and EFL $= 5.16$ μm remain the same as the linearly polarized Gaussian beam case. Strong spherical aberration still exists.
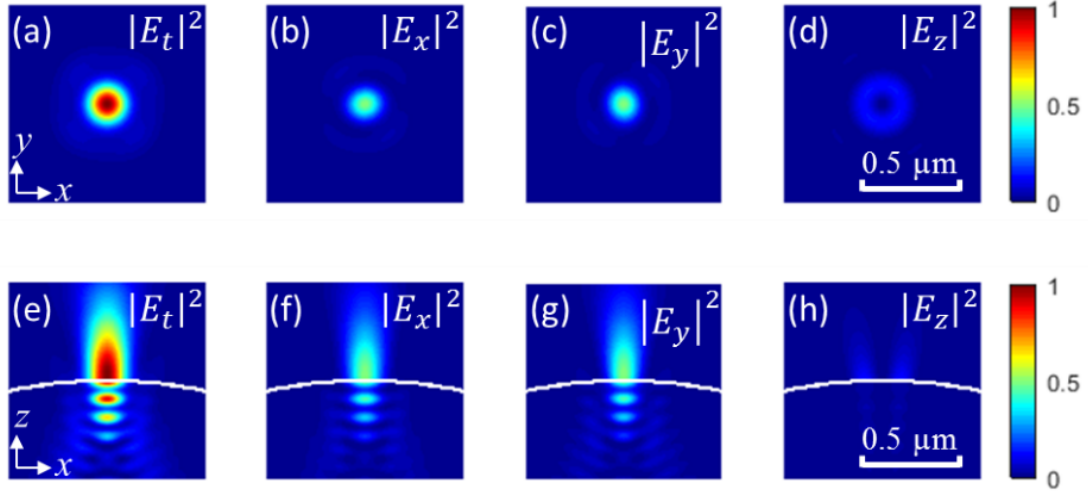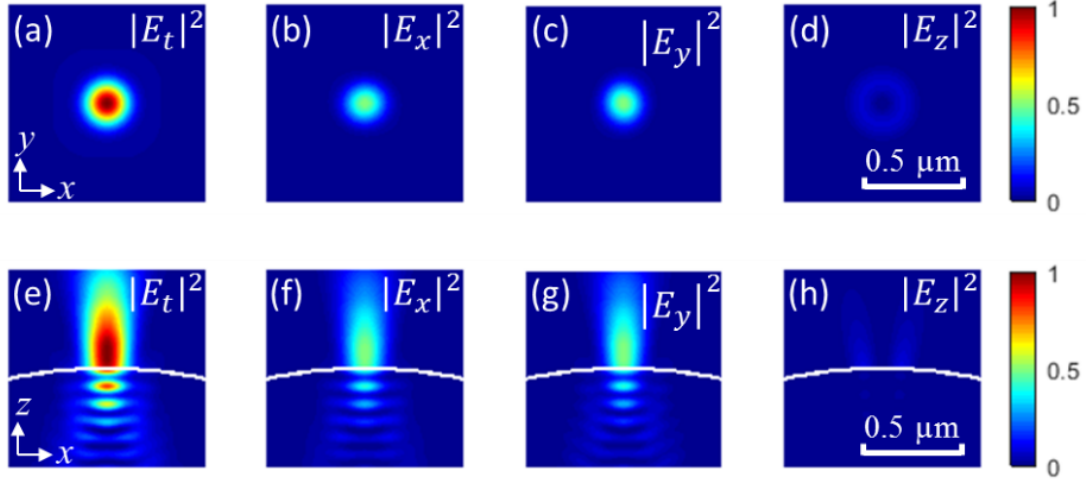

Figure 45 Transverse and longitudinal electric field intensity distribution of the PNJ generated with the circularly polarized Gaussian beam illumination. **(a)-(d)** intensity distribution of total field, $|E_x|^2$, $|E_y|^2$, and $|E_z|^2$ components in the transverse plane, respectively. **(e)-(h)** intensity distribution of total field, $|E_x|^2$, $|E_y|^2$, and $|E_z|^2$ components in the longitudinal plane, respectively.
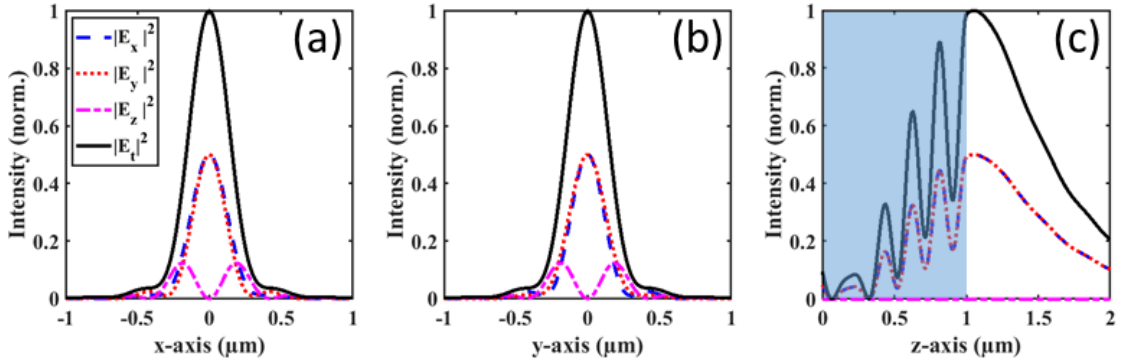

Figure 46 Intensity distribution of PNJ generated with the circularly polarized Gaussian beam illumination in the transverse plane along the **(a)** x-, **(b)** y- axes, and in the longitudinal plane along the **(c)** z- axis, respectively.

4.3.3 Radial polarization

As depicted in Figure 37(c), radially polarized Gaussian beam has all the field vectors aligned in the radial direction. The amplitude profile shows a null center in the transverse plane due to the transverse field continuity [113]. The PNJ produced by a radially polarized Gaussian beam is presented in Figure 47. In the transverse plane, all three components have significant contributions to the total field. If we examine the polarization conversion effect by the microsphere as depicted in Figure 38(c), we can see that the radial components of the light rays after the microsphere (black arrows) have opposite directions for the upper and lower parts, which means a π-phase difference is introduced for the radial component. Thus, destructive interference occurs on the optical axis for $|E_x|^2$ and $|E_y|^2$ components. Zero intensity in the center and two peaks along the x-axis and y-axis can be expected for the $|E_x|^2$ and $|E_y|^2$ components. As for the longitudinal component, the vectors (blue arrows) are all pointing in the same direction, which means they are all in phase, so the electric field has constructive interferences on the optical axis.
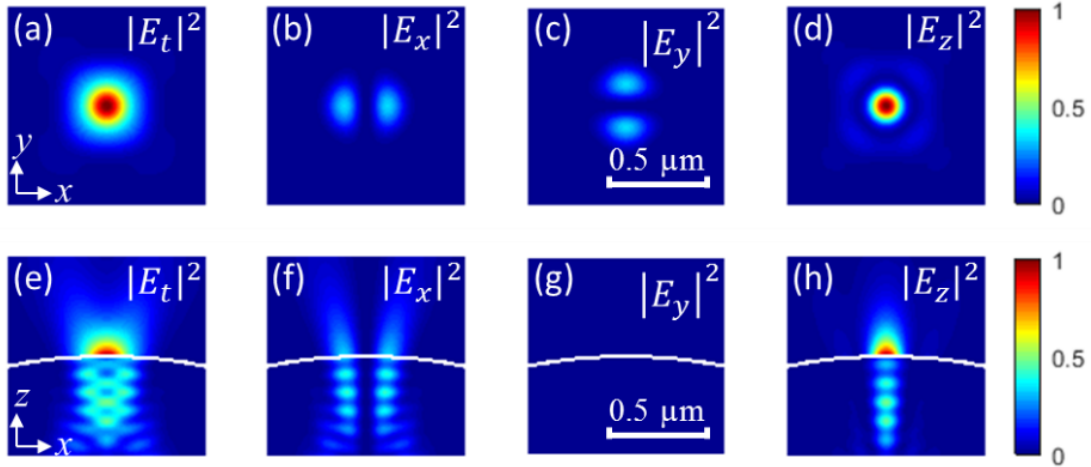
Figure 47 Transverse and longitudinal electric field intensity distribution of the PNJ generated with the radially polarized Gaussian beam illumination. **(a)-(d)** intensity distribution of total field, $|E_x|^2$, $|E_y|^2$, and $|E_z|^2$ components in the transverse plane, respectively. **(e)-(h)** intensity distribution of total field, $|E_x|^2$, $|E_y|^2$, and $|E_z|^2$ components in the longitudinal plane, respectively.

The normalized maximum intensity in the total field is $|E_t|^2/|E_0|^2 = 300$. If we examine the field intensity data of each component along the x-, y-, and z- axes, as shown in Figure

48, it is obvious that the longitudinal component $|E_z|^2$ has the major contribution to the total field. But the two transverse components $|E_x|^2$ and $|E_y|^2$ expand the transverse dimension of the PNJ substantially. Specifically, the maximum intensity of $|E_x|^2$ and $|E_y|^2$ can reach as high as 33% of the maximum total intensity. The distance between these two peaks is 440 nm. The transverse components $|E_x|^2$ and $|E_y|^2$ cause the FWHM of the total field $|E_t|^2$ in the transverse plane to expand up to 400 nm, while the FWHM of the $|E_z|^2$ component in the transverse plane is only 260 nm.

Along the optical axis, the longitudinal size of PNJ d_z is only 160 nm, well below half of the illumination wavelength. A very small EFL of 5.01 μm also occurred in this illumination mode. In contrast to the near-field numerical calculation results, a similar effect is also demonstrated in a far-field high NA focusing system [113]. Theoretically, three-dimensional sub-diffraction limited PNJ can be achieved if we can design a method to suppress the contribution from the radial component while enhancing the contribution from the longitudinal component at the same time.
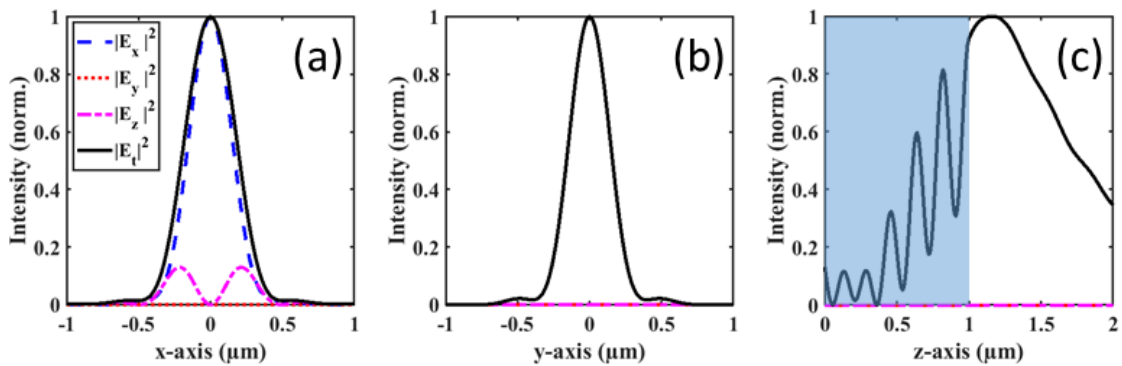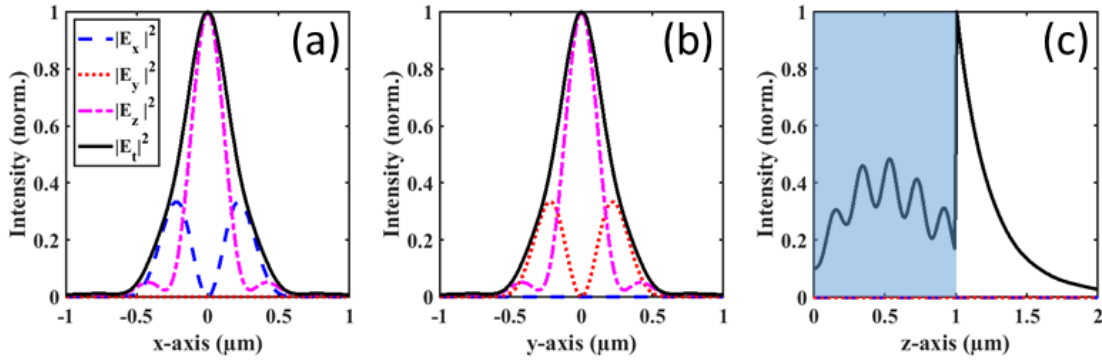

Figure 48 Intensity distribution of PNJ generated with the radially polarized Gaussian beam illumination in the transverse plane along the **(a)** x-, **(b)** y- axes, and in the longitudinal plane along the **(c)** z- axis, respectively.

4.3.4   Azimuthal polarization

The polarization pattern and the amplitude profile for an azimuthally polarized Gaussian beam is depicted in Figure 37(d). The amplitude profile also shows a null center in the

transverse plane. Unlike the beams studied in the previous sections, azimuthally polarized Gaussian beam can generate a PNJ with a hollow center. In 2011, Kim et al. [90] experimentally observed a hollow PNJ when a 10 μm microsphere was illuminated by an azimuthally polarized laser beam. The existence of the hollow center is due to the fact that the orientation of the local polarization after the microsphere is orthogonal to the optical axis and no longitudinal component $|E_z|^2$ exists, as is shown in Figure 38(d). The normalized maximum intensity enhancement achieved by the hollow PNJ outside the microsphere is $|E_t|^2/|E_0|^2 = 300$. The generated PNJ is purely transversely polarized. Hence, the contribution of $|E_z|^2$ component is zero as shown in Figure 49(d). Also, due to the axial symmetrical nature of the azimuthally polarized beams, the field vectors located at the opposite end around the optical axis always have a π-phase difference. So, destructive interference can be expected on the optical axis for the $|E_x|^2$ and $|E_y|^2$ components as shown in Figure 49(b) and (c). The ultimate effect is a hollow center formed in the total field in the transverse plane as depicted in Figure 49(a). The cross-section view of the PNJ with a hollow center is presented in Figure 49(e-h).
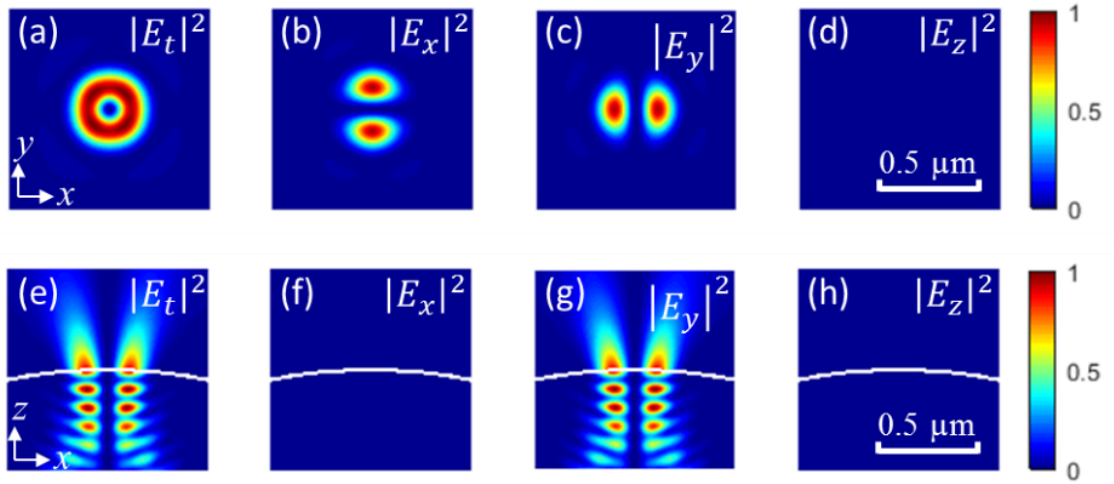
Figure 49 Transverse and longitudinal electric field intensity distribution of the PNJ generated with the azimuthally polarized Gaussian beam illumination. **(a)-(d)** intensity distribution of total field, $|E_x|^2$, $|E_y|^2$, and $|E_z|^2$ components in the transverse plane, respectively. **(e)-(h)** intensity distribution of total field, $|E_x|^2$, $|E_y|^2$, and $|E_z|^2$ components in the longitudinal plane, respectively.
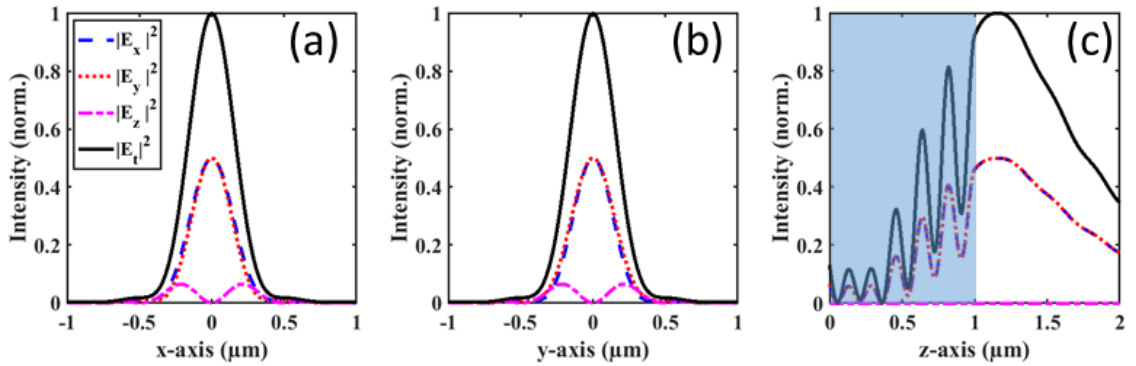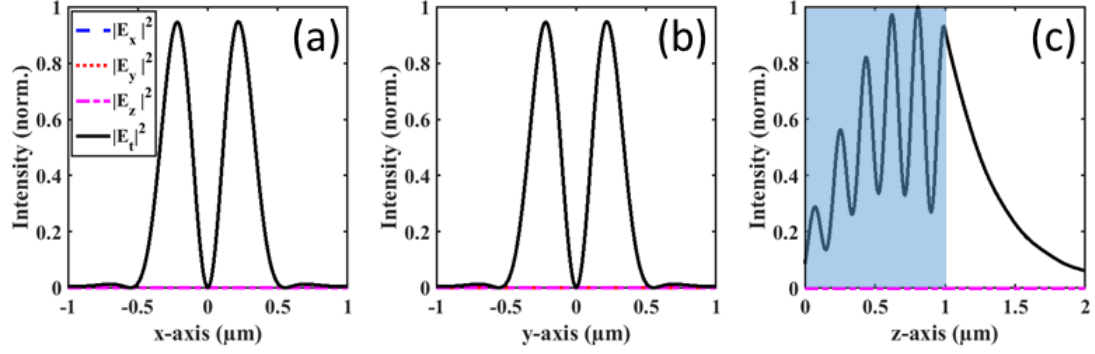
Figure 50 Intensity distribution of PNJ generated with the azimuthally polarized Gaussian beam illumination in the transverse plane along the **(a)** *x*-, **(b)** *y*- axes, and in the longitudinal plane along the **(c)** maximum intensity in the *z*- axis direction, respectively.

Figure 49(e) and (g) shows that the generated PNJ is extremely close to the surface of the microsphere. Intensity distribution of the PNJ outside of the microsphere in the transverse plane along the *x*- and *y*-axes are shown in Figure 50(a) and (b). The total field intensity along the *z*-axis is zero because all three components on the *z*-axis are zero. The generated PNJ has a hollow center in the azimuthal illumination case. Instead of showing all zero field intensities for the three components along the z-axis, Figure 50(c) shows the field intensity variations in the *z*-axis direction at a transverse maximum intensity point. It is worth mentioning that several extremely high field intensity hot spots exist inside the microsphere as shown in Figure 49(e) and (g), and Figure 50(c). Most of the energy is trapped inside the microsphere when it is illuminated with the azimuthally polarized Gaussian beam.

To better understand the properties of this hollow PNJ, two important characterization parameters for the hollow PNJ are introduced. The size of the hollow center d_{hc} which is represented by the distance of the two maximum intensity peaks in Figure 50(a) or (b) is 440 nm. More importantly, the thickness of the obtained hollow PNJ $d_{thickness}$ can be measured by the FWHM of the peaks in Figure 50(a) or (b) and it is below 200 nm in this calculation. This unique hollow PNJ has great potential in applications such as particle trapping and manipulation.

4.4 SUMMARY

Table 3 exhibits the results of our numerical modelling of PNJs generated by plane waves and Gaussian beams with different polarizations.

Table 3 Characteristics of PNJs generated by plane waves and Gaussian beams with different polarizations*

Illumination Beam		Maximum Intensity	Transverse Plane $|E_t|^2$		Longitudinal Plane $|E_t|^2$	
		$\dfrac{|E_t|^2}{|E_0|^2}$	d_x (nm)	d_y (nm)	d_z (nm)	EFL (µm)
Linear	Plane Wave	599	400	260	530	5.05
	Gaussian Beam	206	400	320	620	5.16
Circular	Plane Wave	599	320	320	530	5.05
	Gaussian Beam	206	360	360	620	5.16
Radial	Gaussian Beam	300	400	400	160	5.01
Azimuthal	Gaussian Beam	300	d_{hc} = 440 nm; $d_{thickness}$ = 200 nm			

* d_x is the FWHM of the total field intensity along the x-axis. d_y is the FWHM of the total field intensity along the y-axis. d_z is defined as a measurement starting from the maximum intensity point of a PNJ to one of the half maximum point which is located at the opposite direction of the microsphere. EFL is the distance from the center of the microsphere to the point where the maximum intensity of the PNJ is located. d_{hc} is the diameter of the hollow center of a hollow PNJ which is represented by the distance of the two maximum intensity peaks along the x- axis or the y-axis. $d_{thickness}$ is the thickness of a hollow PNJ which is represented by the FWHM of the total field intensity peaks along the x- axis or the y-axis.

After studying the PNJs generated by illumination beams with different intensity profiles and polarizations, we can draw the following conclusions. First, linear polarization causes the elongated shape of the PNJ in one direction in the transvers plane because of contributions from the $|E_z|^2$ component. Sub-diffraction limit PNJs can still be achieved in the non-polarization direction in the transverse plane. Second, circular polarization can produce a PNJ whose transverse field intensity profile is symmetric with respect to the optical axis. Third, Gaussian beams with linear and circular polarization states generate

similar PNJs as their plane wave counterparts. But the spherical aberration is more evident in the Gaussian beam illumination scenario which causes the PNJs to emerge at a farther distance from the surface of the microsphere and exhibit a much larger longitudinal size. Forth, PNJs generated by radially polarized Gaussian beams are mainly formed by the sub-diffraction limited longitudinal component $|E_z|^2$. Generally, the transverse components $|E_x|^2$ and $\left|E_y\right|^2$ greatly expand the transverse dimensions of the PNJs. However, a 3-D sub-diffraction limited PNJ can be achieved theoretically if one can suppress the radial components and enhance the longitudinal component simultaneously. Finally, azimuthally polarized Gaussian beams can generate a unique hollow PNJ which may be very useful in applications such as nanoparticle trapping.

To thoroughly study the impact of the illumination polarization on the obtained PNJs, we numerically investigated the model of a polystyrene microsphere illuminated by plane waves and Gaussian beams with different polarizations. We started by studying the PNJs generated by linearly and circularly polarized plane waves. Then we explored PNJs obtained with linearly, circularly, radially, and azimuthally polarized Gaussian beams. To conclude, we have shown that the polarizations of the illumination beams have a significant impact on the properties of the obtained PNJs. By controlling the polarization and the amplitude profile of the illumination beam, one can precisely engineer the overall shape, intensity, location, and transverse and longitudinal size of the generated PNJ at will for different applications. Our study clarifies several important characteristics of PNJs generated with different illumination schemes. The results clearly showed that engineering the polarization of the illumination light is an effective method to generate different PNJs and to make them suitable for various application scenarios.

CHAPTER 5   CONCLUSION AND FUTURE WORK

In conclusion, this project theoretically studied the engineering of the focusing field in both far-field and near-field using optical vector beams in detail.

In far-field, a radially polarized DG beam is studied first. The radially polarized doughnut Gaussian beam is introduced to a high numerical aperture focusing system to generate a sub-wavelength focal spot. The focusing characteristics are theoretically investigated based on the Richards-Wolf diffraction integral theory [113] - [116]. Numerical results show that a focusing spot with sub-wavelength lateral size and short DOF can be obtained when the radially polarized doughnut Gaussian incident beam is properly designed.

To achieve long depth of focus, a cosine function based complex amplitude filter is designed to increase the length of DOF in a high NA focusing system. The cosine function based complex amplitude filter can split the focusing field into two or more components in the optical axis direction. In principle, the focusing field can be designed to achieve long DOF by optimizing the m_p parameter of the complex amplitude filter.

By taking advantage of the designed complex amplitude filter, hollow beams with a long focal depth are generated from a radially polarized BG beam with a second-order vortex phase filter. The null intensity on the optical axis is achieved by introducing the second-order vortex. The long focal depth is a result of the amplitude filtering based on cosine functions and Euler transformation. Numerical results indicate that the DOF of a hollow beam is improved from 0.96λ to 3.4λ with a N = 2 complex amplitude filter design. The intensity distribution twist phenomenon of the x- and y-polarized components around the optical axis due to the introducing of the vortex phase is also discussed.

A longitudinally polarized optical chain is generated in a 4π high NA focusing system. The radially polarized BG incident beam is modulated by a complex amplitude filter. Longitudinally polarized focusing spots with uniform intensity, high axial resolution and

small spot volume area are achieved using the carefully designed optical system. The number of the focusing spots in the optical chain can be designed by adjusting the parameters of the complex amplitude filter. As an example, a longitudinally polarized optical chain with seven uniform intensity focusing spots is demonstrated successfully. The volume of each focusing spot is reduced by approximately seven times and the axial resolution is only one-fourth of that in a single lens system with the same parameters. The influence of optical axes mismatching and foci shifting on the focusing performance is also discussed in detail.

The impact of the illumination polarization on the obtained PNJs is numerically investigated for the model of a Polystyrene microsphere illuminated by plane waves and Gaussian beams with different polarizations. Both linearly and circularly polarized planes waves and linearly, circularly, radially, and azimuthally polarized Gaussian beams are used to generate PNJs. Results have shown that the polarizations of the illumination beams have a significant impact on the properties of the generated PNJs. By controlling the polarization and the amplitude profile of the illumination beam, one can precisely engineer the overall shape, intensity, location, and transverse and longitudinal size of the generated PNJ at will for different applications. The results clearly show that engineering the polarization of the illumination light is an effective method to generate different PNJs and to make them suitable for various application scenarios.

For future work, different cylindrical vector beams can be generated using programmable liquid crystal on silicon (LCOS) spatial light modulator [196] - [198] and the designed complex amplitude filters can be implemented using binary optics. Its amplitude filtering performance can then be characterized. Experimental verification of the optical tube and optical chain needs to be performed. These unique focusing fields have great potential in various application scenarios.

In this project, preliminary experimental work has been performed to investigate PNJs. Polystyrene microspheres were dispersed in liquid and then transferred to a coverslip using a pipette. The microspheres can be illuminated from the bottom side and the obtained PNJs

can be examined from the top side. The experiment was carried out using a Zeiss Axio Imager Z2 microscope. A 40× water immersion objective was used to observe the generated PNJs. This microscope system has a high precision three-dimensional motorized stage. Therefore, the focal plane can be scanned in the z direction at a high precision. In the experiment, a series of images were taken at different z level and then analyzed using an image processing software. PNJs were clearly observed at the top side close to the surface of the microspheres. The image data had also been used to quantify the location of the PNJs and characterize the lateral dimension of the generated PNJs.

Due to the limitation of hardware resources available in the lab to generate various CVBs and observe the obtained PNJs in the near-field. Experimental verification of PNJs shaped by various optical vector beams is one of the most exciting works that can be done in the future. A LCOS module can be used to generate various CVBs and a near-field scanning optical microscope can be used to image the generated PNJs. This work could help researchers better understand the mechanism of PNJ generation and its ability for super-resolution imaging. Integrated nano-micro structures that works effectively as amplitude or phase filters can be explored as well to further engineer the generated PNJs.

BIBLIOGRAPHY

[1] E. Hecht. Optics. Pearson education. Addison-Wesley, 2002.

[2] M. Born, E. Wolf, Principles of Optics, 7th Edition, Cambridge University Press, Cambridge, UK 2003.

[3] J. W. Goodman, Introduction to Fourier Optics, 3rd Edition, Roberts and Company Publishers, Greenwood, CO (2005).

[4] E. Abbe, "Beiträge zur theorie des mikroskops und der mikroskopischen wahrnehmung," Archiv für Mikroskopische Anatomie, 9(1), 413-418 (1873).

[5] Lord Rayleigh, "Investigations in optics, with special reference to the spectroscope," Philosophical Magazine, 8(49), 261-274 (1879).

[6] C. M. Sparrow, "On spectroscopic resolving power," Astrophysical Journal, 44(2), 76-86 (1916).

[7] W. V. Houston, "A compound interferometer for fine structure work," Physical Review, 29(3), 478-484 (1927).

[8] B. Richards and E. Wolf, "Electromagnetic diffraction in optical systems II, structure of the image field in an aplanatic system," Proceedings of the Royal Society of London A, 253(1274), 358-379 (1959).

[9] D. N. Grimes and B. J. Thompson, "Two-point resolution with partially coherent light," Journal of the Optical Society of America, 57(11), 1330-1334 (1967).

[10] A. J. den Dekker and A. van den Bos, "Resolution: a survey," Journal of the Optical Society of America A, 14(3), 547-557 (1997).

[11] A. Lipson, S. G. Lipson, and H. Lipson, Optical Physics, 4th Edition, Cambridge University Press, Cambridge, UK (2010).

[12] D. Courjon, Near-field microscopy and near-field optics, Imperial College Press, London, UK (2007).

[13] B. P. Ramsay, E. L. Cleveland, and O. T. Koppius, "Criteria and the intensity-epoch slope," Journal of the Optical Society of America, 31(1), 26-33 (1941).

[14] M. E. Testorf and M. A. Fiddy, "Super-resolution imaging-revisited," Advances in Imaging and Electron Physics, 163, 165-218 (2010).

[15] S. W. Hell, J. Wichmann, Breaking the diffraction resolution limit by stimulated emission: stimulated-emission-depletion fluorescence microscopy, Optics Letters 19 (11) 780-782 (1994).

[16] S. W. Hell, M. Kroug, Ground-state-depletion fluorescence microscopy: A concept for breaking the diffraction resolution limit, Applied Physics B 60 (5) 495-497 (1995).

[17] K. I. Willig, S. O. Rizzoli, V. Westphal, R. Jahn, and S. W. Hell, STED microscopy reveals that synaptotagmin remains clustered after synaptic vesicle exocytosis. Nature 440: 935-939 (2006).

[18] V. Westphal, S. O. Rizzoli, M. A. Lauterbach, D. Kamin, R. Jahn, and S.W. Hell, Video-rate far-field optical nanoscopy dissects synaptic vesicle movement. Science 320: 246-249 (2008).

[19] D. Wildanger, R. Medda, L. Kastrup, and S. W. Hell, A compact STED microscope providing 3D nanoscale resolution. Journal of Microscopy 236: 35-43 (2009).

[20] S. Bretschneider, C. Eggeling, S.W. Hell, Breaking the diffraction barrier in fluorescence microscopy by optical shelving, Physical Review Letters 98 (21) (2007).

[21] The Nobel Prize in Chemistry 2014 - Prize Announcement, https://www.nobelprize.org/nobel_prizes/chemistry/laureates/2014/announcement.html.

[22] E. Betzig, G. H. Patterson, R. Sougrat, O. W. Lindwasser, S. Olenych, J. S. Bonifacino, M. W. Davidson, J. Lippincott-Schwartz, and H. F. Hess, Imaging intracellular fluorescent proteins at nanometer resolution. Science 313: 1642-1645 (2006).

[23] M.J. Rust, M. Bates, X. Zhuang, Sub-diffraction-limit imaging by stochastic optical reconstruction microscopy (STORM), Nature Methods 3 (10) 793-796 (2006).

[24] T. J. Gould, M. S. Gunewardene, M. V. Gudheti, V. V. Verkhusha, S. Yin, J. A. Gosse, and S. T. Hess, Nanoscale imaging of molecular position and anisotropies. Nature Methods 5:1027-1030 (2008).

[25] S. T. Hess, T. P. K. Giriajan and M. D. Mason, Ultra-high resolution imaging by fluorescence photoactivation localization microscopy. Biophysical Journal 91: 4258-4272 (2006).

[26] H. Shroff, C. G. Galbraith, J. A. Galbraith and E. Betzig, Live-cell photoactivated localization microscopy of nanoscale adhesion dynamics. Nature Methods 5: 417-423 (2008).

[27] H. Shroff, H. White and E. Betzig, Photoactivation localization microscopy (PALM) of adhesion complexes. Current Protocols in Cell Biology 41: 4.21.27 (2008).

[28] M. Bates, B. Huang, G. T. Dempsey and X. Zhuang, Multicolor super-resolution imaging with photo-switchable fluorescent probes. Science 317: 1749-1753 (2007).

[29] X. Zhuang, Nano-imaging with STORM. Nature Photonics 3: 365-367 (2009).

[30] B. Huang, S. A. Jones, B. Brandenburg and X. Zhuang, Whole-cell 3D STORM reveals interactions between cellular structures with nanometer-scale resolution. Nature Methods 5: 1047-1052 (2008).

[31] M. G. Gustafsson, Method and Apparatus for Three-Dimensional Microscopy With Enhanced Depth Resolution, https://patents.google.com/patent/US5671085A/en Feb. (1995).

[32] M. G. Gustafsson, Surpassing the lateral resolution limit by a factor of two using structured illumination microscopy, Journal of Microscopy 198 (2) 82-87 (2000).

[33] D. Karadaglic and T. Wilson, Image formation in structured illumination wide-field fluorescence microscopy. Micron 39: 808-818 (2008).

[34] M. A. A. Neil, R. Juskaitis and T. Wilson, Method of obtaining optical sectioning by using structured light in a conventional microscope. Optics Letters 22: 1905-1907 (1997).

[35] M. F. Langhorst, J. Schaffer and B. Goetze, Structure brings clarity: Structured illumination microscopy in cell biology. Biotechnology Journal 4: 858-865 (2009).

[36] F. Chasles, B. Dubertret and A. C. Boccara, Optimization and characterization of a structured illumination microscope. Optics Express 15: 16130-16140 (2007).

[37] M. G. L. Gustafsson, Surpassing the lateral resolution limit by a factor of two using structured illumination microscopy. Journal of Microscopy. 198(2): p. 82-87 (2000).

[38] L. Schermelleh, P.M. Carlton, S. Haase, L. Shao, L. Winoto, et al., Sub-diffraction multicolor imaging of the nuclear periphery with 3D structured illumination microscopy. Science. 320 (5881): p. 1332-1336 (2008).

[39] G. Tortarolo, M. Castello, A. Diaspro, S. Koho and G. Vicidomini, Evaluating image resolution in STED microscopy. Optica 5, 32-35 (2018).

[40] M. G. L. Gustafsson, Nonlinear structured-illumination microscopy: wide-field fluorescence imaging with theoretically unlimited resolution, Proceedings of the National Academy of Sciences of the United States of America 102 (37) 13081-13086 (2005).

[41] G. Huszka and M. A. M. Gijs, Super-resolution optical imaging: A comparison, Micro and Nano Engineering, Volume 2, Pages 7-28 (2019)

[42] E. H. Synge, A suggested method for extending microscopic resolution into the ultra-microscopic region, The London, Edinburgh, and Dublin Philosophical Magazine and Journal of Science 6 (35) 356-362 (1928).

[43] D. W. Pohl, W. Denk, M. Lanz, Optical stethoscopy: image recording with resolution $\lambda/20$, Applied Physics Letters 44 (7) 651-653 (1984).

[44] A. Lewis, M. Isaacson, A. Harootunian, A. Muray, Development of a 500 Å spatial resolution light microscope: I. light is efficiently transmitted through $\lambda/16$ diameter apertures, Ultramicroscopy 13 (3) 227-231 (1984).

[45] A. Harootunian, E. Betzig, M. Isaacson, A. Lewis, Super-resolution fluorescence near-field scanning optical microscopy, Applied Physics Letters 49 (11) 674-676 (1986).

[46] U. Dürig, D.W. Pohl, F. Rohner, Near-field optical-scanning microscopy, Journal of Applied Physics 59 (10) 3318-3327 (1986).

[47] E. Betzig, M. Isaacson, A. Lewis, Collection mode near-field scanning optical microscopy, Applied Physics Letters 51 (25) 2088-2090 (1987).

[48] H. Heinzelmann, B. Hecht, L. Novotny, D.W. Pohl, Forbidden light scanning near field optical microscopy, Journal of Microscopy 177 (2) 115-118 (1995).

[49] B. Hecht, H. Heinzelmann, D.W. Pohl, Combined aperture SNOM/PSTM: best of both worlds? Ultramicroscopy 57 (2) 228-234 (1995).

[50] U.C. Fischer, D.W. Pohl, Observation of single-particle plasmons by near-field optical microscopy, Physical Review Letters 62 (4) 458-461 (1989).

[51] F. Zenhausern, Y. Martin, H.K. Wickramasinghe, Scanning interferometric apertureless microscopy: optical imaging at 10 angstrom resolution, Science 269 (5227) 1083-1085 (1995).

[52] Y. Inouye, S. Kawata, A scanning near-field optical microscope having scanning electron tunnelling microscope capability using a single metallic probe tip, Journal of Microscopy 178 (1) 14-19 (1995).

[53] P. Gleyzes, A.C. Boccara, R. Bachelot, Near-field optical microscopy using a metallic vibrating tip, Ultramicroscopy 57 (2) 318-322 (1995).

[54] C. Girard, O.J.F. Martin, A. Dereux, Molecular lifetime changes induced by nanometer scale optical fields, Physical Review Letters 75 (17) 3098-3101 (1995).

[55] J. Koglin, U. Fischer, H. Fuchs, Scanning near-field optical microscopy with a tetrahedral tip at a resolution of 6 nm, Journal of Biomedical Optics 1 (1) 75-79 (1996).

[56] Sugiura, Kawata, Okada, Fluorescence imaging with a laser trapping scanning nearfield optical microscope, Journal of Microscopy 194 (2-3) 291-294 (1999).

[57] B. Knoll, F. Keilmann, Near-field probing of vibrational absorption for chemical microscopy, Nature 399 (6732) 134-137 (1999).

[58] D. Courjon, Scanning Tunneling Optical Microscopy, Scanning Tunneling Microscopy and Related Methods, NATO ASI Series, Springer, Dordrecht, pp. 497-505 (1990).

[59] R. C. Reddick, R. J. Warmack, T. L. Ferrell, New form of scanning optical microscopy, Physical Review B 39 (1) 767-770 (1989).

[60] H. A. Bethe, Theory of diffraction by small holes, Physical Review 66 (7-8) 163-182 (1944).

[61] C. J. Bouwkamp, On Bethe's theory of diffraction by small holes, Philips Res. Rep. 5 321-332 (1950).

[62] J. Greffet, R. Carminati, Image formation in near-field optics, Progress in Surface Science 56 (3) 133-237 (1997).

[63] O. J. F. Martin, N. B. Piller, Electromagnetic scattering in polarizable backgrounds, Physical Review E 58 (3) 3909-3915 (1998).

[64] C. Girard, A. Dereux, Near-field optics theories, Reports on Progress in Physics 59 (5) 657 (1996).

[65] S. Jutamulia, M. Ohtsu, T. Asakura, Near-Field Optics: Physics, Devices, and Information Processing, Proceedings of SPIE Vol. 3791 (1999).

[66] Martin, 3d simulations of the experimental signal measured in near-field optical microscopy, Journal of Microscopy 194 (2–3) 235-239 (1999).

[67] J. B. Pendry, Negative refraction makes a perfect lens. Physical Review Letters. 85(18): p. 3966-3969 (2000).

[68] M. Cai and V. Shalaev, Optical Metamaterials. Springer Science+Business Media, 2010.

[69] Z. Chen, A. Taflove, V. Backman, Photonic nanojet enhancement of backscattering of light by nanoparticles: a potential novel visible-light ultramicroscopy technique, Optics Express 12 (7) 1214-1220 (2004).

[70] P. Ferrand, J. Wenger, A. Devilez, M. Pianta, B. Stout, N. Bonod, E. Popov, H. Rigneault, others, Direct imaging of photonic nanojets, Optics Express 16 (10) 6930-6940 (2008).

[71] Z. Chen, A. Taflove, V. Backman, Photonic nanojet enhancement of backscattering of light by nanoparticles: a potential novel visible-light ultra microscopy technique, Optics Express 12 1214-1220 (2004).

[72] X. Li, Z. Chen, A. Taflove, V. Backman, Optical analysis of nanoparticles via enhanced backscattering facilitated by 3-D photonic nanojets, Optics Express 13 526-533 (2005).

[73] A. V. Itagi, W. A. Challener, Optics of photonic nanojets, Journal of the Optical Society of America A 22 (12) 2847-2858 (2005).

[74] A. Devilez, B. Stout, N. Bonod, E. Popov, Spectral analysis of three-dimensional photonic jets, Optics Express 16 (18) 14200-14212 (2008).

[75] A. Heifetz, S. C. Kong, A.V. Sahakian, A. Taflove, V. Backman, Photonic nanojets, Journal of Computational and Theoretical Nanoscience 6 (9) 1979-1992 (2009).

[76] C. Y. Liu, Photonic jets produced by dielectric micro cuboids, Applied Optics 54 8694-8699 (2015).

[77] I. V. Minin, O. V. Minin, V. Pacheco-Peña, M. Beruete, Localized photonic jets from flat, three dimensional dielectric cuboids in the reflection mode, Optics Letters 40 (10) 2329-2332 (2015).

[78] C. Y. Liu, C. J. Chen, Characterization of photonic nanojets in dielectric microdisks, Physica E 73 226-234 (2015).

[79] D. McCloskey, J. J. Wang, J. F. Donegan, Low divergence photonic nanojets from Si3N4 micro-disks, Optics Express 20 128-140 (2012).

[80] Y. Shen, L.V. Wang, J.T. Shen, Ultralong photonic nanojet formed by a two layer dielectric microsphere, Optics Letters 39 4120-4123 (2014).

[81] P. K. Kushwaha, H.S. Patel, M.K. Swami, P.K. Gupta, Controlled shaping of photonic nanojets using core shell microspheres, Proc. SPIE 9654, International Conference on Optics and Photonics 2015, 96541H.

[82] Y. E. Geints, A. A. Zemlyanov, E.K. Panina, Microaxicon-generated photonic nanojets, Journal of the Optical Society of America B 32 (8) 1570-1574 (2015).

[83] V. V. Kotlyar, S. S. Stafeev, Modeling the sharp focus of a radially polarized laser mode using a conical and a binary microaxicon, Journal of the Optical Society of America B 27 (10) 1991-1997 (2010).

[84] S. A. Degtyarev, A. P. Porfirev, S. N. Khonina, Photonic nanohelix generated by a binary spiral axicon, Applied Optics 55 (12) B44-B48 (2016).

[85] M. J. Mendes, I. Tobías, A. Martí, A. Luque, Near-field scattering by dielectric spheroidal particles with sizes on the order of the illuminating wavelength, Journal of the Optical Society of America B 27 (6) 1221-1231 (2010).

[86] L. Han, Y. Han, G. Gouesbet, J. Wang, G. Gréhan, Photonic jet generated by spheroidal particle with Gaussian-beam illumination, Journal of the Optical Society of America B 31 (7) 1476-1483 (2014).

[87] L. Han, Y. Han, J. Wang, Z. Cui, Internal and near-surface electromagnetic fields for a dielectric spheroid illuminated by a zero-order Bessel beam, Journal of the Optical Society of America A 31 (9) 1946-1955 (2014).

[88] C.Y. Liu, F.C. Lin, Geometric effect on photonic nanojet generated by dielectric micro-cylinders with non-cylindrical cross-sections, Optics Communications 380 287-296 (2016).

[89] N. Eti, I. H. Giden, Z. Hayran, B. Rezaei, H. Kurt, Manipulation of photonic nanojet using liquid crystals for elliptical and circular core–shell variations, Journal of Modern Optics 64 1566-1577 (2017).

[90] M. S. Kim, T. Scharf, S. Mühlig, C. Rockstuhl, H.P. Herzig, Engineering photonic nanojets, Optics Express 19 (11) 10206-10220 (2011).

[91] Z. Wang, W. Guo, L. Li, B. Luk'yanchuk, A. Khan, Z. Liu, Z. Chen, M. Hong, Optical virtual imaging at 50 nm lateral resolution with a white-light nanoscope, Nature Communications 2 218 (2011).

[92] J. J. Schwartz, S. Stavrakis, S. R. Quake, Colloidal lenses allow high-temperature single-molecule imaging and improve fluorophore photostability, Nature Nanotechnology 5 (2) 127-132 (2010).

[93] A. Darafsheh, G.F. Walsh, L. Dal Negro, V.N. Astratov, Optical super-resolution by high-index liquid-immersed microspheres, Applied Physics Letters 101 (14) 141128 (2012).

[94] H. Yang, N. Moullan, J. Auwerx, M.A.M. Gijs, Fluorescence imaging: superresolution biological microscopy using virtual imaging by a microsphere nanoscope, Small 10 (9) (2014).

[95] A. Darafsheh, C. Guardiola, J. Finlay, A. Cárabe, D. Nihalani, Simple super-resolutionbiological imaging. SPIE Newsroom (2018).

[96] A. Darafsheh, C. Guardiola, D. Nihalani, D. Lee, J.C. Finlay, A. Cárabe, Biological Super-Resolution Imaging by Using Novel Microsphere-Embedded Coverslips. SPIE Proceeding 933705, (2015).

[97] A. Darafsheh, C. Guardiola, A. Palovcak, J.C. Finlay, A. Cárabe, Optical super-resolution imaging by high-index microspheres embedded in elastomers, Optics Letters 40 (1) 5 (2015).

[98] H. Yang, M.A. Gijs, Optical microscopy using a glass microsphere for metrology of sub-wavelength nanostructures, Microelectronic Engineering 143 86-90 (2015).

[99] L.A. Krivitsky, J.J. Wang, Z. Wang, B. Luk'yanchuk, Locomotion of microspheres for super-resolution imaging, Scientific Reports 3 (1) (2018).

[100] Y. Li, Z. Shi, S. Shuai, L. Wang, Widefield scanning imaging with optical super-resolution, Journal of Modern Optics 62 (14) 1193-1197 (2015).

[101] G. Huszka, M.A.M. Gijs, Turning a normal microscope into a super-resolution instrument using a scanning microlens array, Scientific Reports 8 (1) (2018).

[102] J. Li, W. Liu, T. Li, I. Rozen, J. Zhao, B. Bahari, B. Kante, J. Wang, Swimming microrobot optical nanoscopy, Nano Letters 16 (10) 6604-6609 (2016).

[103] F. Wang, L. Liu, H. Yu, Y. Wen, P. Yu, Z. Liu, Y. Wang, W. J. Li, Scanning superlens microscopy for non-invasive large field-of-view visible light nanoscale imaging, Nature Communications 7 13748 (2016).

[104] M. Duocastella, F. Tantussi, A. Haddadpour, R.P. Zaccaria, A. Jacassi, G. Veronis, A. Diaspro, F.D. Angelis, Combination of scanning probe technology with photonic nanojets, Scientific Reports 7 (1) (2018).

[105] B. Du, Y.-H. Ye, J. Hou, M. Guo, T. Wang, Sub-wavelength image stitching with removable microsphere-embedded thin film, Applied Physics A 122 (1) (2018).

[106] B. Yan, Z. Wang, A.L. Parker, Y.-k. Lai, P. John Thomas, L. Yue, J.N. Monks, Superlensing microscope objective lens, Applied Optics 56 (11) 3142 (2017).

[107] D.N. Sitter, J.S. Goddard, R.K. Ferrell, Method for the measurement of the modulation transfer function of sampled imaging systems from bar-target patterns, Applied Optics 34 (4) 746-751 (1995).

[108] R. Horstmeyer, R. Heintzmann, G. Popescu, L. Waller, C. Yang, Standardizing the resolution claims for coherent microscopy, Nature Photonics 10 (2) 68-71 (2016).

[109] W. A. Shurcliff, Polarized Light, Harvard University Press, Cambridge, Massachusetts, 1962.

[110] A. Gerrard and J. M. Burch, Introduction to Matrix Methods in Optics, Wiley, London, 1975.

[111] P. S. Theocaris and E. E. Gdoutos, Matrix Theory of Photoelasticity, Springer Verlag, Berlin, 1979.

[112] M. Bass, C. DeCusatis, J. M. Enoch, V. Lakshminarayanan, G. Li, C. MacDonald, V. N. Mahajan, E. V. Stryland, Handbook of Optics, Third Edition Volume I: Geometrical and Physical Optics, Polarized Light, Components and Instruments, McGraw-Hill Inc., New York, 2010.

[113] Q. Zhan, Cylindrical vector beams: from mathematical concepts to applications, Advances in Optics and Photonics 1 (1) 1-57 (2009).

[114] E. Wolf, "Electromagnetic diffraction in optical systems I. An integral representation of the image field," Proceedings of the Royal Society of London. Series A 253, 349-357 (1959).

[115] K. Yee, Numerical solution of initial boundary value problems involving maxwell's equations in isotropic media, IEEE Transactions on Antennas and Propagation. 14 3, 302-307 (1966).

[116] K. S. Youngworth and T. G. Brown, Focusing of high numerical aperture cylindrical vector beams, Optics Express 7, 77-87 (2000).

[117] S. K. Selvaraja, P. Jaenen, W. Bogaerts, D. V. Thourhout, P. Dumon, R. Baets. Fabrication of photonic wire and crystal circuits in silicon-on-insulator using 193-nm optical lithography. Journal of Lightwave Technology 27:4076-83 (2009).

[118] V. V. Kotlyar, S. S. Stafeev, L. O'Faolain, V. A. Soifer. Tight focusing with a binary microaxicon. Optics Letters 36:3100-2 (2011).

[119] L. Granero, V. Micó, Z. Zalevsky, J. García. Super-resolution imaging method using phase-shifting digital lensless Fourier holography. Optics Express 17:15008-22 (2009).

[120] X. P. Li, Y. Y. Cao, M. Gu. Superresolution-focal-volume induced 3.0 Tbytes/disk capacity by focusing a radially polarized beam. Optics Letters 36:2510-2 (2011).

[121] H. Wang, C. J. R. Sheppard, K. Ravi, S. T. Ho, G. Vienne. Fighting against diffraction: apodization and near field diffraction structures. Laser & Photonics Reviews 6:354-92 (2012).

[122] H. Wang, L. Shi, B. Lukyanchuk, C. J. R. Sheppard, C. T. Chong. Creation of a needle of longitudinally polarized light in vacuum using binary optics. Nature Photonics 2:501-5 (2008).

[123] M. Sohail, A. A. Mudassar. Geometric super-resolution by using an optical mask. Applied Optics 49:3000-5 (2010).

[124] J. M. Wang, W. B. Chen, Q. W. Zhan. Engineering of high purity ultra-long optical needle field through reversing the electric dipole array radiation. Optics Express, 18:21965-72 (2010).

[125] V. V. Kotlyar, S. S. Stafeev, Y. K. Liu, O'Faolain Liam, K. Alexey. Analysis of the shape of a subwavelength focal spot for the linearly polarized light. Applied Optics 52:330-9 (2013).

[126] L. L. Yin, V. K. Vlasko-Vlasov, J. Pearson, J. M. Hiller et al. Subwavelength focusing and guiding of surface plasmons. Nano Letters, 5:1399-402 (2005).

[127] S. Quabis, R. Dorn, M. Eberler, O. Glockl, G. Leuchs. Focusing light to a tighter spot. Optics Communications 179:1–7 (2000).

[128] G. M. Lerman, U. Levy. Effect of radial polarization and apodization on spot size under tight focusing conditions. Optics Express, 16:4567-81 (2008).

[129] Q. Tan, K. Cheng, Z. Zhou, G. Jin, Diffractive super-resolution elements for radially polarized light. Journal of the Optical Society of America A 27:1355-60 (2010).

[130] K. Huang, P. Shi, X. L. Kang, X. Zhang, Y. P. Li. Design of DOE for generating a needle of a strong longitudinally polarized field. Optics Letters 35:965-7 (2010).

[131] J. Lin, K. Yin, Y. D. Li, J. B. Tan. Achievement of longitudinally polarized focusing with long focal depth by amplitude modulation. Optics Letters 36:1185-7 (2011).

[132] C. Emmanuel, F. Michael, G. Thomas, P. Nicolas, A.-A. Kamel. Transverse superresolution technique involving rectified Laguerre-Gaussian LG0p beams. Journal of the Optical Society of America A 28:1709-15 (2011).

[133] Q. G. Sun, K. Y. Zhou, G. Y. Fang, G. Q. Zhang, Z. J. Liu, S. T. Liu. Hollow sinh-Gaussian beams and their paraxial properties. Optics Express, 20:9682-91 (2012).

[134] K. Kitamura, K. Sakai, S. Noda. Sub-wavelength focal spot with long depth of focus generated by radially polarized, narrow-width annular beam. Optics Express, 184518-25 (2010).

[135] Z. J. Liu, H. F. Zhao, J. L. Liu, J. Lin, A. Ahmad Muhammad, S. T. Liu. Generation of hollow Gaussian beams by spatial filtering. Optics Letters 32:2076-8 (2007).

[136] S. N. Khonina, S. G. Volotovsky, Controlling the contribution of the electric field components to the focus of a high-aperture lens using binary phase structures. Journal of the Optical Society of America A 27:2188-97 (2010).

[137] J. Durnin, J. J. Miceli Jr., J. H. Eberly. Diffraction-free beams. Physical Review Letters 58:1499-501 (1987).

[138] Y. Kozawa, T. Hibi, A. Sato, H. Horanai, M. Kurihara, N. Hashimoto, H. Yokoyama, T. Nemoto, S. Sato, Lateral resolution enhancement of laser scanning microscopy by a higher-order radially polarized mode beam, Optics Express 19 15947-15954 (2011).

[139] X. Li, T. H. Lan, C. H. Tien, M. Gu, Three-dimensional orientation-unlimited polarization encryption by a single optically configured vectorial beam, Nature Communications 3 998 1-5 (2012).

[140] R. Dorn, S. Quabis, G. Leuchs, Sharper focus for a radially polarized light beam, Physical Review Letters 91 233901 1-4 (2003).

[141] H. Ye, C. Wan, K. Huang, T. Han, J. Teng, Y. S. Ping, C. W. Qiu, Creation of vectorial bottle-hollow beam using radially or azimuthally polarized light, Optics Letters 39 630-633(2014).

[142] H. Dehez, A. April, M. Piché, Needles of longitudinally polarized light: guidelines for minimum spot size and tunable axial extent, Optics Express 20 14891-14905 (2012).

[143] Y. Zhao, Q. Zhan, Y. Zhang, Y. P. Li, Creation of a three-dimensional optical chain for controllable particle delivery, Optics Letters 30 848-850 (2005).

[144] J. Wang, W. Chen, Q. Zhan, Creation of uniform three-dimensional optical chain through tight focusing of space-variant polarized beams, Journal of Optics 14 055004 1-6 (2012).

[145] J. Zhao, B. Li, H. Zhao, Y. Hu, W. Wang, Y. Wang, Tight focusing properties of the azimuthal discrete phase modulated radially polarized LG11 beam, Optics Communications 296 95-100 (2013).

[146] W. Chen, Q. Zhan, Creating a spherical focal spot with spatially modulated radial polarization in 4Pi microscopy, Optics Letters 34 2444-2446 (2009).

[147] S. Yan, B. Yao, W. Zhao, M. Lei, Generation of multiple spherical spots with a radially polarized beam in a 4π focusing system, Journal of the Optical Society of America A 272033–2037 (2010).

[148] H. Lin, B. Jia, M. Gu, Generation of an axially super-resolved quasi-spherical focal spot using an amplitude-modulated radially polarized beam, Optics Letters 36 2471-2473 (2011).

[149] S. N. Khonina, I. Golub, Engineering the smallest 3D symmetrical bright and dark focal spots, Journal of the Optical Society of America A 30 2029-2033 (2013).

[150] T. Liu, J. Tan, J. Liu, J. Lin, Creation of subwavelength light needle, equidistant multi-focus, and uniform light tunnel, Journal of Modern Optics 60 378-381 (2013).

[151] Y. Kozawa, S. Sato, Dark-spot formation by vector beams, Optics Letters 33 2326-2328 (2008).

[152] Z. Chen, D. Zhao, 4Pi focusing of spatially modulated radially polarized vortex beams, Optics Letters 37 1286-1288 (2012).

[153] Y. Zhang, Y. Dai, Multifocal optical trapping using counter-propagating radially polarized beams, Optics Communications 285 725-730 (2012).

[154] X. L. Wang, J. Ding, J. Q. Qin, J. Chen, Y. X. Fan, H. T. Wang, Configurable three-dimensional optical cage generated from cylindrical vector beams, Optics Communications 282 3421-3425 (2009).

[155] M. Schrader, M. Kozubek, S. W. Hell, T. Wilson, Optical transfer functions of 4Pi confocal microscopes: theory and experiment, Optics Letters 22 436-438 (1997).

[156] G.Y. Chen, F. Song, H. T. Wang, Sharper focal spot generated by 4π tight focusing of higher-order Laguerre-Gaussian radially polarized beam, Optics Letters 38 3937-3940 (2013).

[157] D. Day, M. Gu, Effects of refractive-index mismatch on three-dimensional optical data-storage density in a two-photon bleaching polymer, Applied Optics 37 6299-6304 (1998).

[158] H. Guo, X. Weng, M. Jiang, Y. Zhao, G. Sui, Q. Hu, Y. Wang, and S. Zhuang, Tight focusing of a higher-order radially polarized beam transmitting through multi-zone binary phase pupil filters, Optics Express 21, 5363–5372 (2013).

[159] G. H. Yuan, S. B. Wei, and X.-C. Yuan, Nondiffracting transversally polarized beam, Optics Letters 36, 3479-3481 (2011).

[160] S. N. Khonina, Simple phase optical elements for narrowing of a focal spot in high-numerical-aperture conditions, Optical Engineering 52, 091711 (2013).

[161] S. G. Reddy, A. Kumar, S. Prabhakar, and R. P. Singh, Experimental generation of ring-shaped beams with random sources, Optics Letters 38, 4441-4444 (2013).

[162] S. N. Khonina, S. V. Alferov, and S. V. Karpeev, Strengthening the longitudinal component of the sharply focused electric field by means of higher-order laser beams, Optics Letters 38, 3223-3226 (2013).

[163] J. Wang, Q. Liu, Y. Liu, W. Chen, and Q. Zhan, Discrete complex amplitude filter for ultra long optical tube, Proceedings of SPIE 8097, 809722 (2011).

[164] J. Lin, P. Genevet, M. A. Kats, N. Antoniou, and F. Capasso, Nanostructured holograms for broadband manipulation of vector beams, Nano Letters 13, 4269-4274 (2013).

[165] Y. Song, D. Milam, and W. T. Hill III, Long, narrow all-light atom guide, Optics Letters 24, 1805-1807 (1999).

[166] D. Ganic, X. Gan, and M. Gu, Focusing of doughnut laser beams by a high numerical-aperture objective in free space, Optics Express 11, 2747-2752 (2003).

[167] Z. Wang, Y. Dong, and Q. Lin, Atomic trapping and guiding by quasi-dark hollow beams, Journal of Optics A 7, 147-153 (2005).

[168] A. Calatayud, V. Ferrando, L. Remón, W. D. Furlan, and J. A. Monsoriu, Twin axial vortices generated by Fibonacci lenses, Optics Express 21, 10234-10239 (2013).

[169] A. Ortiz-Ambriz, S. Lopez-Aguayo, Y. V. Kartashov, V. A. Vysloukh, D. Petrov, H. Garcia-Gracia, J. C. Gutiérrez-Vega, and L. Torner, Generation of arbitrary complex quasi-non-diffracting optical patterns, Optics Express 21, 22221-22231 (2013).

[170] Q. Zhan, Properties of circularly polarized vortex beams, Optics Letters 31, 867-869 (2006).

[171] S. N. Khonina, N. L. Kazanskiy, and S. G. Volotovsky, Vortex phase transmission function as a factor to reduce the focal spot of high-aperture focusing system, Journal of Modern Optics 58, 748-760 (2011).

[172] L. Rao, J. Pu, Z. Chen, and P. Yei, Focus shaping of cylindrically polarized vortex beams by a high numerical-aperture lens, Optics & Laser Technology 41, 241-246 (2009).

[173] S. F. Pereira and A. S. van de Nes, Superresolution by means of polarisation, phase and amplitude pupil masks, Optics Communications 234, 119-124 (2004).

[174] L. Chen, Y. Zhou, Y. Li, M. Hong, Microsphere enhanced optical imaging and patterning: From physics to applications, Applied Physics Reviews 6 (2019) 021304.

[175] L. W. Chen, Y. Zhou, M. X. Wu, M. H. Hong, Remote-mode microsphere nano-imaging: new boundaries for optical microscopes, Opto-Electronic Advances 01 01 170001 (2018).

[176] L. Yue, B. Yan, Z. Wang, Photonic nanojet of cylindrical metalens assembled by hexagonally arranged nanofibers for breaking the diffraction limit, Optics Letters 41 (7) 1336-1339 (2016).

[177] H. Yang, R. Trouillon, G. Huszka, M. A. M. Gijs, Super-Resolution Imaging of a Dielectric Microsphere Is Governed by the Waist of Its Photonic Nanojet, Nano Letters 16 8 4862-4870 (2016).

[178] H. Yang, M. Cornaglia, M. A. M. Gijs, Photonic Nanojet Array for Fast Detection of Single Nanoparticles in a Flow, Nano Letters 15 3 1730-1735 (2015).

[179] H. Wang, X. Wu, D. Shen, Trapping and manipulating nanoparticles in photonic nanojets, Optics Letters 41 7 1652-1655 (2016).

[180] B. Born, J. D. A. Krupa, S. Geoffroy-Gagnon, and J. F. Holzman, Integration of photonic nanojets and semiconductor nanoparticles for enhanced all-optical switching, Nature Communications 6, 8097 (1-9) (2015).

[181] B. Born, S. Geoffroy-Gagnon, J. D. A. Krupa, I. R. Hristovski, C. M. Collier, and J. F. Holzman, Ultrafast all-optical switching via subdiffractional photonic nanojets and select semiconductor nanoparticles, ACS Photonics, 3 1095-1101 (2016).

[182] E. McLeod, C.B. Arnold, Sub-wavelength direct-write nanopatterning using optically trapped microspheres, Nature Nanotechnology, 3 413-417 (2008).

[183] W. Wu, A. Katsnelson, O.G. Memis, H. Mohseni, A deep sub-wavelength process for the formation of highly uniform arrays of nanoholes and nanopillars, Nanotechnology 18 485302 (2007).

[184] J. Kim, K. Cho, I. Kim, W.M. Kim, T.S. Lee, K. Lee, Fabrication of plasmonic nanodiscs by photonic nanojet lithography, Applied Physics Express 5 025201 (2012).

[185] A. Bonakdar, M. Rezaei, R.L. Brown, V. Fathipour, E. Dexheimer, S.J. Jang, H. Mohseni, Deep-UV microsphere projection lithography, Optics Letters 40 11 2537-2540 (2015).

[186] A. Bonakdar, M. Rezaei, E. Dexheimer, H. Mohseni, High-throughput realization of an infrared selective absorber/emitter by DUV microsphere projection lithography, Nanotechnology 27 3 035301 (2016).

[187] K. J. Yi, H. Wang, Y. Lu, Z. Yang, Enhanced Raman scattering by self-assembled silica spherical micro particles, Journal of Applied Physics 101 063528 (2007).

[188] R. Dantham, P.B. Bisht, C.K.R. Namboodiri, Enhancement of Raman scattering by two orders of magnitude using photonic nanojet of a microsphere, Journal of Applied Physics109 103103 (2011).

[189] P. K. Upputuri, Z. Wu, L. Gong, C. K. Ong, H. Wang, Super-resolution coherent anti- Stokes Raman scattering microscopy with photonic nanojets, Optics Express 22 11 12890-12899 (2014).

[190] A. Darafsheh, D. Bollinger, Systematic study of the characteristics of the photonic nanojets formed by dielectric microcylinders, Optics Communications 402 270-275 (2017).

[191] M. X. Wu, B. J. Huang, R. Chen, Y. Yang, J. F. Wu, R. Ji, X. D. Chen, M. H. Hong, Modulation of photonic nanojets generated by microspheres decorated with concentric rings, Optics Express 23 15 20096-20103 (2015).

[192] M. X. Wu, R. Chen, J. H. Soh, Y. Shen, L. S. Jiao, J. F. Wu, X. D. Chen, R. Ji, M. H. Hong, Super-focusing of center-covered engineered microsphere, Scientific Reports 6 31637 (2016).

[193] M. X. Wu, R. Chen, J. Z. Ling, Z. C. Chen, X. D. Chen, R. Ji, M. H. Hong, Creation of a longitudinally polarized photonic nanojet via an engineered microsphere, Optics Letters 42 7, 1444-1447 (2017).

[194] Y. Zhou, H. Gao, J. H. Teng, X. G. Luo, M. H. Hong, Orbital angular momentum generation via a spiral phase microsphere, Optics Letters 43 1 34-37 (2018).

[195] H.S. Patel, P.K. Kushwaha, M.K. Swami, Generation of highly confined photonic nanojet using crescent-shape refractive index profile in microsphere, Optics Communications 415 140-145 (2018).

[196] C. Alpmann, S. Schlickriede, E. Otte, and C. Denz, Dynamic modulation of poincaré beams. Scientific Reports 7, 8076 (2017).

[197] C. Rosales-Guzman, N. Bhebhe, and A. Forbes. Simultaneous generation of multiple vector beams on a single SLM. Optics Express, 25:25697–25706, (2017).

[198] J. Chen, C. H. Wan and Q. W. Zhan, Vectorial optical fields: recent advances and future prospects, Science Bulletin 63, 54 (2018)

APPENDIX A   CODE FOR FAR-FIELD ANALYTICAL CALCULATION

Matlab code example for the calculation of the focusing performance of a hollow Gaussian beam in a high NA focusing system.

```matlab
%Focusing performance of a hollow Gaussian beam in a high NA focusing system
%------------------------------------------------------------------------
clc
close all
clear
format long
naper=0.95;              % NA of the objective lens
nshu=4097;
refm=1.0;                % Refractive index of air
theta=asin(naper/refm);
wave=1.0;                % wavelength
kv=2*pi/wave;            % wave vector
ra=4*wave;
za=8*wave;
nr=513;
nz=513;
dr=-ra:ra/(nr-1):ra;
dz=-za:za/(nz-1):za;
save dr
save dz
nrx=length(dr);
nzx=length(dz);
thetax=0:theta/(nshu-1):theta;
dtheta=theta/(nshu-1);

%----------------hollow Gaussian Beam-------------------------------------
omega=theta;
alphaf=0.1;
cp=0.1;
omega_0=alphaf*omega;
sintheta=sin(thetax);
beam=exp(-(sintheta-cp).^2/omega_0^2);
figure;plot(thetax,beam);

%----------------Analytical Results---------------------------------------
E_field_r=zeros(nrx,nzx);
E_field_z=zeros(nrx,nzx);
for m=1:nrx;
    rr=dr(m);
    bessa=besselj(0,kv*abs(rr)*sin(thetax));
    bessb=besselj(1,kv*abs(rr)*sin(thetax));
    for n=1:nzx;
        zz=dz(n);
        E_f_r=sqrt(cos(thetax)).*sin(2*thetax).*beam.*bessb.*exp(sqrt(-1)*kv*zz*cos(thetax));
        Efr=0.5*dtheta*sum(E_f_r(1,1:nshu-1)+E_f_r(1,2:nshu));
        E_field_r(m,n)=Efr;
        clear E_f_r Efr
        E_f_z=2*sqrt(-1)*sqrt(cos(thetax)).*((sin(thetax)).^2).*beam.*bessa.*exp(sqrt(-1)*kv*zz*cos(thetax));
        Efz=0.5*dtheta*sum(E_f_z(1,1:nshu-1)+E_f_z(1,2:nshu));
        E_field_z(m,n)=Efz;
        clear E_f_z Efz
    end
end
per=(abs(E_field_r)).^2;
pez=(abs(E_field_z)).^2;
petotal=per+pez;
petm=max(max(petotal));
per=per/petm;
pez=pez/petm;
petotal=petotal/petm;

save petotal
p4r=petotal(:,nz);
p4z=petotal(nr,:);
figure
subplot(1,3,1);imshow(per,[]);colorbar
subplot(1,3,2);imshow(pez,[]);colorbar
subplot(1,3,3);imshow(petotal,[]);colorbar
figure
plot(dr,per(:,nz),'red','LineWidth',1);
hold on
plot(dr,pez(:,nz),'blue','LineWidth',1);
plot(dr,petotal(:,nz),'black','LineWidth',1);
hold on
```

APPENDIX B   SCRIPT FOR NEAR-FIELD NUMERICAL CALCULATION

Example code for generating a radially or azimuthally polarized beam.

```
1  ##########################################################################
2  # Description:
3  # This is an example of how to create a radially or azumithally polarized source.
4  # In this example, we create a radially or azumithally polarized source using a
5  # paraxial beam profile definition.
6  ##########################################################################
7
8  # clear all current variables
9  clear;
10 switchtolayout;
11
12 # set desired beam polarization (radial=1, azimuthal=2)
13 pol = 1;
14
15 # define position vectors
16 x = linspace(-10e-6,10e-6,501);
17 y = linspace(-10e-6,10e-6,501);
18 z = 0;
19 X = meshgridx(x,y);
20 Y = meshgridy(x,y);
21
22 lambda0 = 0.532e-6;
23 f = c/lambda0;
24 w = 2*pi*f;
25 k = 2*pi/lambda0;
26
27 ##################################################
28 # define beam using a simple near field definition
29 ##################################################
30    # Specify beam envelope
31
32    ## using FWHM
33    # FWHM = 5e-6;
34    # sigma = FWHM / ( 2*sqrt(2*log(2)) );
35    # envelope = exp( - (X^2)/(2*sigma^2) - (Y^2)/(2*sigma^2) );
36
37    # using field intensity at 1/e^2
38    w0 = 5e-6;
39    XY2 = sqrt(X^2 + Y^2);
40    hs = 0;
```

```
40    hs = 0;
41    #hs = 0.8e-5;
42    envelope = exp( - (XY2 - hs)^2/(w0^2) );
43    # envelope = exp( - (X^2)/(w0^2) - (Y^2)/(w0^2) );
44
45
46    # specify near fields
47    phi=atan2(Y,X);
48
49    if(pol==1){     # if radial polarization
50        Ex = cos(phi);
51        Ey = sin(phi);
52        Ez = 0;
53    }else{  # if azimuthal polarization
54        Ex = -sin(phi);
55        Ey = cos(phi);
56        Ez = 0;
57    }
58    Ex = Ex*XY2*envelope;
59    Ey = Ey*XY2*envelope;
60    Ez = Ez*envelope;
61
62    #Field Normalization
63    nx = max(Ex);
64    ny = max(Ey);
65    Ex = Ex/nx;
66    Ey = Ey/ny;
67
68    # Package field data into the EM fields dataset that can be
69    # loaded into the Import source
70    EM = rectilineardataset("EM fields",x,y,z);
71    EM.addparameter("lambda",c/f,"f",f);
72    EM.addattribute("E",Ex,Ey,Ez);
73
74  # directly load dataset into source
75  select("import_beam");
76  importdataset(EM);
77  set("center wavelength",lambda0);
78  set("wavelength span",0);
79
80  # save dataset to .mat file which can be imported at a later time
```

```
80   # save dataset to .mat file which can be imported at a later time
81   matlabsave("Source_EM.mat",EM);
82
83   # run simulation;
84   run;
85
86
87   # plot field data
88   E_forward = getresult("T","E"); # forward E field, E results from T monitor
89   E_backward = getresult("R","E"); # backward E field, E results from R monitor
90   E_propagate = getresult("XZ","E"); # propagation E field along Z axis, E results from XZ monitor
91   T = getresult("T","T"); # transmission of T monitor
92   R = getresult("R","T"); # transmission of R monitor, it's actually reflection in this case
93   visualize(EM);
94   visualize(E_forward);
95   visualize(E_backward);
96   visualize(E_propagate);
97   #visualize(T);
98   #visualize(R);
99
100  # Save a selected set of variables to a mat file
101  x=getdata("T","x");
102  y=getdata("T","y");
103  Ex=getdata("T","Ex");
104  Ey=getdata("T","Ey");
105  Ez=getdata("T","Ez");
106  E_total=getelectric("T");
107  matlabsave("XY_EM", x,y,Ex,Ey,Ez,E_total);
108  ?"Created: XY_EM.mat";
109
110  xx=getdata("XZ","x");
111  zz=getdata("XZ","z");
112  Exx=getdata("XZ","Ex");
113  Eyy=getdata("XZ","Ey");
114  Ezz=getdata("XZ","Ez");
115  EE_total=getelectric("XZ");
116  matlabsave("XZ_EM", xx,zz,Exx,Eyy,Ezz,EE_total);
117  ?"Created: XZ_EM.mat";
118
119  yy=getdata("YZ","x");
120  zzz=getdata("YZ","z");
121  Exxx=getdata("YZ","Ex");
122  Eyyy=getdata("YZ","Ey");
123  Ezzz=getdata("YZ","Ez");
124  EEE_total=getelectric("YZ");
125  matlabsave("YZ_EM", yy,zzz,Exxx,Eyyy,Ezzz,EEE_total);
126  ?"Created: YZ_EM.mat";
127
128  xxx=getdata("XZ_contour","x");
129  zzzz=getdata("XZ_contour","z");
130  s_outline=getdata("XZ_contour","index_x");
131  matlabsave("StructureOutline", xxx,zzzz,s_outline);
132  ?"Created: StructureOutline.mat";
133
134  #E=getresult("XZ","E");     # E fields at monitor
135  #filename="ElectricField";
136  #matlabsave(filename, E);
137
138
139  # plot E field data in vector plot
140  E_dataset = rectilineardataset("EM fields",x,y,z);
141  E_dataset.addparameter("lambda",c/f,"f",f);
142  E_dataset.addattribute("E",Ex,Ey,Ez);
143
144  #vectorplot(E_dataset);
145  #vectorplot(E_forward);
146  #vectorplot(E_backward);
```

APPENDIX C   LIST OF PUBLICATIONS

The following is a list of publications during my Ph. D. study.

1. R. Chen, J. Lin, P. Jin, M. Cada and Y. Ma, Photonic nanojet beam shaping by illumination polarization engineering, Optics Communications, 456, 124593, 2020

2. R. Chen, M. Cada, Y. Ma, Numerical and Experimental Study of Photonic Nanojets Generated by Microspheres, 2017 IEEE International Conference on Computational Electromagnetics, Japan, 2017

3. R. Chen, J. Lin, P. Jin, Y. Ma and M. Cada, Photonic nanojet effect of surface nanostructured dielectric micro-cylinders, Photonics North 2015, Canada, 2015

4. R. Chen, J. Lin, P. Jin, Y. Ma and M. Cada, Photonic nanojets generated by microcylinders with rough surface, The 28th annual IEEE Canadian Conference on Electrical and Computer Engineering, Canada, 2015

5. J. Lin, R. Chen, P. Jin, M. Cada, Y. Ma, Super-resolution Focusing with Polarized Optical Beam, The 28th annual IEEE Canadian Conference on Electrical and Computer Engineering, Canada, 2015

6. J. Lin, R. Chen, P. Jin, M. Cada and Y. Ma, Generation of longitudinally polarized optical chain by 4π focusing system, Optics Communications, 340, 69–73(2015).

7. J.-M. Daignan, R. Chen, K. A. Mahmoud, Y. Ma, I. G. Hill and L. Kreplak, Patterning of nanocrystalline cellulose gel phase by electrodissolution of a metallic electrode, PLOS One. 9(6):e99202 (2014)

8. J. Lin, R. Chen, H. C. Yu, P. Jin, Y. Ma and M. Cada, Generation of hollow beam with radially polarized vortex beam and amplitude filter, Journal of the Optical Society of America A, Vol. 31, Issue 7, pp. 1395-1400 (2014)

9. J. Lin, R. Chen, H. C. Yu, P. Jin, M. Cada and Y. Ma, Analysis of sub-wavelength focusing generated by radially polarized doughnut Gaussian beam, Optics & Laser Technology, 64, 242–246 (2014)

APPENDIX D   EXPERIMENTAL OBSERVATION OF PHOTONIC NANOJETS GENERATED BY MICROSPHERES

I.   Numerical results

First, Finite-difference time-domain (FDTD) computational technique is used to solve Maxwell's equations for this photonic nanojet generating model. We consider microspheres with a diameter of d = 15 μm and a refractive index of n_p = 1.59 (polystyrene) embedded in a medium of refractive index n_m = 1.0 (air) or 1.33 (water). In the calculation process, linearly polarized plane waves propagate through the microsphere.

Since the diameter of the microspheres studied here is 15 μm and the illumination light is in the visible region. The size parameter implies that ray optics can still be a good approximation. Using the geometrical optics theory, we can estimate that the effective focal length is around 9.33 µm in air and 19.80 μm in water. The effective focal length is defined as the distance from the center of a microsphere to the maximum intensity of the photonic nanojet.

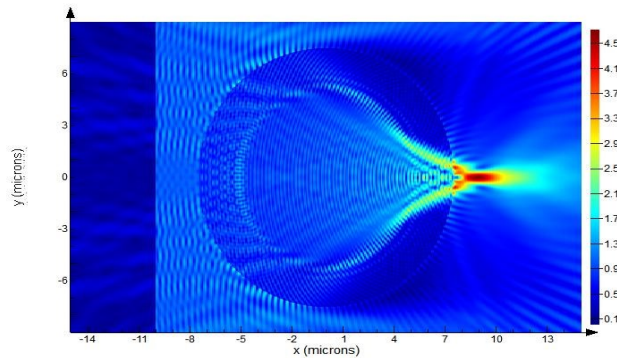Figure 1 The contour map of the electric field distribution

The FDTD analysis results are shown in Figure 1. We see that the electric field is scattered by the dielectric microsphere. The ripples inside and outside the microsphere are the results of the interference between the incident and the reflected waves. Apparently, a high intensity tight focusing spot can be observed at the exit interface of the microsphere. The

location, size and intensity of this focusing spot are controlled by the size of the spheres and the refractive index of both the microsphere and the surrounding medium. These are key parameters to study and careful considerations should be taken when selecting microspheres for specific applications.

II.   Experimental results

The experiment was carried out using a Zeiss Axio Imager Z2 microscope. PS Microspheres were dispersed in liquid and transferred to a coverslip using a pipette. Then the sample was moved to the microscope stage. A 40× water immersion objective was used to investigate the photonic nanojet. Therefore, the surrounding medium is going to be water in this case. The microscope system has a high precision three dimensional motorized stage. So that it can be used to adjust the focal plane in the z direction and perform a z scan. In principle, the microscope can take a series of images at different z level. In this experiment, 77 images were taken at different z level and the resolution of the z direction movement is 500 nm. Therefore, the focal plane traveled a total of 38 μm in the z direction.

High intensity photonic nanojet can be clearly observed from the images shown in Figure 2. The effective focal length of the generated photonic nanojet can be extracted after analyzing the obtained images.

Table 1 Comparison of effective focal length

Physical Model	Effective Focal Length		
	Geometrical optics estimation	FDTD analysis	Experimental results
PS in air	9.33 μm	8.83 μm	-
PS in water	19.80 μm	18.33 μm	~ 10 μm

Table 1 summarizes the geometrical optics analysis, FDTD analysis and experimental results. As we can see that the two numerical calculation results are very close. However, there is a significant difference between the numerical results and the experimental results. Although there are many causes of this difference, we have identified two most important

components here: (1) the illumination is monochromatic light in the FDTD analysis whereas it is full spectrum white light in the experiment. (2) the coverslip in the experiment will change the illumination condition which in turn will cause errors in the experiment results.

Figure 2 Experimental observation of photonic nanojet